VANADIUM OXIDE MICROBOLOMETERS WITH PATTERNED GOLD BLACK OR PLASMONIC RESONANT ABSORBERS

by

EVAN M. SMITH
B.A. Physics, Drew University, 2007
M.S. Physics, University of Central Florida, 2012

A dissertation submitted in partial fulfillment of the requirements
for the degree of Doctor of Philosophy
in the Department of Physics
in the College of Sciences
at the University of Central Florida
Orlando, Florida

Fall Term
2015

Major Professor: Robert E. Peale

© 2015 Evan Smith

ABSTRACT

High sensitivity uncooled microbolometers are necessary to meet the needs of the next generation of infrared detectors, which seek low power consumption and production cost without sacrificing performance. Presented here is the design, fabrication, and characterization of a microbolometer with responsivity enhanced by novel highly absorptive coatings. The device utilizes a gold-doped vanadium oxide film in a standard air bridge design. Performance estimations are calculated from current theory, and efforts to maximize signal to noise ratio are shown and evaluated. Most notably, presented are the experimental results and analysis from the integration of two different absorptive coatings: a patterned gold black film and a plasmonic resonant structure.

Infrared-absorbing gold black was selectively patterned onto the active surfaces of the detector. Patterning by metal lift-off relies on protection of the fragile gold black with an evaporated oxide, which preserves gold black's near unity absorptance. This patterned gold black also survives the dry-etch removal of the sacrificial polyimide used to fabricate the air-bridge bolometers. Infrared responsivity is improved 70% for mid-wave IR and 22% for long-wave IR. The increase in the thermal time constant caused by the additional mass of gold black is a modest 15%. However, this film is sensitive to thermal processing; experimental results indicate a decrease in absorptance upon device heating.

Sub-wavelength resonant structures designed for long-wave infrared (LWIR) absorption have also been investigated. Dispersion of the dielectric refractive index provides for multiple overlapping resonances that span the 8-12 μm LWIR wavelength band, a broader range than can be achieved using the usual resonance quarter-wave cavity engineered into

the air-bridge structures. Experimental measurements show an increase in responsivity of 96% for mid-wave IR and 48% for long-wave IR, while thermal response time only increases by 16% due to the increased heat capacity. The resonant structures are not as susceptible to thermal processing as are the gold black films. This work suggests that plasmonic resonant structures can be an ideal method to improve detector performance for microbolometers.

To my wife and two beautiful children

ACKNOWLEDGMENTS

First and foremost I wish to thank Dr. Peale for his constant guidance and support in my research. He has showed me what it means to be a professional experimental physicist, and guided me to all of the opportunities I have taken advantage of in my professional career. He has also showed me how to write a professional quality paper. Most importantly, he has demonstrated that learning is a lifelong process, and that the purpose of graduate school is not so much to learn facts, but gain the skills to teach yourself in the future. I am very grateful for the experience of working with such a great advisor.

I would also like to thank my committee members: Dr. Saiful Khondaker, Dr. Adrienne Dove, and Dr. Glenn Boreman, for their advice and wisdom. In particular, I appreciate the support and interest Dr. Boreman has showed me and my research, as he made it a point to meet with me when he has visited Central Florida.

I also want to thank Dr. David Shelton and Dr. James Ginn for their guidance and support of my work, both in my efforts towards graduation and in my work through Plasmonics, Inc. I appreciate the opportunity to work for such a great company during my tenure at UCF. I also want to acknowledge my coworkers at Plasmonics, Dr. Andrew Warren, Dr. Christopher Long, Joshua Perlstein, Pedro Figueiredo, Nathan Post, KatyAnn Cassidy, Natalie Concors, Alex Dillard, and Robert John. Without your assistance this work would have not been completed.

I want to thank my lab mates in Dr. Peale's group: Dr. Deep Panjwani, Dr. Janardan Nath, Dr. Farnood Khalilzadeh-Rezaie, Dr. Imen Rezadad, Javaneh Boroumand, and Mehmet

Yesiltas. Particularly, thanks to Deep and Janardan for the assistance in developing the gold black and metamaterials absorbers that are the crux of this dissertation.

I would like to thank everyone involved in the UCF physics cleanroom, particularly Seth Calhoun and Guy Zummo. Everything that I know about servicing and maintaining high-tech equipment I learned from Guy Zummo. He has been very integral in my education while at UCF.

The work in this dissertation has been funded by Plasmonics, Inc., though a grant from Army Research Labs SBIR program, W911QX-13-C-0013.

Many thanks to my parents for supporting me and my family through this time, and for always believing in me. Thanks especially to my father for discussing my research and taking the time to look through this dissertation. I am grateful to my many friends have supported me in this effort, including my family at First Alliance Church (Chad, Lonnie and Charlie in particular) as well as emotional support from Pastor Craig Hofer through our weekly meetings.

I would like to express my deepest gratitude and thanks to my wife, Abby, for going through this process with me and putting up with me. This dissertation is as much yours as it is mine. You have stood beside me in all of this, and given me the confidence and motivation to complete this work. Thanks as well to my two children, Kinnebrew and Elliott, who were always there to remind me of the more important things in life. No matter how difficult the day may have been, it was always made better by coming home and hearing a joyful cry of "Daddy!"

Above all else, all glory and praise goes to God through Jesus Christ, without Whom there would be no infrared physics to study. In this long and at times trying process, He has been my strength when I was weak, my endurance when I was tired, my wisdom when I lacked it, my confidence when I failed, and my joy when I could see none.

TABLE OF CONTENTS

LIST OF FIGURES xi

LIST OF TABLES xv

ACRONYMS AND ABBREIVIATIONS xvi

CHAPTER ONE: INTRODUCTION 1

CHAPTER TWO: THEORETICAL CONSIDERATIONS 8

2.1 Blackbody Radiation Theory 8

2.2 Responsivity 10

2.2.1 Temperature Coefficient of Resistivity 10

2.2.2 Thermal Considerations 11

2.2.3 Responsivity of a Microbolometer 16

2.3 Noise Considerations 17

2.3.1 Johnson Noise 18

2.3.2 Thermal Fluctuation Noise and Background Fluctuation Noise 20

2.3.3 1/f Noise 22

2.3.4 Total System Noise 24

2.4 Optimization Techniques 27

2.4.1 TCR and Resistivity 28

2.4.2 Thermal Conductance 29

2.4.3 Absorptance 32

2.5 Measurement Techniques 39

2.5.1 Testing Schematic 39

2.5.2 Derivation of Incident Power 42

2.5.3 NEP and D* 44

2.5.4 NETD 45

CHAPTER THREE: MICROBOLOMETER DEVELOPMENT 49

3.1 Microbolometer Design and Performance Estimations 49

3.2 VO_x-Au Development and Optimization 53

3.2.1 Background 53

3.2.2 Experimental Methods 57

3.2.3 Results ... 62
3.3 Optimization of Microbolometer Design ... 68
3.3.1 NiCr Arms ... 68
3.3.2 Polyimide Sidewalls ... 71
3.3.3 Release Methods and Design Failures ... 73
3.3.4 Detector Redesign ... 77
CHAPTER FOUR: SENSITIVITY ENHANCEMENTS USING PATTERNED GOLD BLACK ABSORBER ... 82
4.1 Experimental Methods ... 82
4.2 Absorption Measurements ... 86
4.3 Responsivity and Noise Measurements ... 91
4.4 Absorption Effects from Thermal Processing ... 99
4.5 D* and NETD ... 105
4.6 Summary ... 107
CHAPTER FIVE: SENSITIVITY ENHANCEMENTS USING SUB-WAVELENGTH RESONANT ABSORBERS ... 108
5.1 Theoretical Considerations ... 108
5.2 Experimental Methods ... 111
5.3 Responsivity and Noise Measurements ... 117
5.4 D* and NETD ... 125
5.5 Summary ... 126
CHAPTER SIX: CONCLUSIONS ... 127
6.1 Evaluation of Methods ... 127
6.2 Future Experiments ... 130
APPENDIX A: DERIVATION OF BLACKBODY RADIANCE ... 132
APPENDIX B: PUBLICATIONS ... 141
APPENDIX C: COPYRIGHT PERMISSION LETTERS ... 144
REFERENCES ... 147

LIST OF FIGURES

Figure 1. Atmospheric Transmission for NIR-LWIR. Ref. [2] 2

Figure 2. Thermal schematic for a bolometer. Energy comes in to the detector by radiation from the source, energy leaves by conduction through the two arms and by radiation. 13

Figure 3. Schematic for a voltage divider circuit used to measure ΔV across the detector, and by extension, measure ΔR. 14

Figure 4. Noise voltage per unit root bandwidth for each of the four main types of detector noise as a function of modulation frequency at 1V applied bias. 25

Figure 5. Noise voltage per unit root bandwidth for each of the four main types of detector noise as a function of applied bias voltage. 27

Figure 6. TCR as a function of resistivity for VO_x films [25]. Reprinted from Uncooled Infrared Imaging Arrays and Systems, Semiconductors and Semimetals Vol. 47, Wood, R.A., Monolithic Silicon Microbolometer Arrays, page 55, Copyright 1997, with permission from Elsevier and Academic Press.. 29

Figure 7. Thermal Conductance through microbolometer support arms as a function of arm length, compared with the limits of radiation and conduction of air at atmospheric pressure. 32

Figure 8. Simulated reflectance spectrum of quarter wave cavity. 34

Figure 9. Schematic of device test configuration.. 41

Figure 10. Schematic showing the solid angle Ω based upon a detector with area A_d a distance r away from a blackbody. 43

Figure 11. Ray diagram schematic in which a lens is used with a detector to image a source. 46

Figure 12. Drawing of the detector design before (A) and after (B) removal of the sacrificial polyimide. 51

Figure 13. Deposition rate, TCR and resistivity of VOx films as a function of oxygen/argon ratio. Films were deposited by reactive pulsed-dc magnetron sputtering by Jin et al. [35]. Reprinted with permission from Jin, Y.O., et al., Potential for reactive pulsed-dc magnetron sputtering of nanocomposite VOx microbolometer thin films. Journal of Vacuum Science & Technology A, 2014. **32**(6): p. 061501, Copyright 2014, American Vacuum Society. 56

Figure 14. RGA data measured during a deposition The peak at 32 AMU is characteristic for O_2, while the peaks at 36 and 40 AMU show Argon. 60

Figure 15. Plot of ln(R) vs. T a VO_x-Au film deposited with 3% O_2 and 12% Au. 62

Figure 16. Relationship between % O_2, % Au and room temperature resistivity............ 63

Figure 17. Relationship between % O_2, % Au and TCR. 64

Figure 18. TCR and resistivity plot for samples using only one vanadium target. Samples are identified here by the nominal oxygen content. 65

Figure 19. Film stress causing breaking and bending of deposited NiCr. The breaking point is generally at the polyimide sidewall. In this image, the polyimide was designed to be squares directly underneath the pixel. 70

Figure 20. Film stress as a function of chamber pressure during sputter coating of NiCr. 70

Figure 21. Polyimide sidewalls before and after an isotropic plasma etch. This process is designed to increase the slope of the sidewall. 73

Figure 22. Microscope images showing the progression of the O_2 plasma release etch on single pixel. The polyimide seen around and under the pixel can be seen to be retreating over time. 75

Figure 23. SEM image of a detector in which the NiCr arm has broken along the polyimide sidewall after release. 76

Figure 24. The edges of a sputtered VOx-Au film, showing the “bat-ear” effect that could cause electrical impedance issues. 77

Figure 25. Process schematic for the redesign of the pixel, using a trench etch as opposed to the polyimide sacrificial layer.. 78

Figure 26. SEM images showing the two designs of microbolometers fabricated in this study: the top utilizes the sacrificial polyimide, while the bottom utilizes the flat pixel and silicon trench etch. 81

Figure 27. Deposition chamber for thermal evaporation of gold black (bell jar is removed). [49] 83

Figure 28. An array of gold black-coated pixels fabricated for testing purposes. In this image the gold black has been slightly misaligned, but is still electrically isolated. 85

Figure 29. VOx air-bridge bolometers without (a) and with (b) the gold black coating. . 86

Figure 30. Specular and diffuse reflectance of SiO_2-protected gold black film on gold-coated silicon, at incidence angles of 7, 15, 30, 45, and 60°. 87

Figure 31 Spatial absorptance map for individual pixel. (a) and (b) show the absorptance across a single pixel without gold black coating for MWIR and LWIR, respectively. The corresponding absorptance for a pixel with the gold black coating is shown in images (c) and (d). 89

Figure 32. Absorptance spectra averaged over one pixel with and without gold black overcoat. The spike near 4.2 μm is an artifact due to atmospheric CO_2................. 91

Figure 33. Voltage responsivity and noise voltage over a range of detectors, displayed as a function of detector resistance. Measurements are made at 80 Hz chopping frequency with 1 V applied bias and no optical filter.. 93

Figure 34. Measured noise voltage as a function of frequency for five devices with gold black compared with five uncoated device. A fit of the data generated by integrating Eq. 39 is presented, using a measurement bandwidth of 17 Hz. 95

Figure 35. Voltage responsivity as a function of chopping frequency. The solid lines are fits to Eq. 29.. 97

Figure 36. Voltage responsivity as function of IR bandwidth, which is given by horizontal limits of each bar. The solid curve is the incident power spectrum based on the blackbody radiance at 300˚. The upper percentage labels give the responsivity increase due to the gold black coating, while the lower values in parentheses give the absorptance increase for the same range. Note that the range for LWIR responsivity is 7.6-14.6 μm, while the LWIR absorption range is only from 7.6-11 μm. Measurements taken at 37 Hz with 3V applied bias.. 99

Figure 37. Reflectance spectra of gold black after annealing at the indicated temperatures for 10 minutes. 101

Figure 38. Comparison of protected gold black films under similar thermal processes. The red curve shows the reflectance of a sample that has an additional 350 nm SiO_2 deposited in a 300˚C PECVD process. 102

Figure 39. Top-down view of gold black films coated in SiO_2. The first sample (a) has had no heat treatment, while (b) and (c) have been heated on a hot plate at 100˚C and 300˚C, respectively. 350 nm PECVD oxide has been deposited on (d), during which thermal treatment was very similar to (c). 103

Figure 40. SEM cross section images of investigated samples: (a) unheated, (b) 100˚C, (c) 300˚C and (d) PECVD additional overcoat. 105

Figure 41. Schematic of the structured metamaterial absorber..................................... 109

Figure 42. Comparison of detectors without patterned metamaterial (top) and with the metamaterial detector patterned (bottom). 113

Figure 43. SEM images of (top) absorber structures on VO_x air-bridge bolometer and (bottom) absorber structures on Si substrate. 114

Figure 44. Reflectance spectra of absorber structure measured by FTIR. Reflectance minima (absorption peaks) are labeled. 115

Figure 45. Noise voltages from devices with and without absorbers as a function of frequency, here plotted on a log-log scale. The Johnson noise floor is shown in blue, and the data are fitted based on Eq. 66 for 1/f noise. 119

Figure 46. The voltage responsivity of devices with and without absorbers as a function of chopping frequency. This data is taken with a bias voltage of 2V. The solid lines are fits to Eq. 29. 121

Figure 47. Responsivity and noise voltage as a function of bias voltage measured at 35 Hz. 123

Figure 48. Voltage responsivity as a function of measurement bandwidth, plotted in comparison to the spectral incident power used in measurement for a 300°C blackbody. Data were taken using 2V applied bias at 35 Hz modulation. 124

Figure 49. Comparison of absorbed power between different absorbers, plotted against the maximum absorbed power for a 300°C blackbody. 129

Figure 50. Schematic for a VO_x-Au microbolometer with integrated resonant absorber structure. 131

LIST OF TABLES

Table 1. Physical and thermal properties of materials used in device fabrication........... 52

Table 2. Resistivity and TCR values of VO_x-Au films produced with modified co-sputtering method. Samples 1 and 2 were purposely thicker films. 66

Table 3. Effect of substrate bias on TCR and resistivity for a number of different deposition parameters. 68

Table 4. Comparison of D* and NETD for devices with and without gold black under various testing conditions 106

Table 5. Data averaged over 10 detectors with and without the absorbing structure. 118

Table 6. Comparison of D* and NETD for devices with and without the absorbers under various testing configurations. 125

ACRONYMS AND ABBREIVIATIONS

Au	Gold
CF_4	Carbon Tetrafluoride
D*	Normalized Detectivity
FTIR	Fourier Transform Infrared Spectroscopy
FPA	Focal Plane Array
HDR	Hemispherical Diffuse Reflectometer
KOH	Potassium Hydroxide
KRS-5	Thallium Bromo-Iodide
LWIR	Long-Wave Infrared, 8-12 µm
MEMS	Micro-Electromechanical Sensor
MWIR	Mid-Wave Infrared, 3-5 µm
NETD	Noise Equivalent Temperature Difference
NEP	Noise Equivalent Power
NiCr	Nichrome (Nickel/Chrome 80/20)
NMP	n-methyl-2-pyrrolidone

O_2	Oxygen
PECVD	Plasma Enhanced Chemical Vapor Deposition
RIE	Reactive Ion Etcher
RGA	Residual Gas Analyzer
ROIC	Read-Out Integrated Circuit
SEM	Scanning Electron Microscope
SF_6	Sulfur Hexafluoride
SNR	Signal-to-Noise Ratio
SWIR	Short-Wave Infrared, 0.75-2.5µm
TCR	Temperature Coefficient of Resistivity
TMAH	Tetramethyl Ammonium Hydroxide
VO_x-Au	Gold Doped Amorphous Vanadium Oxide

CHAPTER ONE: INTRODUCTION

Infrared radiation is the general term for electromagnetic waves whose wavelengths extend beyond the visible spectrum, between 0.75 μm to 1000μm. This type of radiation was discovered in 1800 by William Herschel when he measured an increase in radiant power (by measuring temperature) through the visible spectrum and extending beyond into the "invisible thermometrical spectrum" [1]. Research into this field over the following century led to the work of Rayleigh, Wien and Planck, among others, in developing the theory of blackbody radiation, which describes the phenomenon of *self-radiation*. All charged particles, including atoms, will oscillate and emit electromagnetic radiation at a specific frequency or wavelength. The amount of radiant energy an object emits, and the frequencies at which it emits that energy, depends on its temperature and emissivity.

A blackbody is defined as an object that both absorbs all incident electromagnetic energy, and, by the law of conservation of energy, must perfectly emit this energy as radiation if in thermodynamic equilibrium. While such an object is only theoretically perfect, many objects will exhibit a *nearly* blackbody behavior. The sun is near perfect blackbody, whose peak emission, based upon its temperature, is 0.5 μm (right in the middle of our visible spectrum) but also acts as a broadband source of infrared radiation, which we experience as heat. Earth's atmosphere restricts the transmission of this radiation within certain wavelength bandwidths. A plot of atmospheric transmission with wavelength can be seen in Figure 1 [2], which in particular points out absorption bands of the most common atmospheric molecules. Based upon Earth's transmission windows, infrared radiation is

typically divided into three bandwidths: short-wave IR (SWIR, 0.75-2.5 µm), mid-wave IR (MWIR, 3-5 µm) and long-wave IR (LWIR, 8-14 µm).

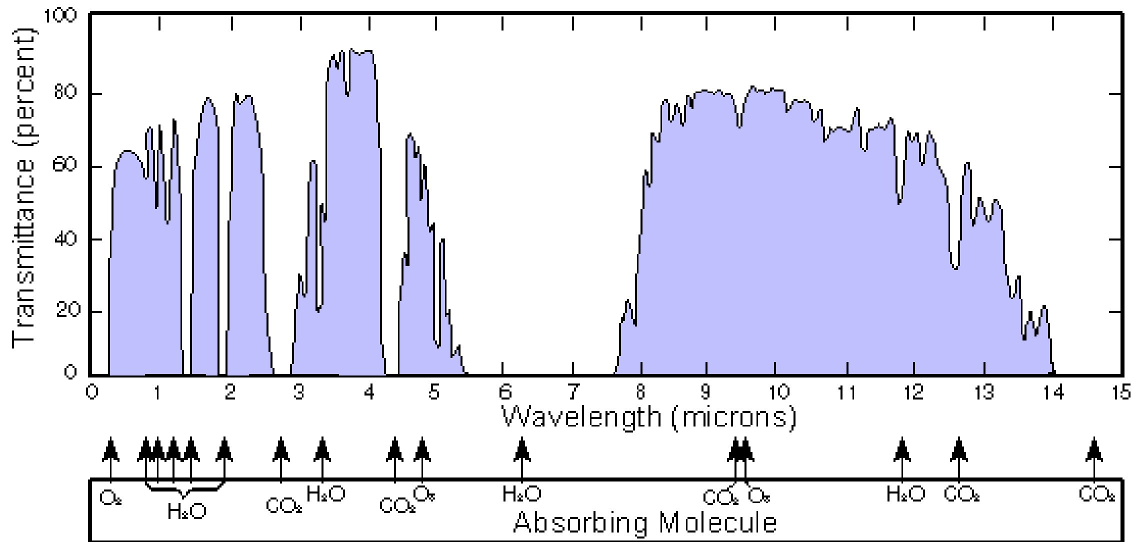

Figure 1. Atmospheric Transmission for NIR-LWIR. Ref. [2]

An infrared detector is a device designed to transduce infrared radiation into measurable electrical signals. A two-dimensional detector array, or Focal Plane Array (FPA), allows infrared imaging, which is useful for "night vision" based on the infrared radiation that objects *emit*, rather than by the sunlight that they *reflect*. Such imagers are also ideal in environments such as fog, smoke or dense dust, where Rayleigh scattering obscures the transmittance of the shorter optical wavelengths but has little to no effect on infrared radiation, especially for the LWIR. These imagers have a wide range of applications, including defense, surveillance, security, and emergency response.

Infrared detectors are classified as either photon detectors or thermal detectors. Photon

detectors function by the excitation of bound electrons by incident photons. In a photoconductor, for instance, this interaction causes an increase in conductivity, which can be measured by monitoring the voltage fluctuations across the detector biased with a constant current. Thermal detectors, on the other hand, convert radiant energy to heat. One such device is a microbolometer, in which heat will change the resistance of an active film, which can be measured in the same manner as a photoconductor.

A thermal detector is distinguished from a photon detector in that it must be thermally isolated to achieve high sensitivity. This is generally achieved through an air bridge structure, in which the detector is suspended above a substrate by support arms. These devices are slower than photon detectors because they rely on a thermal time constant determined by the heat flux through the support arms. They are also generally less sensitive than photon detectors. However, a thermal detector has the potential to absorb energy on a broader bandwidth than photon detectors and can be less expensive to fabricate. To obtain high sensitivity, many photon detectors require cryogenic cooling, which can be expensive and use a lot of power; thermal detectors can operate uncooled (at ambient temperature). Thermal detectors are therefore an attractive option over photon detectors in terms of cost and power consumption.

A microbolometer is a Micro-Electromechanical Sensor (MEMS) device fabricated by silicon micromachining. The device consists of a thin dielectric membrane supporting an active film suspended above a substrate and connected to that substrate by two or more support arms that allow and control thermal and electrical conduction. This film will

change its resistance upon heating and can be either a metal or a semiconductor. Pure metal films typically increase their resistance as they heat up; insulators and semiconductors will decrease their resistance with heating.[3] The amount by which films change their resistance with heat is defined as the material Temperature Coefficient of Resistivity (TCR). TCR is positive for metals and negative for semiconductors. High TCR is desirable for increased sensitivity. Films are also characterized by their room temperature resistivity, ρ_{RT}, which is desired to be low for noise considerations. Many different films have been used and studied in microbolometers [4], such as platinum [5], titanium [6], amorphous silicon [7] and amorphous vanadium oxide (VO_x) [8].

Vanadium oxide is perhaps one of the most widely used films in modern microbolometers [4, 9-11]. VO_x has a fairly low resistivity yet a high TCR, making it a desirable material for microbolometers. Single crystal films of unique stoichiometry can exhibit high TCR, but will generally have a metal-to-insulator transition around a specific temperature at which the resistivity will change by orders of magnitude [12]. For VO_2 this occurs around 68˚C. Additionally, this transition exhibits a hysteresis effect, in which the temperature to transition in one direction will not be the same to transition back. In contrast, the amorphous vanadium oxide film has a much more stable TCR with no hysteresis, which makes it a better candidate for thermal imaging applications than a single crystal film.

An infrared imaging system consists of detectors in an FPA, imaging optics, electronic read out, and a hermetically sealed evacuated housing. An important figure of merit for any

infrared imaging system is the Noise Equivalent Temperature Difference (NETD), defined as

$$NETD = \frac{\Delta T}{SNR}, \quad (1)$$

where ΔT is the temperature difference and SNR is the signal to noise ratio. NETD is the minimum resolvable temperature contrast achievable for the imager. Any object to be imaged by a detector system will emit radiation with a power representative of its temperature. However, the background scene surrounding the object will also emit radiation, often with a similar intensity or spectral behavior. In a low contrast (high NETD) image, the object will be obscured by the background radiation. An improved detector with NETD < 50 mK will result in a more recognizable image [4]. Current state of the art imagers still have much lower contrast and resolution than are possible with a visible imager.

As use of infrared detectors has become more widespread, the demand for better-performing, lower-cost detectors has increased. Efforts to enhance the performance of a vanadium oxide microbolometer without sacrificing fabrication complexity, cost, or power consumption are required to meet this need. This can be achieved through increasing the TCR of the vanadium oxide or by increasing the device thermal isolation. The former has limitations of the material properties of vanadium oxide; the latter involves a trade-off with response time. Alternatively, detectors can be more thermally efficient by maximizing absorption.

Infrared detectors typically are optimized for LWIR or MWIR by Fabry-Perot [4, 13] and other resonant structures [14-16], whose peak absorbance and bandwidth depend on resonator Q and hence on fabrication tolerances. Broadband absorbing films, such as metal black films, have been investigated as well [17-19]. These films are quite desirable for their low heat capacity (due to porosity) and high absorption over a much broader spectral range than is possible by any other mechanism. In principle, such absorbing structures can be ideal tools for optimization as they can increase detector responsivity without increasing noise or thermal time constant.

It is the aim of this research to evaluate various methods of increasing detector performance for a VO_x microbolometer, developed and fabricated by Plasmonics, Inc.[20]. ***Chapter 2*** provides the theoretical background behind device operation, responsivity, noise, and characterization methods. ***Chapter 3*** describes device fabrication. Included is a discussion of methods to improve mechanical strength and stability of the air bridge structure, as well as efforts to decrease the resistivity of the VO_x film without affecting TCR. The next two chapters deal with optimizing absorption by two kinds of absorbing films: ***Chapter 4*** reports integration of a broadband gold black film, while ***Chapter 5*** reports the use of a *metamaterial* with multiple absorption peaks. Finally, ***Chapter 6*** provides a summary and comparative evaluation of methods described, as well as presents possible future experiments.

Gold black has very high absorption over a broad spectral range [21]. Blanket coatings are easily achieved using an ordinary thermal evaporator, suggesting the possibility of

multiband sensors fabricated using a single material with minimal fabrication tolerances. This very low-density material is extremely fragile, which makes it difficult to integrate onto a micro-bolometer array, since usual fabrication processes destroy the film. A novel approach for patterning of gold black by a standard lift-off technique using evaporated SiO_2 as a protection layer has been demonstrated [22]. Measurements of detector performance with and without a gold black coating for comparison are reported.

One trade-off of using metal black films is that they can be fragile, making them susceptible to standard fabrication processes. While this fragility has been shown to be a solvable problem, it is indicative of a more fundamental concern. Films are thermomechanically unstable due to their mixed grain size and porous structure, yet it is this very structure that gives gold black its high absorption. These films can collapse over time, which results in a decrease in absorptance. More immediately, the absorptance of gold black will decrease at high temperatures, such as those experienced in standard vacuum packaging processes. Therefore an alternate absorbing material based upon a metamaterial structure is proposed.

Metamaterials are much thinner than their resonant wavelengths and comprise resonant structures that are laterally sub-wavelength as well. For LWIR applications, required dimensions are still within capability of standard UV photolithography, and dispersion within dielectric elements create multiple resonances that span the LWIR with strong absorption [23]. Such an absorber has been successfully on an optimized VO_x microbolometer. Responsivity and noise measurements are compared between devices with and without the absorbers, and a significant improvement is demonstrated.

CHAPTER TWO: THEORETICAL CONSIDERATIONS

2.1 Blackbody Radiation Theory

Planck's Law describes the amount of energy emitted from a body in reference to the body's internal temperature over a specific wavelength bandwidth. This relationship can be determined by considering any object as a distribution of harmonic oscillators under Bose-Einstein statistics, which will emit photons with energy related to their frequency of oscillation. Planck's law defines the *spectral radiance*, L_λ, as [24]

$$L_\lambda = \frac{2hc^2}{\lambda^5\left[e^{\frac{hc}{\lambda kT}}-1\right]} \, , \qquad (2)$$

in which $h = 6.6 \times 10^{-34}\, J\, s$ is Planck's constant, $c = 3 \times 10^8\, m/s$ is the speed of light in vacuum, $k = 1.38 \times 10^{-23}\, J/K$ is the Boltzmann constant, T is the internal temperature of the body, and λ is the specific wavelength at which this energy is emitted. L_λ typically has units of Watts cm^{-2} sr^{-1} μm^{-1} . A full derivation of Eq. 2 is given in Appendix A.

Spectral radiance is the power per unit source area emitted into a unit solid angle per unit wavelength interval. The total radiance L in W cm^{-2} sr^{-1} within a finite bandwidth $\lambda_1 - \lambda_2$ at a given temperature is found by integrating Eq. 2 with the substitution $x = \frac{hc}{\lambda kT}$, giving

$$L = +\frac{2k^4T^4}{h^3c^2}\int_{x2}^{x1}\frac{x^3}{e^x-1}dx\ , \qquad (3)$$

which can be solved numerically. Integration over all wavelengths gives

$$L = \frac{\sigma}{\pi}T^4\ , \qquad (4)$$

which is the power per unit source area per unit solid angle, where σ is the Stefan-Boltzmann constant $\sigma = \frac{2\pi^5k^4}{15h^3c^2}$ (5.67 x 10^{-8} W m^{-2} K^{-4}). This assumes a Lambertian emitter where the radiance is proportional to cos (θ), where θ is the angle with respect to the surface normal. Integrating over a hemisphere gives

$$M = \sigma T^4, \qquad (5)$$

where *M* is the *radiant exitance*. Eq. 5 is the Stefan-Boltzmann Law. The exitance contrast is found by differentiating Eq. 5 with respect to temperature, which is useful for thermal mapping of an image. The exitance contrast is

$$\frac{\partial M}{\partial T} = 4\sigma T^3\frac{Watts}{cm^2\ K}\ . \qquad (6)$$

Multiplying Eq. 6 by the area of the body, A_d, and by the emissivity of the object ϵ ($\epsilon = 1$ for a blackbody) gives the total power leaving the object per degree, which is the defined as the thermal conductance by radiation,

$$G_{rad} \equiv 4\sigma\epsilon A_dT^3\frac{Watts}{K}\ . \qquad (7)$$

2.2 Responsivity

2.2.1 Temperature Coefficient of Resistivity

The resistance of a material is a function of temperature, given by [24]

$$R(T) = R_0(1 + \alpha \Delta T) , \tag{8}$$

where R_0 is the resistance at temperature T_0, $\Delta T = T - T_0$, and α is the TCR of the material, defined as

$$TCR \equiv \alpha = \frac{1}{R}\frac{dR}{dT} . \tag{9}$$

In a metal, an increase in temperature will cause a decrease in the mobility of free carriers, which will cause the resistance to rise. In a semiconductor, an increase in temperature will increase carrier mobility and density of mobile carriers. For a semiconductor, the resistance can be modeled based on the thermal excitation of carrier density across a bandgap [25]

$$R(T) = R_0 e^{\left(\frac{E_A}{kT}\right)} , \tag{10}$$

where E_A is the activation energy, equal to half of the bandgap energy E_g. By the definition of TCR in Eq. 9 the TCR of a semiconductor can be expressed as

$$\alpha = -\frac{E_A}{kT} . \tag{11}$$

The bandgap energy for VO_x is heavily dependent upon stoichiometry, but measurements on VO_2 films have shown $E_A \approx 0.7\ eV$ at room temperature [26]. By Eq. 11 the TCR for VO_2 turns out to be roughly -4.5 %/K. It is stressed that the bandgap energy and TCR of vanadium oxide films are heavily dependent upon stoichiometry and crystallography of the film, and that this calculation is a simplification of the TCR of VO_x films. In fact, TCR of VO_x films typically are in the range of -2% to -3% [4]. A detailed discussion of TCR in VO_x will be given in Chapter 3.

2.2.2 Thermal Considerations

The change in temperature as a function of incident power must be derived for analysis. The first law of thermodynamics is the law of the conservation of energy. The internal energy *E* of a body is a function of both the work *W* done on the system and the heat *Q* transferred to or from other bodies in contact with it. The change in energy per unit time of the body is written as [27]

$$\frac{dE}{dt} = \frac{dW}{dt} + \frac{dQ}{dt}\,. \tag{12}$$

The heat is positive if it flows into the body; it is negative if it flows out of the body. If no work is done on the system, then the change in energy is simply

$$\frac{dE}{dt} = \frac{dQ}{dt}\,. \tag{13}$$

The specific heat, or *heat capacity* C, is defined by Ref. [27] as "the quantity of heat which must be gained in order to raise the temperature of the body by one unit", and can be written as

$$C = \frac{dQ}{d\Delta T} = \frac{dQ}{dt}\frac{dt}{d\Delta T} \ ,$$

$$C\frac{d\Delta T}{dt} = \frac{dQ}{dt} \ . \tag{14}$$

A microbolometer is mostly thermally isolated from any heat sink, only connected by two support arms, as shown in Figure 2. In this design, the positive heat in to the detector is the *incident radiant energy,* P_i, and the heat out of the detector is the conduction loss through the arms and by radiation. The conduction loss is governed by the *thermal conductance* G, measured in W/K, which is a function of material properties and geometry. For this system, the heat $\frac{dQ}{dt}$ is

$$\frac{dQ}{dt} = \eta P_i - G\Delta T \ , \tag{15}$$

where $0 < \eta < 1$ is the absorbtance of the detector film describing the amount of incident power that is absorbed by the film, and ΔT represents the change in temperature between the VO_x detector and the heat sink.

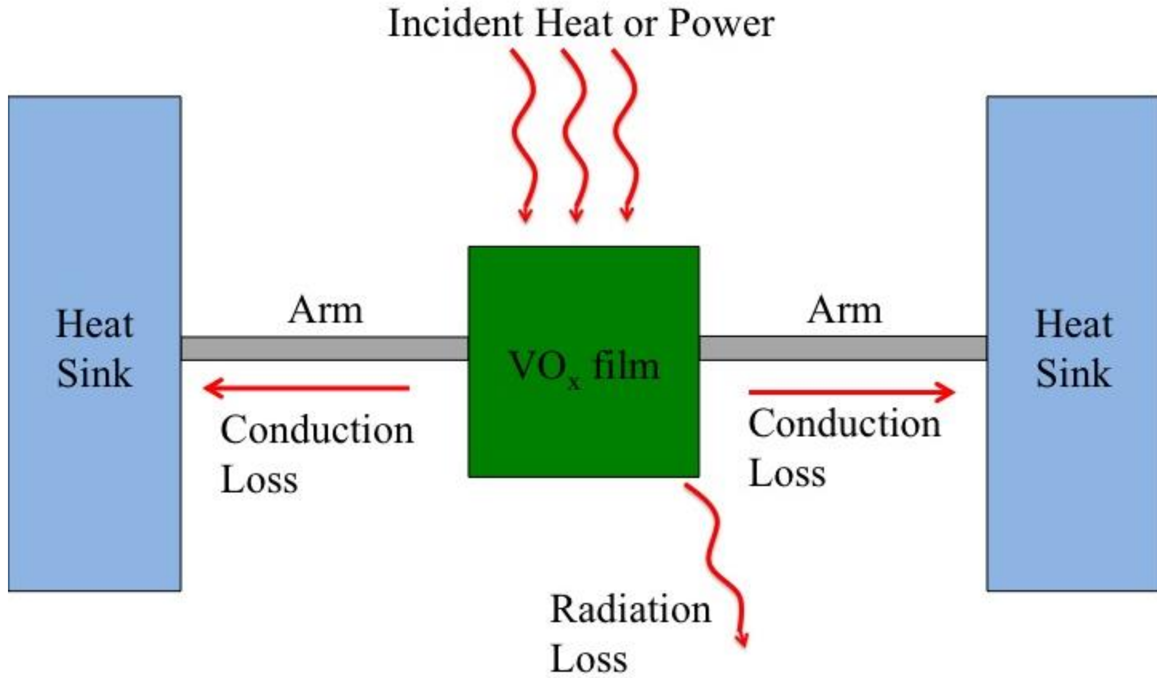

Figure 2. Thermal schematic for a bolometer. Energy comes in to the detector by radiation from the source, energy leaves by conduction through the two arms and by radiation.

Combining Eqs. 14 and 15 gives

$$C\frac{\partial(\Delta T)}{\partial t} + G\Delta T = \eta P_i \; . \tag{16}$$

Eq. 16 is called the *heat-balance equation*. The assumption is made that the incident power is modulated such that $P_i = P_i e^{i\omega t}$, where $\omega = 2\pi f$ is the frequency of modulation. In practice, this is achieved by using an optical chopper in front of the detector.

One additional source of heating in the device is bias heating, also known as *Joule heating*, or i^2R heating. To understand this, a brief description of the measurement technique is necessary. To measure a change in resistance of the microbolometer, the detector is DC-

biased with a constant current source. The resistance deviation is determined from the deviation in potential across the detector, $\Delta R \propto \Delta V$. The simplest and most direct way to do this is to use a voltage divider circuit, shown in Figure 3. A low-noise DC voltage source applies a constant current. The detector is in series with an impedance-matched resistor R_L, such that the voltage across the resistor is

$$V_{out} = V_B \frac{R}{R_L+R} \, . \tag{17}$$

Differentiating Eq. 17 with respect to a change in resistance yields

$$dV_{out} = V_B \frac{R_L}{(R_L+R)^2} dR \approx \frac{V_B}{4}\frac{dR}{R} \, , \tag{18}$$

where the approximation $\frac{R_L}{(R_L+R)^2} \approx \frac{1}{4R}$ is appropriate for $R \approx R_L$, as is designed in the circuit.

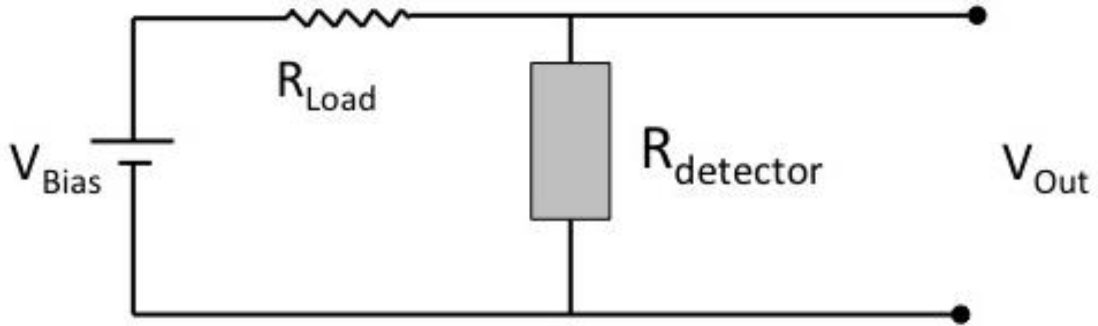

Figure 3. Schematic for a voltage divider circuit used to measure ΔV across the detector, and by extension, measure ΔR.

The heat balance equation can now be adjusted to include the Joule heating term as

$$C\frac{\partial(\Delta T)}{\partial t} + G\Delta T = \eta P_i + i^2R = \eta P_i e^{i\omega t} + \frac{V_B^2 R}{(R_L+R)^2}\,. \tag{19}$$

In the absence of external heating ($P_i = 0$) the steady-state solution to Eq. 19 is

$$G_0\Delta T = i^2R = \frac{V_B^2 R}{(R_L+R)^2}\,. \tag{20}$$

G_0 is the average thermal conductance of the material at temperature *T*. The Joule heating term depends upon resistance, which of course is a function of temperature. Therefore, in the dynamic heat balance equation with external heating the Joule heating term is $\frac{d(i^2R)}{dT}$, which is solved as

$$\frac{d}{dT}(i^2R) = \frac{d}{dR}(i^2R)\frac{dR}{dT} = \frac{d}{dR}\left(\frac{V_B^2 R}{(R_L+R)^2}\right)R\alpha = \alpha\frac{V_B^2 R}{R_L+R}\frac{R_L-R}{(R_L+R)^2}\,. \tag{21}$$

The heat balance equation with Joule heating becomes

$$C\frac{\partial(\Delta T)}{\partial t} + G\Delta T = \eta P_i e^{i\omega t} + \frac{V_B^2 R}{(R_L+R)^2}\frac{R_L-R}{R_L+R}\alpha\Delta T\,, \tag{22}$$

Using the steady state solution in Eq. 20, Eq. 22 can be written as

$$C\frac{\partial(\Delta T)}{\partial t} + \left\{G - G_0\Delta T\alpha\frac{R_L-R}{R_L+R}\right\}\Delta T = \eta P_i\,. \tag{23}$$

The term in the brackets is defined as the effective thermal conductance G_{eff}. The heat balance can finally be written as

$$C\frac{\partial(\Delta T)}{\partial t} + G_{eff}\Delta T = \eta P_i e^{i\omega t} \ . \tag{24}$$

Eq. 24 is an inhomogeneous first-order differential equation, which seeks a solution of the form $\Delta T = Ae^{i\omega t}$. Solving this equation yields

$$\Delta T = T_0 e^{-\frac{G_{eff}}{C}t} + \frac{\eta P}{G+i\omega C}. \tag{25}$$

The first term in Eq. 25 is a transient term, which, provided $G_{eff} > 0$, will tend towards zero. The latter term is the periodic dependence that is related to the modulation frequency of the incident power, that is, it is the desired signal to observe. The magnitude of the change in temperature is found from the real part of Eq. 25, and is

$$|\Delta T_d| = \frac{\eta P_i}{G\sqrt{1+\omega^2\tau_{th}^2}} \ , \tag{26}$$

where the ratio of heat capacity C to the thermal conductance is defined as the *thermal time constant*, as

$$\tau_{th} = \frac{C}{G_{eff}}. \tag{27}$$

2.2.3 Responsivity of a Microbolometer

The responsivity of a microbolometer is defined as the ratio of the measured response to incident power. Specifically, voltage responsivity $\mathcal{R}_v$ is the measured change in voltage divided by the incident power, $\frac{dV_{out}}{P_i}$. The measurable signal voltage is given in Eq. 18.

The definition of TCR in Eq. 9 can be rewritten as $\frac{dR}{R} = \alpha dT \approx \alpha \Delta T$. This is combined with Eq. 26 and substituted into Eq. 18 to give

$$dV_{out} = \frac{V_B \alpha \eta P_i}{4G_{eff}} \frac{1}{\sqrt{1+\omega^2 \tau_{th}^2}}. \tag{28}$$

The voltage responsivity $\mathcal{R}_v$ is

$$\mathcal{R}_v = \frac{V_B \alpha \eta}{4G_{eff}} \frac{1}{\sqrt{1+\omega^2 \tau_{th}^2}} . \tag{29}$$

According to Eq. 29, the voltage responsivity of a detector is dependent upon 6 parameters: (1) applied bias voltage, (2) the TCR of VO_x, (3) device absorption, (4) effective thermal conductance, (5) modulation frequency, and (6) heat capacity. The applied bias and the modulation frequency are independent upon device design. The heat capacity effects performance only if the thermal time constant $\tau = \frac{C}{G_{eff}}$ is long compared to the modulation frequency; for $\tau \ll \omega$ the effect of heat capacity on responsivity is negligible (this will be discussed later in relation to measurements of thermal time constants in fabricated devices). Hence, the three parameters that can optimize the responsivity are TCR, absorption and thermal conductance.

2.3 Noise Considerations

Noise is inherent in any detection system, and is a result of random fluctuations in various components of the system. Noise in an infrared detector can be found in each of three

components of the system: photon flux, detector, and amplifier/electronic read-out. The scope of this work will focus on detector noise, which in general will have the largest contribution to total system noise, and is the limiting factor in the total noise of the system.

Many noise sources are independent of the electronic frequency; these are called *white noise*. Common types of white noise are Johnson Noise, Thermal Fluctuation Noise (phonon noise), and Background Fluctuation Noise (photon noise). Some sources of noise depend upon frequency. An example of so-called *pink noise* is 1/f noise, named simply by the relationship between noise voltage and frequency domain. There is often a noise peak at 60 Hz and harmonics of this value, which comes from cross-talk effects from supplied AC electrical power. Other common types of detector noise include shot noise and generation-recombination noise; these only relate to photon detectors however. The four main types of noise for a microbolometer are Johnson noise, thermal fluctuation noise, background fluctuation noise, and 1/f noise.

2.3.1 Johnson Noise

Johnson noise (sometimes referred to as Johnson-Nyquist noise) is essentially a thermal effect; it is derived from the fluctuations in thermal motion of charge carriers in a resistor. These fluctuations give rise to a variation in the total resistance of the material, and thus to the potential across this resistor. Johnson noise is only present for detectors that need an external bias, which of course includes the microbolometers under investigation. The mean RMS voltage fluctuation for Johnson noise is given by [24]

$$\delta V_j = \sqrt{4k_B TR\Delta f}, \tag{30}$$

where Δf is the electronic measurement bandwidth, which is related to the measurement integration time τ_e as

$$\Delta f = \frac{1}{2\tau_e}. \tag{31}$$

To reduce Johnson noise, the detector can be cooled using a Peltier device, or even cryogenically, but would no longer be an uncooled detector, which is desired for low cost and low power consumption. As the detector heats up (from the scene or Joule heating) this noise will increase, however the temperature change, given by Eq. 26, will be $\Delta T \sim \frac{P}{G}$, where *P* here is generalized to the absorbed power by any method. As incident power is typically in the nanowatt range, and thermal conductance is typically ~10^{-7}-10^{-6} W/K, the temperature change will generally be limited to ~1 K or less, an increase of 0.3% from ambient temperature. The increase in noise therefore would be ~0.17%, which would likely be below the noise floor of other noise sources, and can be considered negligible.

It can be concluded that for an uncooled detector with a specific bandwidth, the only way to reduce the Johnson noise is to reduce the resistance of the detector, and the noise reduces by $\sqrt{R}$.

2.3.2 Thermal Fluctuation Noise and Background Fluctuation Noise

Thermal fluctuations arise from the exchange of heat between different bodies. This effect is not necessarily dependent upon a difference in temperature; small heat exchanges will occur between thermally connected bodies *even if they are at the same temperature*, provided the net exchange of heat is zero [10]. This arises from random fluctuations and collisions of particles, modeled as harmonic oscillators, through thermal conduction paths. Specifically, any heat exchange by means of conduction or convection is called *thermal fluctuation noise*, while heat exchange by means of radiation only is called *background fluctuation noise*. The latter is considered to be the ultimate limit of performance for a thermal detector, and is not a possible noise floor as some thermal conduction must be present for the device to function.

The thermal fluctuation noise can be derived from the solution to a general case of the heat balance equation (Eq. 16) in which the power will be considered to be from any source. The solution will look similar to Eq. 26, but written in terms of the mean square fluctuation of temperature, such that

$$\overline{\Delta T^2} = \frac{\overline{\Delta P^2}}{G^2+\omega^2 C^2} \,. \qquad (32)$$

Thermal fluctuations are white noise. To account for this Eq. 32 is integrated over all electronic frequencies f. Considering $\omega=2\pi f$ and $\int_0^\infty \frac{dx}{a^2+b^2x^2} = \frac{1}{ab}\tan^{-1}\left[\frac{bx}{a}\right]\Big|_0^\infty$ this integral solves as

$$\overline{\Delta T^2} = \frac{\overline{P^2}}{4GC}. \tag{33}$$

The mean square temperature fluctuations can also be solved for considering the mean square energy fluctuations of a canonical system possessing many degrees of freedom [10, 28]

$$\overline{\Delta T^2} = \frac{kT^2}{C}. \tag{34}$$

Eq. 34 is equated to Eq. 33 to solve for the mean square fluctuations in power. This is then substituted into Eq. 32 to obtain the RMS temperature fluctuation for the detector[24],

$$\sqrt{\overline{\Delta T^2}} = \frac{\sqrt{4kGT^2\Delta f}}{G\sqrt{1+\omega^2\tau_{th}^2}}. \tag{35}$$

Combining the voltage differential (Eq. 18) with the definition of TCR (Eq. 9) gives

$$dV_{out} = \frac{V_B}{4}\alpha dT. \tag{36}$$

This equation was utilized to describe the voltage responsivity as a function of the change in temperature due to incident power; however it can also be used to describe the noise voltage for the temperature fluctuations. A substitution of the temperature fluctuation for *dT* gives the RMS voltage fluctuations for thermal fluctuation noise

$$\delta V_{TF} = \frac{V_B}{4}\ \alpha \frac{\sqrt{4kGT^2\Delta f}}{G\sqrt{1+\omega^2\tau_{th}^2}} = \sqrt{\frac{4kGT^2\Delta f\mathcal{R}^2}{\eta^2}}\,, \tag{37}$$

where the term on the right utilized the defined voltage responsivity from Eq. 29.

The most straightforward analysis of temperature fluctuation noise is from Eq. 35, in which it is clear that the only way to minimize thermal fluctuation noise is through thermal isolation.

Background fluctuation noise can be derived by replacing the thermal conductance G in Eq. 35 or 37 with the thermal conductance by radiation, Eq. 7,

$$\delta V_{BF} = \sqrt{\frac{16k\sigma A_d T^5\Delta f\mathcal{R}^2}{\eta}}\,, \tag{38}$$

where Kirchhoff's Law ($\eta = \epsilon$) is utilized [24]. It should be noted that $\mathcal{R}_v^2 \propto \eta^2$, so there is no dependence on absorbtance for thermal fluctuation noise, but $\delta V_{BF} \propto \eta^{\frac{1}{2}}$.

2.3.3 1/f Noise

A noise source present in microbolometers but that is poorly understood is 1/f noise, so called due to its experimentally-determined dependence upon frequency. This type of noise is related to slow fluctuations in the resistance of a material, and is therefore proportional to the bias current or bias voltage applied across the resistor. This noise is material dependent; differences in material, deposition technique, dimensions, and the

quality of electrical contacts can affect 1/f noise by orders of magnitude [25]. In particular, 1/f noise is affected by film imperfections and non-ohmic contacts [24].

1/f noise is present at any and low electrical frequencies, regardless of the modulation frequency of the detector. It is advantageous, therefore, to operate a detector at a frequency above the 1/f noise floor; further reduction of 1/f noise can be achieved by using an amplifier circuit with a high-pass filter to as a DC-block. There is no complete analytical derivation or description of 1/f noise, but experimental observations indicate that the mean square voltage magnitude in a 1 Hz electrical bandwidth is approximately [10]

$$V_{1/f} = \sqrt{\frac{\left(\frac{V_B R}{R_L + R}\right)^{\sim 2} k_f}{f^{\sim 1}}}, \tag{39}$$

where k_f is the 1/f parameter, related to the Hooge parameter α_H by

$$k_f = \frac{\alpha_H}{nV}, \tag{40}$$

where n is the mobile charge carrier density and V is the volume of the film [25]. For VO_x microbolometers (TCR ~-2.0%) developed at Honeywell, R.A. Wood reports a typical value of $k_f \approx 1 \times 10^{-13}$ [25].

Basantani et al. [29] report measurements for the normalized Hooge parameter α_H/n in cm^3 for microbolometers using a variety of thin films, including hydrogenated amorphous silicon, mixed phase hydrogenated amorphous germanium and amorphous VO_x, both doped and undoped. For high resistivity films (>10^4 Ω-cm) they find $\frac{\alpha_H}{n} \approx 10^{-20} -$

$10^{-17}\ cm^3$, while films with resistivity between 0.1-1 Ω-cm have $\frac{\alpha}{n} \approx 10^{-22}\ cm^3$. They find that the Hooge parameter is related to fluctuations in carrier mobility, which is in itself dependent upon material and specifically imperfections in that material.

It should be stressed that the magnitude of 1/f noise is unique to each device and is dependent upon the *quality* of the electrical path in the detector. This analysis really only investigates the 1/f noise in the VO_x film, however 1/f noise will be present in all of the electrical contacts from the detector to the voltmeter, the most significant of which probably would be the isolation arms that connect the pixel to the substrate heat sink. This can increase the measured value of 1/f noise by orders of magnitude above approximated calculations.

2.3.4 Total System Noise

Noise voltages add in quadrature, so that the total system noise is given by

$$V_{N,Total} = \sqrt{V_j^2 + V_{TF}^2 + V_{BF}^2 + V_{1/f}^2}\ . \tag{41}$$

Figure 4 presents the calculated noise voltage per unit root bandwidth for each of the four main types of detector noise in a microbolometer based off of typical parameters. In these calculations, $T=300K$, $\Delta f=30\ Hz$, the TCR $\alpha=-2.0\%$, thermal conductance $G=5.0 \times 10^{-7}\ W/K$, thermal time constant $\tau_{th} = 5\ ms$, absorbtance $\eta=0.9$, and the detector has an area $A_d= 35 \times 35\ \mu m^2$ with a thickness of $t=100\ nm$. The applied bias voltage $V_B = 1V$. The

normalized Hooge parameter $\frac{\alpha_H}{n} = 1.225 \times 10^{-23}\ cm^3$ is chosen based upon earlier analysis, but uncertainty in this number could shift the 1/f curve vertically by as much as an order of magnitude. By this chosen approximation the 1/f noise dominates at low frequencies, while Johnson noise dominates above 10 Hz for a 200kΩ detector; this point is sometimes referred to the *knee* [10]. If the resistance of the detector were to drop to 50 kΩ, the 1/f knee extends to 30 Hz, which is typically the video frame rate. Background fluctuation noise is quite small, and thermal fluctuation noise has some slight dependence in frequency from the thermal response term in Eq. 37. Such a device (both 50 kΩ and 200 kΩ detectors) would be said to be Johnson noise limited, as this is the dominant noise source for standard operating frequencies.

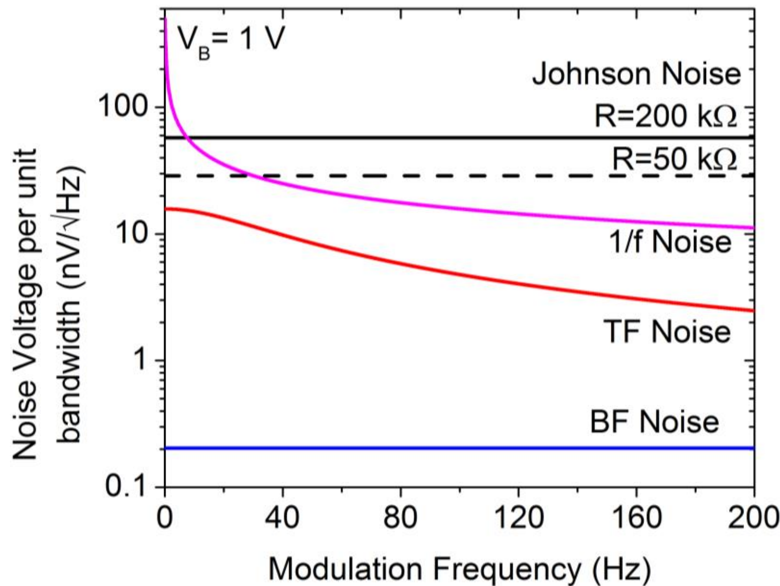

Figure 4. Noise voltage per unit root bandwidth for each of the four main types of detector noise as a function of modulation frequency at 1V applied bias.

The applied bias does not affect Johnson noise but it has an impact on the other noise sources. The RMS temperature fluctuation in a device is independent of bias voltage, but a greater applied bias will result in a greater voltage response to temperature. This affects the desired voltage responsivity in a positive way, however the noise voltage due to background fluctuations and thermal fluctuations increases as well. Figure 5 presents the noise voltage per unit root bandwidth as a function of applied bias voltage at a 30 Hz modulation frequency. For a 200 kΩ resistor, the detector is Johnson-noise limited up to 2.0V, however beyond this point the 1/f noise begins to dominate. For a detector with lower resistance, 1/f noise dominates at only ~1V, as was shown in Figure 4. Temperature fluctuation noise dominates beyond Johnson noise above ~4V applied bias at a 30 Hz modulation frequency.

The optimal applied bias is hence the maximum bias that still keeps the detector Johnson noise limited; based upon these calculation this is approximately 2V for the 30 Hz frequency. Another approach would be to measure the detector at higher frequencies. An 80 Hz modulation frequency would allow for higher applied bias while remaining Johnson-noise-limited, and is sufficiently above the common noise feature 60 Hz.

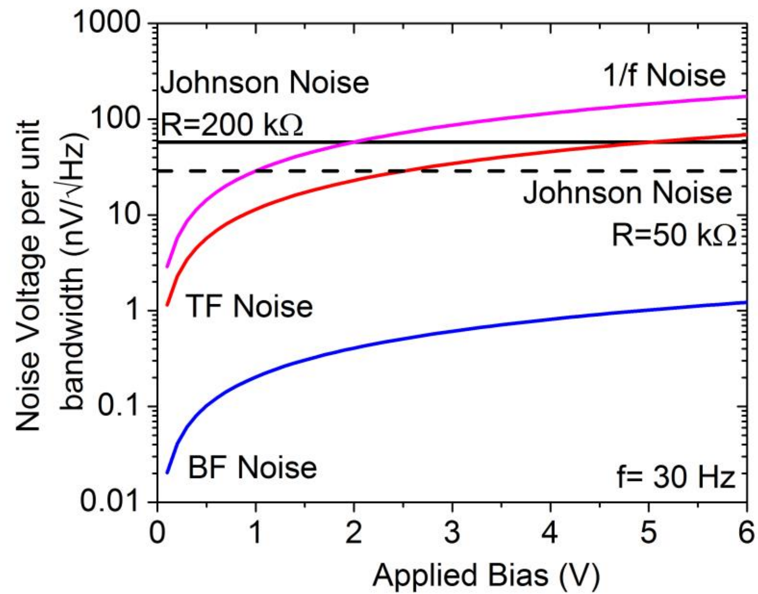

Figure 5. Noise voltage per unit root bandwidth for each of the four main types of detector noise as a function of applied bias voltage.

2.4 Optimization Techniques

The previous two sections have described the factors that influence detector performance. Microbolometers can be characterized and compared based upon the signal to noise ratio (SNR) for a given incident power. Higher SNR for a given incident power indicates a better device. Hence, improving device performance means increasing responsivity and/or decreasing noise. Parameters to optimize are the TCR and resistivity of the VO_x film, the thermal conductance G of the detector, and the absorbtance η of the detector.

2.4.1 TCR and Resistivity

The resistance of a vanadium oxide film is heavily dependent upon temperature and stoichiometry. Crystalline VO_2 has a sharp metal-to-insulator transition (MIT) at 68˚C that can be utilized for a number of devices [30]. Different stoichiometric configurations of vanadium oxide show this transition occurs at different temperatures [31]. However, these phase transitions are hysteretic [32], and such a non-linear effect is not desirable for infrared imaging systems.

Amorphous VO_x films for microbolometers were developed by Honeywell [25]. These films show a linear TCR over a broad range of temperatures. The value of the TCR is closely related to the resistivity; this relationship is given by $TCR \propto Log(\rho)$ (see Figure 6). To maximize responsivity, TCR must be increased; unfortunately increasing TCR also increases resistivity, which increases Johnson noise. For microbolometers, VO_x films generally have a TCR between -2.0% and -3.0%, with a resistivity between 0.1-1 Ω-cm [4].

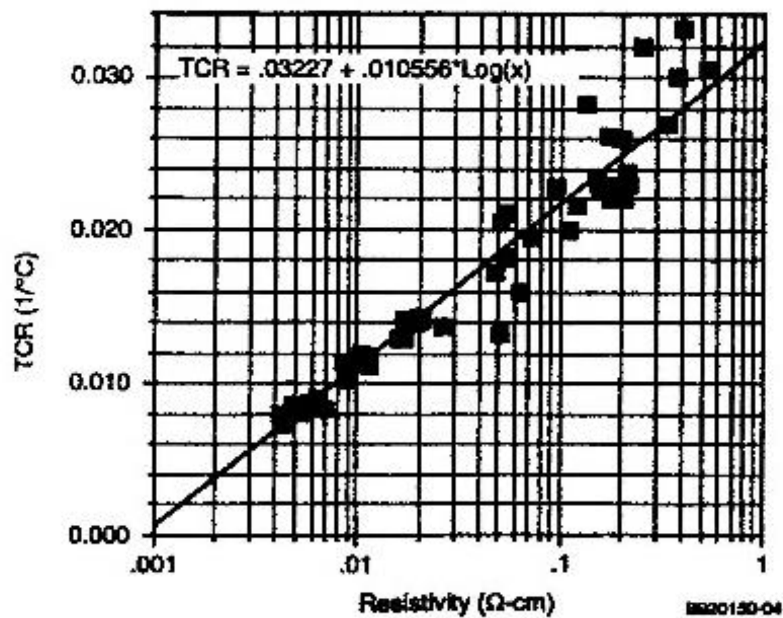

Figure 6. TCR as a function of resistivity for VO_x films [25]. Reprinted from Uncooled Infrared Imaging Arrays and Systems, Semiconductors and Semimetals Vol. 47, Wood, R.A., Monolithic Silicon Microbolometer Arrays, page 55, Copyright 1997, with permission from Elsevier and Academic Press.

In part, VO_x can be characterized by the value of x, that is, by the ratio of vanadium to oxygen in the film [33]. Typically, these films have $1.5 < x < 2$ [4, 8, 10, 34, 35]. As x increases, the film becomes more insulating, and the TCR goes up. As x gets smaller, the film is more metallic, and the TCR is low. This content is heavily dependent upon deposition parameters.

2.4.2 Thermal Conductance

Detector performance is heavily dependent upon how well thermally isolated it is. The higher the thermal isolation, the more the detector will change in temperature. If a detector

is not well isolated, then any incident power will flow out of the detector too quickly and will not allow the detector to increase its temperature for a sufficient resistance change. Low thermal conductance is thus desirable.

Thermal conductance also effects responsivity by way of the thermal time constant in the $\frac{1}{\sqrt{1+\omega^2\tau^2}}$ term found in Eq. 29. In this case, it is not simply the thermal conductance, but the ratio of heat capacity to thermal conductance that is important. To mitigate this term and give high performance, one may suggest choosing a low operating frequency such that $1+\omega^2\tau^2 \sim 1$, which is possible even for high thermal time constants. Indeed, some kinds of sensors, such as pyroelectric-based motion detectors, are designed to operate at frequencies of 1 Hz or even less [36]. However, this constraint is not suitable for an IR imaging system if the desire is to operate at video frame rates, as is typical. For a 30 Hz frame rate $\omega = 2\pi f = 188.5\ s^{-1}$. For a thermal time constant of 1 ms, the term $\frac{1}{\sqrt{1+\omega^2\tau^2}} = 0.98$. At 10 ms, this term drops to 0.47. For the fastest frame rate, it is desirable to decrease heat capacity instead of increasing thermal conductance if possible.

The device considered consists of the VO_x film encapsulated between two identical dielectric layers and connected to the substrate by two metal arms. The thermal conductance and heat capacity can be determined by device geometry and material properties as [37]

$$C = c_i \rho_i t_i A_d \,, \qquad (42)$$

where C is the heat capacity determined by specific heat c_i, density ρ_i, thickness t_i and area A_d of the VO_x and dielectric layers, and [38]

$$G = \frac{2gtw}{l}, \tag{43}$$

where G is the thermal conductance through the two arms of the microbolometer, which is determined by arm geometry (t, w, and l) and the thermal conductivity g of the metal.

Total thermal conductance is, of course, not just limited to heat transfer through the arm, but also by radiation (Eq. 7) and by conduction through the air. The latter can be the greatest source of heat loss in a detector. Devices in air at atmospheric pressure will have a conductance given by [37]

$$G_{air} = \frac{g_{air}A_d}{d}, \tag{44}$$

where $g_{air}=0.0257\ W/mK$ and d is the air gap between the detector and the substrate. To remove this thermal path detectors are usually operated in vacuum. It has been shown that at pressures under 100mTorr the thermal conductance of air will be negligible compared to the thermal conductance through the arms [39, 40].

Thermal Conductance through the arms of a microbolometer as a function of arm length is presented in Figure 7. For this calculation, arms are set to be 4µm wide and 100 nm thick 80/20 nichrome (NiCr), chosen for its low thermal conductivity of 11.3 W/mK [41]. By increasing the arm length from 1µm to 20 µm, thermal conductance is reduced by a factor of ~15, increasing arm length from 20 µm to 100 µm further reduces the arm length a factor

of 5. Beyond this concerns about mechanical stability outweigh the benefits of a marginal decrease in thermal conductance.

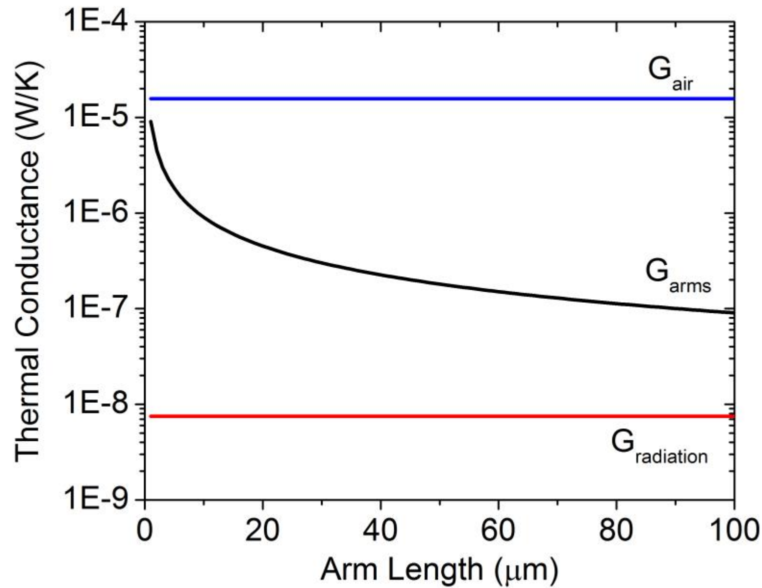

Figure 7. Thermal Conductance through microbolometer support arms as a function of arm length, compared with the limits of radiation and conduction of air at atmospheric pressure.

2.4.3 Absorptance

All light incident upon the detector will either be reflected, transmitted or absorbed. These quantities can be defined as the reflectance, transmittance and absorbtance, such that the sum of these quantities at any given wavelength will be one. To improve the efficiency of the detector it is desired to maximize the amount of light absorbed by the detector in the desired bandwidth of operation. Thus device performance can be improved by increasing the magnitude of the absorbtance and/or increasing the bandwidth in which absorbtance is

high. LWIR is generally the desired bandwidth for uncooled microbolometers, as microbolometers will likely never reach the performance of an uncooled photoconductor (such as lead selenide) in the MWIR [24]. However, a microbolometer that performs well in *both* LWIR and MWIR would be desirable. Common techniques to increase absorbtance include the use of a: (1) Fabry-Perot quarter wave cavity, (2) thick dielectric layer, (3) metal black layer, and (4) plasmonic resonant structure.

2.4.3.1 Fabry-Perot Quarter Wave Cavity

A quarter wave cavity is a common method of achieving high absorption in an infrared detector [4, 42-44]. The basic principle is quite simple: light that is transmitted through a detector exits the bottom plane of the detector and enters the resonant cavity. The light travels a distance $\frac{\lambda}{4}$ through the cavity. At the other end of the cavity is a near perfect reflector, generally a thick metal. Upon reflection off of this metal the light has an 180° phase shift, and then travels a distance $\frac{\lambda}{4}$. The result is a standing wave with a maximum at the bottom surface of the detector. In practice, the material in the detector affects the optical path length of the light, so that the given explanation is adjusted so that the standing wave maximum, and hence the maximum absorption, occurs at wavelengths of $\frac{\lambda_x}{4}$, where λ_x is the index-dependent wavelength of light in the material [4]. Detectors using this method can achieve high absorption at a particular designed wavelength. This approach does not necessarily give a narrow band of absorption, but the bandwidth is limited based upon design parameters.

A plot of the simulated reflectance spectrum for a quarter wave cavity design is shown in Figure 8. This simulation was done using GD-Calc [45], a Mat-Lab based electromagnetic simulation software package that utilizes Rigorous Coupled-Wave Analysis (RCWA). The simulated stack consists of a 100 nm Au reflector, a 2 μm air gap, and the $SiO_2/VO_x/SiO_2$ device with thicknesses of 300 nm/100nm/300nm. Index values for VO_x are based off of ellipsometry measurements from a witness sample of VO_x. The transmittance in this simulation is ~0; the absorptance can be assumed to be unity less the reflectance.

The calculated spectrum shows little or no absorption occurring in the MWIR. The peak of the absorptance of 93% is at 9.3 μm, which is due to the absorption band of SiO_2. The secondary peak at 12.9 μm of 82% is the Fabry-Perot resonance from the cavity. The average absorption in the LWIR is 71%.

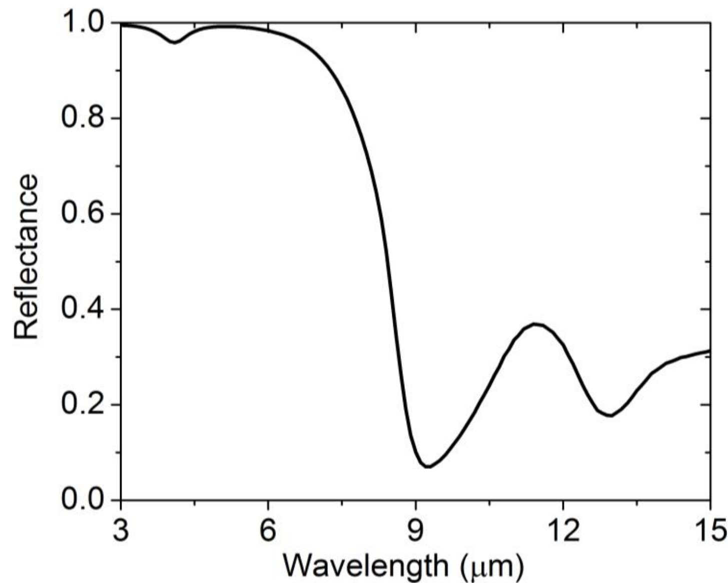

Figure 8. Simulated reflectance spectrum of quarter wave cavity.

2.4.3.2 Thick Dielectric Layer

Dielectrics, such as silicon dioxide and silicon nitride, can have absorption peaks in the infrared. Silicon dioxide has a peak around 8.3 μm [46] and silicon nitride has a peak at 11.7 μm [47]. It is possible to deposit a mixture of these two dielectrics (silicon oxynitride) which can have different absorption spectra altogether, achieving desired absorption peaks. To achieve high absorption, however, the thickness of the layers must be quite thick, resulting in a high heat capacity C of the detector, and a high thermal time constant by extension.

2.4.3.3 Metal Black Layer

Metal blacks have been investigated as mechanisms for achieving high absorption [18, 21, 36, 48, 49]. These films are pure elemental metals, but are arranged in porous, web-like structures with large voids. These voids cause scattering within the material, as light is internally reflected multiple times in random and varied geometric planes. Pfund first discovered metal blacks by depositing bismuth films at ~250 mTorr pressure in an inert gas [50]. At this high pressure, he concluded that deposited particles did not easily align to existent lattice structures in a film, and therefore were loosely bound to each other. Marshall et al. used platinum black for high emissivity surfaces in pyroelectric detectors fabricated for Honeywell [51]. They achieved this by electroplating platinum at a rapid deposition rate. They noted that when the rate is too low, the Pt atoms adhere to the structure of the substrate and form a smooth, reflecting film, but at higher rates the atoms

are deposited in a disordered fashion. Becker et al. evaluated gold black films for absorption between 15-700 μm [21], and observed that the absorption decreases at higher frequencies. This can be explained both in terms of the size of the voids and in terms of the conductivity of the film.

Gold black is a good absorber for infrared because it has a high absorption over a broad spectral range and it has a low heat capacity due to its porosity [17]. Coatings are easily achieved using an ordinary thermal evaporator, which suggests the possibility for multiband sensors fabricated using a single material with minimum fabrication tolerances. On the other hand, this material is extremely fragile, which makes it difficult to integrate on a microbolometer array as typical fabrication processes destroy the film. Recently, a process to pattern gold black using standard photolithography and lift-off techniques has been demonstrated [22], which has influenced the choice of this material in this work to optimize the absorbtance of the microbolometer.

2.4.3.4 Plasmonic Resonant Structures

The field of plasmonics is the study of the interaction between light and structured subwavelength elements, defined by their complex electrical permittivity $\epsilon(\omega)$ and magnetic permeability $\mu(\omega)$. Plasmonic structures, sometimes referred to as resonant structures or metamaterials, are good candidates for electromagnetic wave absorbers because they depend on the geometry of the structure [15]. As such, these structures can be tailored to achieve absorption at almost any frequency, considering fabrication

constraints, and have been shown to function from mm-waves through the visible spectrum. Structures are structured from highly conducting metals, and are typically arranged into periodic structures. As light interacts with the metallic structure, it creates a resonating dipole, which will then interact with adjacent dipoles and cause them to resonate. This results in the propagation of electron oscillations, commonly referred to as surface plasmons.

A 'metamaterial perfect absorber' (MPA) consists of a metal ground plane and dielectric layer, with a periodic, metallic metamaterial above a metal ground plane and separated by a dielectric layer [15]. For a metal such as gold, the dielectric function (relative permittivity) is given by [52]

$$\epsilon(\omega) = \epsilon_{\infty} - \frac{\omega_p^2}{\omega^2 + i\gamma\omega}, \tag{45}$$

where the plasma frequency is $\omega_p = \frac{ne^2}{\epsilon_o m}$ and γ is the damping frequency associated with collisions, which is the inverse of the relaxation time for a free electron gas, and ϵ_{∞} is the static permittivity at infinite frequency. For a simple metal-dielectric interface, the wave vector of a surface plasmon is given by

$$k_x = \frac{\omega}{c}\sqrt{\frac{\epsilon_m + \epsilon_d}{\epsilon_m \epsilon_d}} \tag{46}$$

The dispersion relation of a material can be represented as a plot of the wave vector in frequency space. Thus, the frequencies at which the specific modes of a periodic resonator

intersect with the dispersion relation of the material are the frequencies at which light will couple in to the material; that is, where absorption will be highest.

Such absorbers can obtain can obtain a very high absorbtance, but typically only in a narrow band. Liu et al. developed a metal-dielectric-metal (MDM) structure by placing a periodic array of gold disks (350 nm diameter by 20 nm thick) on a layer of Au/MgF_2 200nm/30nm [14], which resulted in an absorbtance of 0.99 at a frequency of 185 THz (~1.67 μm), although the full width half maximum (FWHM) of this peak is only ~30 THz (~1.5-1.7 μm absorption band).

Plasmonic metamaterials have been integrated with microbolometers and shown signal enhancement. Erturk et al. [53] patterned an array of concentric C-shaped patterns of gold onto silicon nitride on a standard microbolometer and measured an 18% increase in absorption. The unit cell of these absorbers was 5 x 6 μm^2, and the critical dimension was 600nm, which is below the limitations of standard UV photolithography. In contrast, Ogawa et al. [54] made features large enough to be compatible with standard photolithography. They etched holes of 3 μm in diameter and a depth of 1.2 μm into a dielectric film and deposited an overcoat of gold. By altering the period of these holes from 4 μm to 6.5 μm they were able to shift the peak absorbtance from 4 μm to 6.5 μm, matching the periodicity, although the absorbtance was 30% less for the highest wavelength. Zhu et al. [55] designed an absorber to minimize heat capacity. Unlike other plasmonic absorbers, which generally consist of ~1 μm dielectric, they deposited only 200 nm silicon nitride and patterned 20 nm strips of gold of dimension 1.5 μm x 0.15 μm.

While the absorption of this film only achieved 45%, the minimal increase in heat capacity makes this approach attractive.

The optimization goals in the implementation of such a plasmonic resonant structure is to maximize the absorptance over a wide bandwidth through multiple absorption peaks. While some heat capacity increase is expected, keeping this effect minimal is important for device response time.

2.5 Measurement Techniques

2.5.1 Testing Schematic

Detectors are measured and characterized in a typical blackbody test configuration [24]. The schematic for this configuration is shown in Figure 9. A calibrated blackbody source (IR-301 Infrared Systems Development Corporation) is used as the power source. This uses a cavity configuration with an active PID controller to maintain a stable temperature to within 0.1˚C, and can reach temperatures up to 1200˚C. For testing described in this work temperatures ranged between 300˚C-500˚C. The blackbody is set a distance *r=14-24 cm* away from the detector, and the power from the blackbody is modulated using an optical chopper to frequencies between 10 Hz-160 Hz.

Detectors were connected via patterned metal traces on the substrate to large gold bond pads. These bond pads were wire bonded to standard chip carriers using aluminum wire. These chip carriers were placed in a vacuum box with electrical feedthroughs. The box

has a Thallium Bromo-Iodide (KRS-5) window, which has a transmission of ~70% from 0.6-40 μm wavelength. This box was pumped down to ~20 mTorr before any testing commenced to reduce the thermal conductance through air.

The detector is connected to a simple voltage divider circuit shown in Figure 3. Bolometer and load resistances were matched $R_L \approx R$, and the circuit was biased with a low-noise DC source. Based upon noise concerns raised earlier, the bias voltage was maintained between 1-3V. The modulation in V_{out} due to the chopped incident IR irradiance is the quantity dV_{out} (Eq. 28), which was synchronously amplified using a lock-in amplifier (Stanford Research Systems SR530 analog and SR850 digital) with a 30 ms integration time constant. The modulation frequency was referenced via an output from the optical chopper. A spectrum analyzer (HP 3585) was also used to identify the power spectrum of the noise. This was particularly useful in identifying noise features such as 1/f noise and 60 Hz noise. Information from the spectrum analyzer, along with the discussed noise concerns, influenced the decision to measure detectors initially at an 80 Hz chopping frequency.

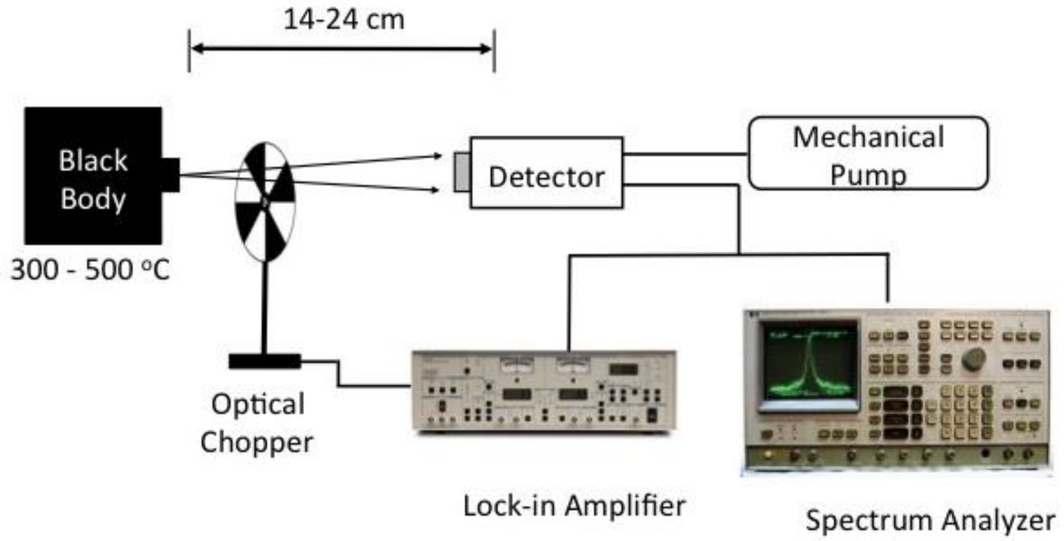

Figure 9. Schematic of device test configuration.

To characterize the noise [56], the incident blackbody irradiance was blocked by a shield, whose highly reflecting surface faced the blackbody, and whose blackened surface faced the bolometer. The noise is the output voltage variation measured using the lock-in amplifier with a time constant of 30 ms.

Measurements of the thermal time constant were made by taking advantage of the frequency dependence of the voltage responsivity in Eq. 29, that is, $\mathcal{R} \propto \frac{1}{\sqrt{1+\omega^2\tau_{th}^2}}$. Solving Eq. 29 for τ_{th} gives

$$\frac{1}{2\pi}\sqrt{\frac{R_0^2}{R_v^2}-1} = \tau_{th}f \tag{47}$$

where R_0 is responsivity when $f = 0$. When the function of responsivity on the left is plotted as a function of chopping frequency, the slope of the linear fit gives the thermal time constant.

2.5.2 Derivation of Incident Power

A blackbody source may be approximated as a collection of finite point sources each emitting a certain and uniform amount of radiant energy. The radiance of the blackbody L, defined in Eq. 3 for a given bandwidth $\lambda_1 - \lambda_2$, is the power per unit source area per unit solid angle. The solid angle Ω is defined as

$$\Omega = \frac{A_d}{r^2}. \quad (48)$$

As seen in Figure 10, each of these points will emit the same amount of power onto an object with area A_d located a distance r away from the blackbody, as the solid angle for each of these points is identical. The total power on the object is thus the summation of all these point sources, which is

$$P = L \times A_{BB} \times \Omega \,. \quad (49)$$

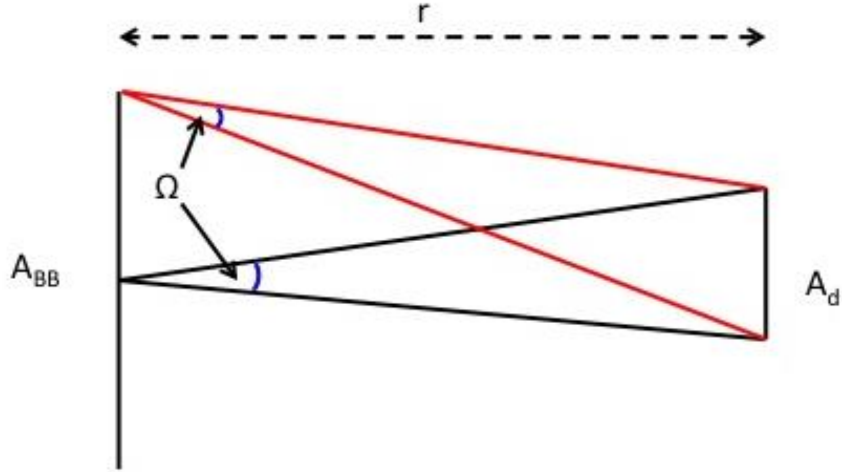

Figure 10. Schematic showing the solid angle Ω based upon a detector with area A_d a distance r away from a blackbody.

There will be a small amount of background energy based off of the ambient temperature, which will be different from the temperature of the blackbody. In essence, this is the temperature of the chopping wheel. As the signal voltage is actually the difference between the blocked and unblocked states of the chopper, the background radiance should be subtracted from the blackbody radiance, giving the differential radiance $\Delta L = L_{BB} - L_{Background}$. The incident power for a modulated signal is given by [24]

$$\Delta P_i(T) = \Delta L(T)\frac{A_{BB}A_d}{r^2}F_f t \tag{50}$$

where t is the transmittance of the KRS-5 window of the detector housing, and F_f is the incident power RMS form factor to account for the modulation of the signal, assuming the modulation produces a square wave with a 50% duty ($Ff = \frac{\sqrt{2}}{Pi}$).

The blackbody has an aperture area $A_{BB}=26.4\ cm^2$, and detectors have an area $A_d= 1.225 \times 10^{-5}\ cm^2$. The radiance is calculated between 0.6-40 μm, based off of the transmittance bandwidth for the KRS-5 window. A background temperature of 22˚C (295 K) has a radiance of 13.07 mW/cm^2 sr.

2.5.3 NEP and D*

Important figures of merit for an infrared detector are Noise Equivalent Power (NEP) and Normalized Detectivity (D*). These figures of merit exist to help characterize infrared detectors and to compare detectors of different geometries and configurations. NEP is defined as [24]

$$NEP = \frac{\Delta P_i}{SNR} = \frac{V_N}{\mathcal{R}_v}. \quad (51)$$

In general, NEP is the minimum amount of radiation discernable, that is, in which the signal-to-noise ratio is 1. NEP depends upon many parameters of the detector, such as area, bias voltage, spectral range, chopping frequency and noise equivalent bandwidth Δf. The last of these factors, Δf, is of great importance. Consider the lock-in amplifier used to measure a signal voltage. This device functions by isolating a signal at a particular frequency. According to Fourier's theorem, any random periodic signal can be expressed as a series of sine waves of various frequencies. A signal voltage as a function of time can be observed in in a frequency domain using a Fourier transform. The range of frequencies that are observed for a given signal are hence related to the integration time over which the signal is being observed. A small integration time will mean a large frequency bandwidth;

however in theory an infinite integration time would result in a delta function in the frequency domain. This relationship has already been given in Eq. 31. As the noise spectrum is largely flat over the frequency domain, the measured noise will be reduced as Δf gets smaller. One could therefore report a very low NEP by integrating over a long time on a lock in amplifier.

To normalize NEP for detector area and noise equivalent bandwidth, the normalized detectivity has been defined as [24]

$$D^* = \frac{\sqrt{A_d}\sqrt{\Delta f}}{NEP} \tag{52}$$

which has units of cm $Hz^{1/2}$ W^{-1}, sometimes referred to as *Jones*. Unlike NEP, high D* is desirable. Microbolometers generally have a D* of ~10^8 cm $Hz^{-1/2}$ W^{-1} for LWIR.

2.5.4 NETD

The Noise Equivalent Temperature Difference (NETD, or NEΔT) is the minimum temperature difference that an imaging system can observe. In other terms, it is the temperature difference that would result in a SNR of 1. NETD has already been defined in Eq. 1 for an imager. However, NETD can be calculated for a single pixel with a given D*, assuming some parameters of the imaging system.

An imaging system will consist of a detector, a lens, and an amplifier. The lens helps to focus a distant image onto the detector, in essence increasing the total incident power. The

amplifier is generally necessary as ΔL from distant objects at temperatures close to ambient is small. The amplifier will increase the input voltage; this includes both signal voltage and noise voltage, so that the SNR, NEP and D* will remain constant (in practice, there is usually noise associated with an amplifier, so if anything, SNR can go down with the addition of an amplifier; low noise amplifiers have been developed to reduce the effect of this additional noise source).

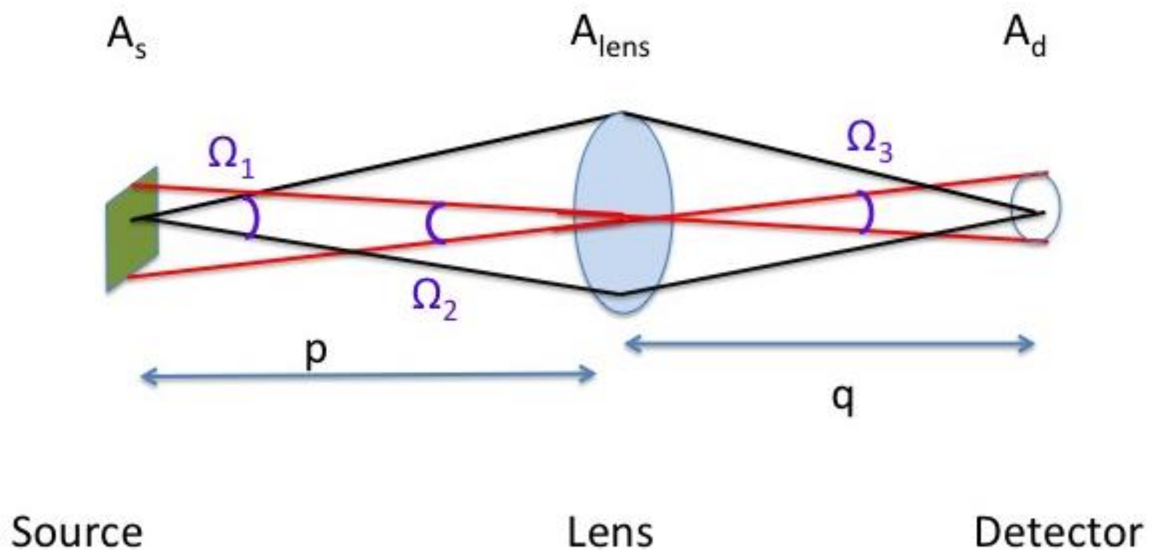

Figure 11. Ray diagram schematic in which a lens is used with a detector to image a source.

A ray diagram schematic for a source-lens-detector system is shown in Figure 11. The three solid angles drawn in the image are expressed as

$$\Omega_1 = \frac{A_{lens}}{p^2}\ , \Omega_2 = \frac{A_s}{p^2}\ , \Omega = \frac{A_d}{q^2}\ \ . \tag{53}$$

A_s stands for that portion of an extended source (the scene) that is imaged onto the detector area A_d. Rays from the extreme edges of A_s pass undeflected through the center of the lens to the extremes of A_d. These rays are indicated by red lines Figure 11, which shows that $\Omega_2 = \Omega_3$. The incident power is thus

$$P = L \times A_s \times \Omega_1 = L \times A_{lens} \times \Omega_2 = L \times A_{lens} \times \Omega_3 \,, \tag{54}$$

where the second equality holds by the definition of solid angle (Eq. 48). For distant objects $p \rightarrow \infty$ and q~F, the focal length of the lens, and the power can be expressed as

$$P = L \times A_{lens} \times \frac{A_d}{F^2} = L \times \pi \left(\frac{D_{lens}}{2}\right)^2 \times \frac{A_d}{F^2}. \tag{55}$$

The F-number of the optical system is defined as

$$F/\# = \frac{F}{D_{lens}}, \tag{56}$$

so that the incident power can finally be written as [24]

$$P = L \times \frac{\pi}{4} \times \frac{A_d}{(F/\#)^2} \,. \tag{57}$$

Eq. 57 can be defined in terms as signal voltage based upon the device responsivity. Seeking a thermal gradient, $\frac{\partial}{\partial T}$ is taken of both sides, which yields

$$\frac{dV_{out}}{\Delta T} = \mathcal{R}_V \times \frac{\partial L}{\partial T} \times \frac{\pi}{4} \times \frac{A_d}{(F/\#)^2}. \tag{58}$$

Eq. 51 gives $\mathcal{R}_v = \frac{V_N}{NEP}$, and $\frac{dV_{out}}{V_N} = SNR$ by definition. From this, the NETD can be written in terms of NEP as

$$\frac{\Delta T}{SNR} = NETD = \frac{4}{\pi}\left[\frac{(F/\#)^2 NEP}{\frac{\partial L}{\partial T} A_d}\right], \tag{59}$$

or in terms of D*,

$$NETD = \frac{4}{\pi}\left[\frac{(F/\#)^2\sqrt{\Delta f}}{D^*\left(\frac{\partial L}{\partial T}\right)\sqrt{A_d}}\right] . \tag{60}$$

The term $\frac{\partial L}{\partial T}$ in Eq. 60 is the *radiance contrast*. *L* changes with *T* according to

$$\frac{\partial L}{\partial T} = +\frac{2k^4T^3}{h^3c^2}\int_{x_2}^{x_1}\frac{e^x x^4}{(e^x-1)^2}dx , \tag{61}$$

Where $x = \frac{hc}{\lambda kT}$. At 300K, $\frac{\partial L}{\partial T} = 0.629\frac{W}{m^2\ sr\ K}$ for LWIR.

Hence, by determining the D* of individual fabricated devices, the NETD of a potential imager can be determined. Efforts to improve an imager must start at maximizing D*.

CHAPTER THREE: MICROBOLOMETER DEVELOPMENT

3.1 Microbolometer Design and Performance Estimations

The microbolometer under investigation in this work was designed by Plasmonics, Inc. for use in a linear array detector system [20]. Individual detectors (often referred to as *pixels* in an imaging system, as a single detector will generally correspond to one single pixel in a visual display) can be characterized by the pixel *fill factor*, which is the ratio of the active area to the total area. High fill factor is desirable to maximize the efficiency of incident energy. In a standard infrared imager, detectors are laid out in a two-dimensional grid, called a focal plane array (FPA), and so a two-dimensional fill factor is considered. With a linear array, the fill factor is only considered in one dimension. This influences the geometry of the support arms and increases the potential for thermal isolation.

Detector design is shown in Figure 12, showing the detector built upon the sacrificial polyimide layer (A) and then freestanding after this layer has been removed (B). The structure is built on an oxidized silicon wafer for electrical isolation. Gold reflectors are patterned where the elements will eventually sit. The air bridge structure is achieved by first depositing a sacrificial polyimide and using a wet etch process to form it into pillars of the desired thickness and lateral dimension. The thickness of this layer will be the size of the quarter-wave cavity. Structural considerations with the support arms favor shallow-sloped sidewalls, which are designed to be ~45˚.

Now the element is patterned on the polyimide. Because the active film VO_x-Au etches quickly in any plasma, the film is encapsulated in between two layers of silicon dioxide. Low-stress NiCr (80/20 nickel/chrome) arms are sputtered to form the arms of the air bridge. These arms provide structural stability and electrical continuity. They stretch over the polyimide pillar, so that the slope of the polyimide sidewalls corresponds to the slope of these arms (A).

The final step in the process is the removal of the cured polyimide to create a freestanding air bridge with two NiCr anchors (B). The sample is placed in an isotropic O_2 plasma in a barrel asher and etched until the polyimide is removed.

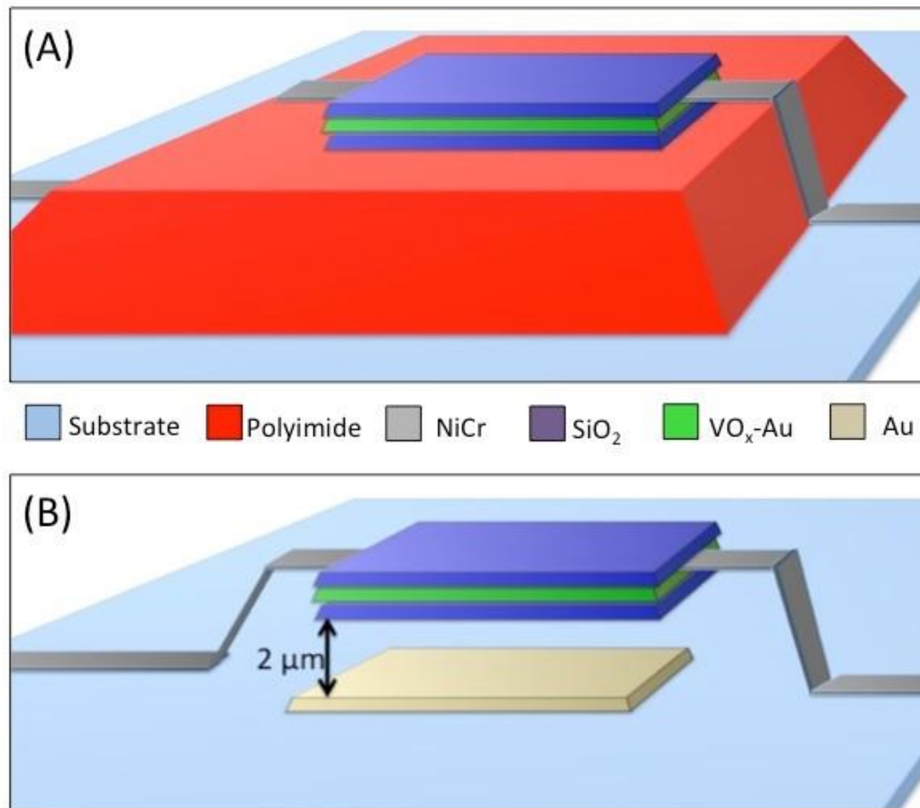

Figure 12. Drawing of the detector design before (A) and after (B) removal of the sacrificial polyimide.

The active area A_d is the VO_x-Au film, which has an area of 35 x 35 µm^2 and is 120 nm thick. The SiO_2 layers are 350 nm each, and have an area of 40 x 40 µm to facilitate full encapsulation of the VO_x-Au. The NiCr arms are 4 µm wide and have a total length of 10 µm to the substrate. The arms are designed to be 200 nm thick. The heat capacity and device thermal conductance through the arms and by radiation can be evaluated using Eqs. 42, 43, and 7 and material properties found in Table 1. The calculated heat capacity is 1.87 x 10^{-9} J/K, the thermal conductance through the arms is 1.8 x 10^{-6} W/K, and the thermal conductance by radiation is 7.5 x 10^{-9} W/K, which is small enough to be considered

negligible by these calculations. The thermal time constant, given from Eq. 27, is 1.035 ms.

Table 1. Physical and thermal properties of materials used in device fabrication

	Specific Heat [J g^{-1} K^{-1}]	Density [x 10^6 g m^{-3}]	Thermal Conductivity [W m^{-1} K^{-1}]
VO_2 [12]	0.3	3.36	Temperature dependent
Au [57]	0.129	19.8	314
SiO_2 [37]	0.7	2.2	1.1
NiCr [58]	0.45	8.4	11.3

Physical and thermal properties for the VO_x-Au film are not known. The parameters in Table 1 are reported for crystalline VO_2, which neglects the non-stoichiometric composition of VO_x and the additional degrees of freedom of amorphous over crystalline films. Furthermore, the heat capacity of crystalline VO_2 changes with a phase transformation, while the VO_x films do not undergo any reversible phase transformation [32]. Furthermore, the dispersed Au nanoparticles add more complexity to determining these parameters. Therefore it can be reasonably assumed that the density and specific heat are higher in VO_x-Au than in crystalline VO_2, and so the calculated heat capacity should be considered an underestimation.

The average absorptance for LWIR for a quarter wave cavity of 2 μm was shown in Figure 8 to be 71%.

For an incident power of 100nW, the temperature of the device will rise by $\Delta T = 38.5\ mK$, by Eq. 26. From the definition of TCR (Eq. 9), the change in device resistance is $\Delta R \approx$

$R_0 \alpha \Delta T$. Measurements of VO_x-Au films have shown a sheet resistance of ~250 kΩ with a TCR of -2.0 %. The resistance of the VO_x film, with 100 nW of power, will decrease by 192.7 Ω. With 1V applied bias, the estimated responsivity by Eq. 29 is 1927 V/W.

Noise calculations from Eqs. 30, 37, 38 and 39, show that the detector is Johnson noise limited. From these calculations, Johnson noise is expected to be 352.5 nV, while thermal fluctuation, background fluctuation and 1/f noise contribute 44.6 nV, 2.4 nV, and 82.5 nV, respectively, giving a total expected noise voltage of 364.8 nV.

From Eq. 51, $NEP = \frac{V_N}{\mathcal{R}_v} = \frac{364.8\ nV}{1927\ V/W} = 1.9 \times 10^{-10}\ W$. From Eq. 52, D*=1.01 x 10^8 cm √Hz W^{-1}. Finally, for an imager using F/1 optics and operating at 30 Hz video frame rate, expected NETD by Eq. 60 is 312.7 mK.

3.2 VO_x-Au Development and Optimization

3.2.1 Background

VO_x can be deposited by evaporating thin films of vanadium then annealing in an oxygen environment [59, 60], by reactive sputtering [35], and by sol-gel method [61]. The first method involves depositing pure vanadium by sputtering or evaporation onto a substrate. A subsequent anneal at high temperatures in an oxygen environment will cause oxygen atoms to diffuse into the vanadium film. In reactive sputtering, pure vanadium is sputtered in an argon/oxygen plasma. Vanadium atoms knocked off of the target will combine with oxygen atoms en route to the substrate, and thus can be deposited on the substrate as VO_x.

The partial pressure of oxygen has a large effect on this process. A sol-gel deposition involves a chemical process by which VO_x powder is dissolved or suspended in a solvent solution. This solution can then be spin-coated onto a substrate, and the solvent can be baked off. Annealing steps are often employed to optimize film quality.

Jin et al. have explored the factors that affect VO_x deposition by DC magnetron reactive sputtering [35]. They identified chamber pressure, oxygen content, throw distance and oxygen inlet position as factors that can affect the TCR and resistivity of a VO_x film. The deposition rate is affected by these elements as well, and it may be concluded that the deposition rate is an indicator of the film quality.

Figure 13 presents data from [35] showing the relationship of O_2/Ar ratio and chamber pressure on TCR and resistivity. When the oxygen content in the chamber is low, the metal sputtered from the target will largely remain metallic as it comes in contact with the substrate. Only a small amount of vanadium will be oxidized, and the value of x in VO_x will be small. In other words, if the oxygen content is small, then there is not enough oxygen to quench all of the vanadium atoms.

At the other extreme, if the oxygen content is too large, then not only will a higher ratio of vanadium atoms be oxidized en route to the substrate, but the excess oxygen will begin to oxidize the surface of the target. This effect is called *target poisoning*. Instead of sputtering pure vanadium, VO_x will be sputtered. DC magnetron sputtering relies on using the target at a cathode and an electrical potential being generated at the surface. Thus, metals will sputter much more quickly than dielectrics. If a metal target has surface

poisoning, the deposition rate will drastically drop. The high oxygen content and target poisoning create a positive feedback loop that keeps the target surface oxidized and the value of x in the VO_x film quite high. The effects of target poisoning can be seen in Figure 13 for high oxygen content. At an O_2/Ar ratio of 0.12, the deposition rate drops and the resistivity increases, sometimes by many orders of magnitude. This effect is enhanced at higher chamber pressures; hence keeping the chamber pressure low may be useful in maintaining a more uniform and repeatable recipe. As noted in the plots, the TCR is higher for films with higher resistivity.

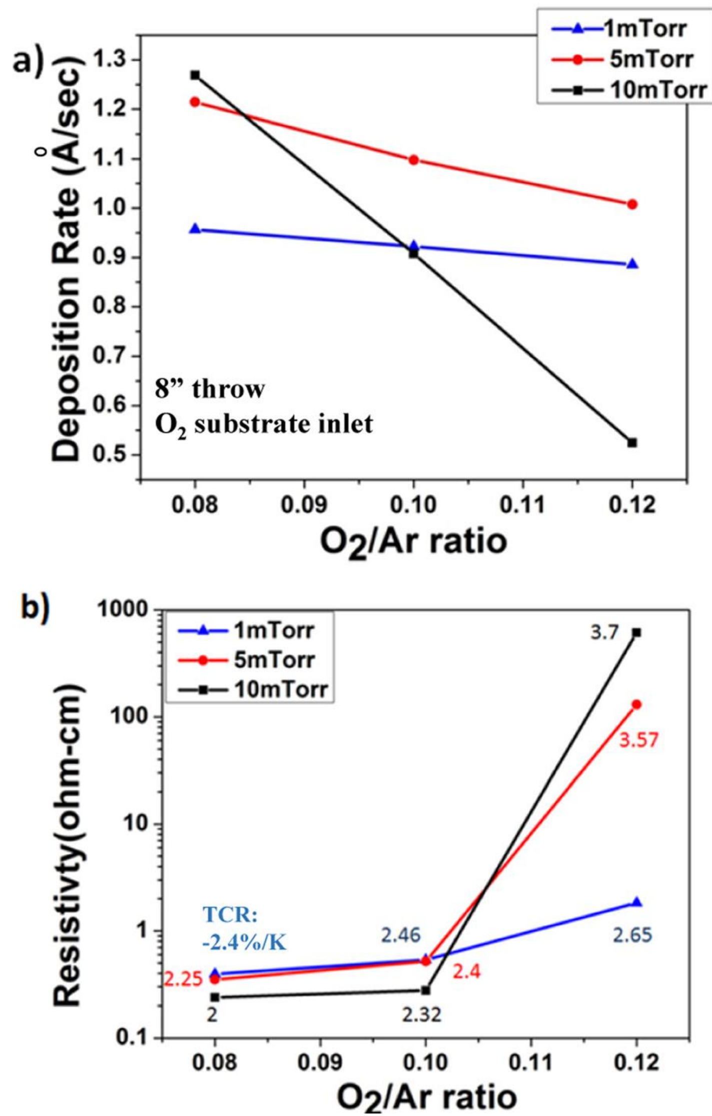

Figure 13. Deposition rate, TCR and resistivity of VOx films as a function of oxygen/argon ratio. Films were deposited by reactive pulsed-dc magnetron sputtering by Jin et al. [35]. Reprinted with permission from Jin, Y.O., et al., Potential for reactive pulsed-dc magnetron sputtering of nanocomposite VOx microbolometer thin films. Journal of Vacuum Science & Technology A, 2014. ***32****(6): p. 061501, Copyright 2014, American Vacuum Society.*

The VOx films doped with metallic particles investigated in this work were developed by Lam [62, 63]. Films were deposited by reactive DC magnetron co-sputtering of noble

metals with vanadium in an Argon/Oxygen plasma. Films were made with platinum and gold dopant materials; the relative sputtering power of the respective targets controlled the concentration of metal to VOx. Platinum proved to be more difficult to control, as it more greatly affected the TCR of the film. On the other hand, it was shown that a small amount of gold infused into the VOx film would drop the resistivity of the film without decreasing the TCR. Increasing the amount of gold would eventually result in a drop in TCR, along with a continued drop in resistivity.

3.2.2 Experimental Methods

VO_x-Au films were deposited in a 6-gun AJA sputter coater with RF and DC magnetron power supply capabilities. The system has a load lock to facilitate multiple depositions at uniformly low pressure in a small amount of time. Up to four gasses can be flowed into the chamber with flow rates of 1-20 standard cubic centimeters per minute (sccm) with a precision of 0.1 sccm. Chamber pressure is maintained with a throttle value to within 0.1 mTorr. Substrates are offset a distance of ~8 inches from the targets and rotated during deposition to ensure uniformity. The substrate could also be RF biased, which increases the surface energy of the substrate and can increase the density of deposited films. A residual gas analyzer (RGA) is attached to the machine that allows for *in situ* monitoring of chamber gas composition, before, during, and after a deposition.

The following parameters were modulated in the optimization of VO_x films: (1) Number of vanadium targets and power; (2) gold target power; (3) oxygen-to-argon ratio; (4) chamber pressure; and (5) substrate RF bias voltage. While not directly an experimental parameter, it was also observed that chamber contamination and base pressure also had an effect on the quality and reproducibility of VO_x films. By directly changing these parameters, the relative composition of vanadium, oxygen and gold are changed in the film, resulting in more dielectric or more metallic films, which in turn relate back to the TCR and resistivity of the film.

The Au to VO_x ratio was directly modulated by keeping the bias power constant for the vanadium target and altering the bias power on the gold target. The total amount of Au in the film (%Au) is found from the ratio of the number of Au atoms to the total number of atoms in the film, where the number of atoms is

$$\# \, Atoms = \frac{Density \times Deposition \, Rate}{Atomic \, Mass}, \qquad (62)$$

which has units of moles per area times time. In essence, this describes the average number of atoms deposited in a single monolayer of material. Deposition rates were measured for VO_x and Au separately but in similar environments. For a 200W bias on a vanadium target in 2% O_2, the deposition rate of VO_x was ~60 Å/min per vanadium target, while the deposition rate for gold was found to be ~1 Å/min per Watt applied bias, which was determined to be accurate from ~3-10W applied bias. Although the deposition rate for VO_x is dependent upon the oxygen partial pressure, this deposition rate showed little

change *so long as the target did not become poisoned*, at which point the deposition rate would dramatically drop.

The oxygen content in the atmosphere, which influences the value of x, was manipulated by the flow rates of oxygen and argon process gasses. To fine-tune this ratio, a bottle of 20% O_2 to Ar was mixed with pure Ar, such that

$$\%O_2 = \frac{0.2\times O_2/Ar\ flow\ rate}{total\ gas\ flow\ rate}. \quad (63)$$

An RGA is a mass spectrometer built in to the vacuum chamber. Gas particles from the chamber are ionized and sent through a field, whereupon they are filtered out and separated by atomic mass. An RGA gives data in terms of counts (# of atoms) per atomic mass unit. For a nominal O_2 ratio of 20%, RGA analysis indicates only 12% oxygen environment in the chamber. When a plasma is ignited on one vanadium target, free oxygen particles combine with ejected vanadium particles, and this ratio drops to 8%. If the number of targets increases to four, then the oxygen ratio drops to 0.5%. Figure 14 presents RGA data during a deposition at 4mTorr in which the nominal oxygen ratio is 20%. The largest and most characteristic peaks represent Argon and Oxygen. Argon has a peak at 40 AMU and a secondary isotope at 36 AMU. The peak at 20 AMU can be explained by doubly ionized argon. Oxygen has a characteristic peak at 32 AMU. This plot also shows the presence of chamber contaminates. While much less present, water vapor is characterized at 16 and 18 AMU, while another contaminate, possibly explained by a carbon-chloride molecule, is indicated at 38 AMU.

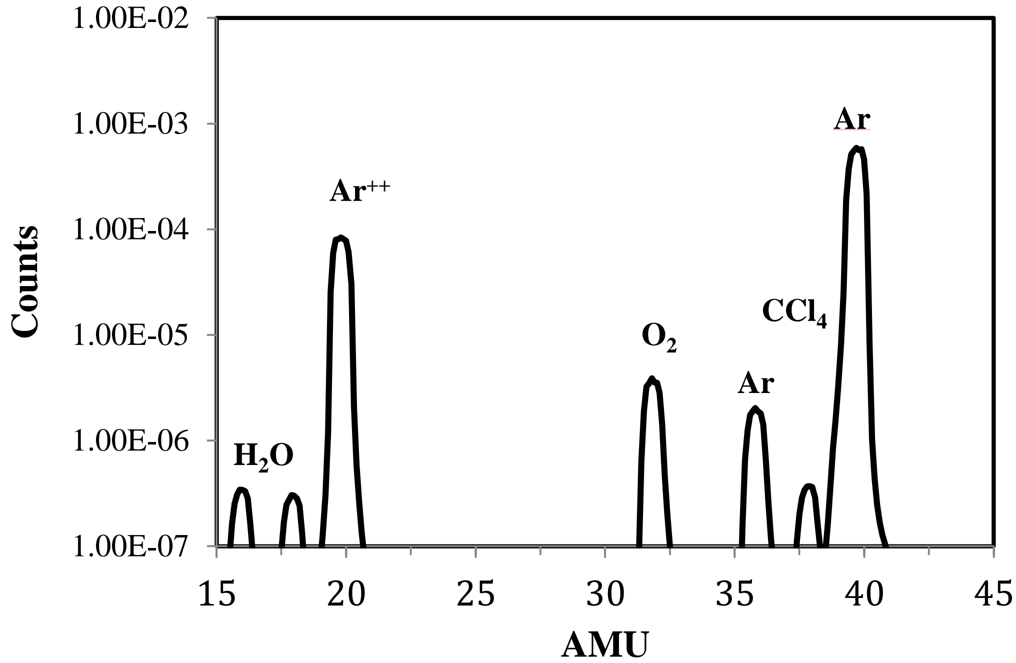

Figure 14. RGA data measured during a deposition The peak at 32 AMU is characteristic for O_2, while the peaks at 36 and 40 AMU show Argon.

For testing, VO_x-Au films were deposited on to oxidized silicon wafers. The thick surface oxide facilitates electrical isolation of the film. The resistivity of a VO_x-Au film is measured using a four-point probe method. A four-point probe has four pins equally spaced apart from each other, which are brought into contact with a thin film. A bias current is supplied by the outermost pins of the probe, while the potential is measured by the inner two pins. By the geometry of the system, the sheet resistance R_s is determined by

$$R_s = \frac{\pi}{\ln(2)} \frac{V}{I} \approx 4.53 \frac{V}{I}, \tag{64}$$

where sheet resistance is given in units of Ω/square. The product of the sheet resistance and the film thickness is the resistivity.

To determine the film thickness, a physical step is produced in the test film by a shadow mask during deposition; this can be as simple as a piece of tape or mark from a felt pen that can be removed in acetone post-deposition. The step can be measured using a stylus profilometer (Dektak 3). This consists of a fine-point pin that is connected to a sensitive piezoelectric crystal and then dragged across a surface to be measured. As the pin moves up and down across the topography of the surface, the piezoelectric crystal is stretched and compressed, which in turn releases a proportional electrical impulse. By dragging the stylus profilometer tip across a pre-defined step in the film, the thickness can be determined to within ~20 nm.

The TCR of a film is determined by measuring the sheet resistance of a film while it is heated on a hot plate. The definition of TCR from Eq. 9 can be written as $\alpha dT = \frac{dR}{R}$. Integrating both sides of this equation and solving for the TCR gives

$$\alpha = \frac{\Delta ln(R)}{\Delta T}. \quad (65)$$

Thus, TCR can be determined by plotting LN(R) as a function of T, and determining a linear fit of the data. A plot of Eq. 65 for a VO_x-Au film is shown in Figure 15. Deposition conditions were 12% Au, 3% O_2, 4mTorr chamber pressure, and with no substrate bias.

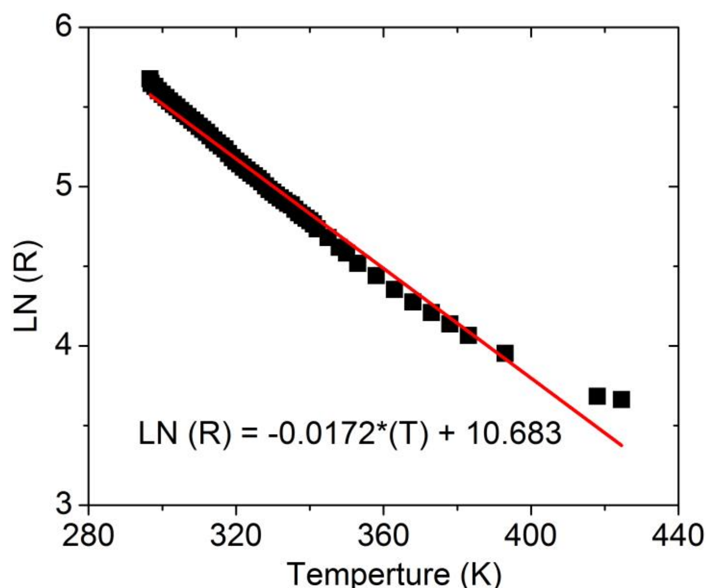

Figure 15. Plot of ln(R) vs. T a VO_x-Au film deposited with 3% O_2 and 12% Au.

3.2.3 Results

The influence of oxygen and gold ratios in deposition parameters on the room temperature resistivity of VO_x-Au is shown in Figure 16. These films were produced using a single vanadium target. Deposition parameters were randomized, instead of sequential, to reduce any tendency of systematic bias. Depositions were also completed over multiple days. The results indicate that a higher flow rate of oxygen compared with argon results in a generally more dielectric film with higher resistivity. For these VO_x films, the value of x increases with the amount of oxygen in the chamber. The trend with the gold content ratio is less clear, although films with more gold tend to have higher resistivity than films with less gold, as should be expected. The exception to this is the films produced using 12% Au,

which appeared to have the highest resistivity of all films at 1% O_2 and 2% O_2, while having a lower resistivity at 3% O_2. It should be noted that often depositions with the same parameters would have different results.

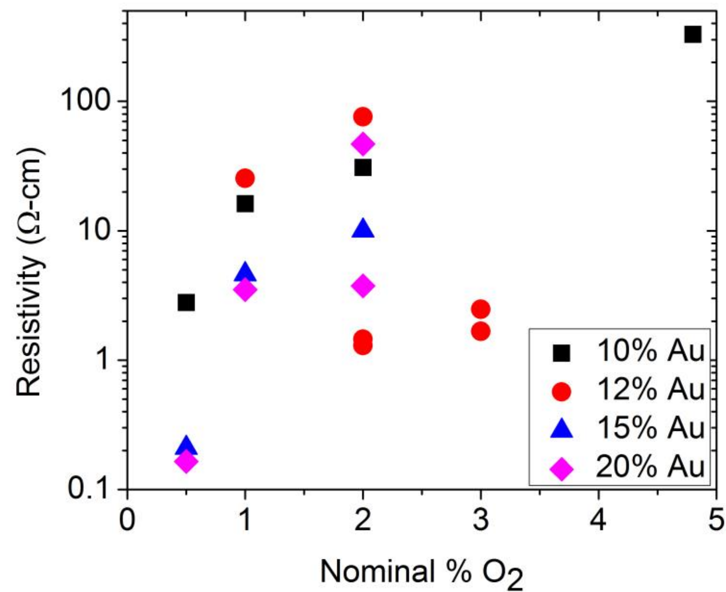

Figure 16. Relationship between % O_2, % Au and room temperature resistivity.

Figure 17 presents the effect of oxygen and gold ratios on TCR from the same samples as was shown in Figure 16. As the oxygen content increases, the films generally have a higher magnitude of TCR, which is to be expected from theory. As before, the exception to this is with the films produced using 12% Au, in which the trend is reversed or flat. Interestingly, a trend between gold content and TCR is not visible from this data. This suggests that a small amount of gold can influence the resistivity of film without negatively affecting the TCR.

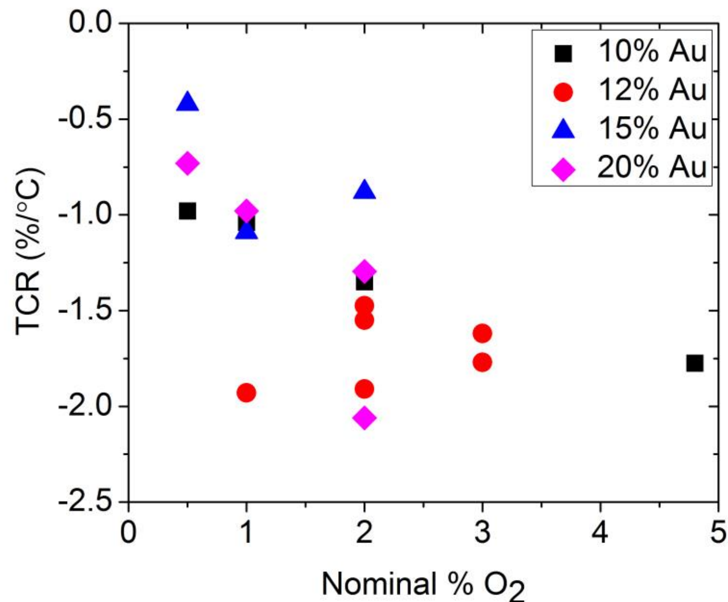

Figure 17. Relationship between % O_2, % Au and TCR.

While these data show general trends that agree with theory, they also demonstrate a great deal of inconsistency between runs, even for samples with the same parameters. Indeed, samples with the same measured resistivity will have different values for TCR, as noted in Figure 18. This indicates that other factors, such as the chamber base pressure, target and chamber conditioning, and chamber contaminants have a much larger effect on TCR and resistivity than initially expected. In addition, to achieve the desired parameters of low oxygen content and low gold content compared with sputtered vanadium, the flow rate of oxygen and power on the gold target had to be set to very low values, which may be near the limits of capabilities of the regulating mechanisms in the machine. To increase repeatability in detected devices, two schemes were identified: (1) increasing the deposition rate of vanadium and (2) monitoring the chamber base pressure and contamination levels. The former could be achieved by using co-sputtering with multiple

vanadium targets. For the latter, the machine was allowed to pump down for 48 hours prior to any deposition. RGA analysis showed a sizable presence of water vapor in the chamber, even at pressures of 10^{-6} Torr.

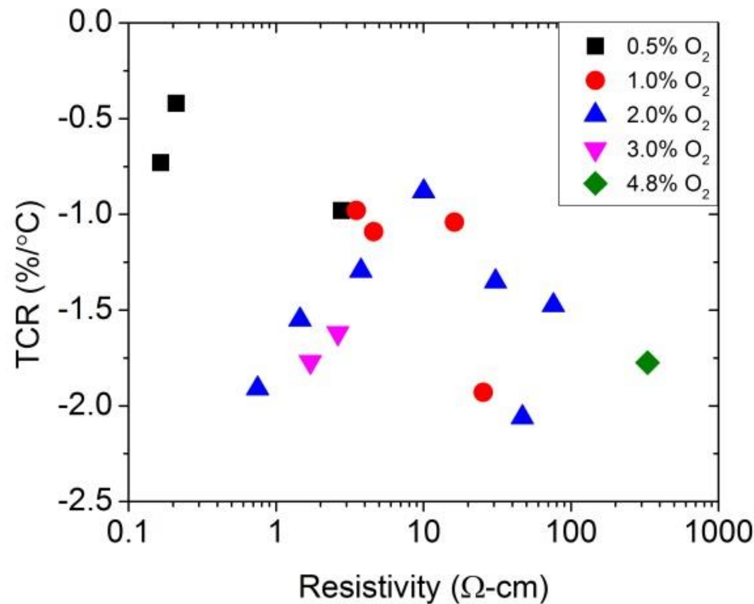

Figure 18. TCR and resistivity plot for samples using only one vanadium target. Samples are identified here by the nominal oxygen content.

Table 2 presents data for VO_x-Au deposited using 4 vanadium targets each powered at 200W and one gold target powered at 10 W in a nominal oxygen concentration of 20% and a chamber pressure of 4mTorr.

The nominal flow of oxygen in this case is much higher than when using only one vanadium target. This of course was the desired effect; a higher deposition rate of vanadium allows the flow rate of oxygen to be higher while keeping the effective oxygen content small. This was shown in RGA analysis from Figure 14. All samples were

deposited after the chamber was allowed to pump for 48 hours, and a base pressure less than 10^{-7} Torr was achieved. This base pressure was reproducible even for sequential depositions by using a load lock chamber. Films have an average resistivity of 2.66 Ω-cm with a standard deviation of 0.12 and an average TCR of -1.94% with a standard deviation of 0.0004.

Table 2. Resistivity and TCR values of VO_x-Au films produced with modified co-sputtering method. Samples 1 and 2 were purposely thicker films.

Sample	Thickness (nm)	Sheet Resistance at 22˚C (kΩ)	Resistivity at 22˚C (Ω-cm)	TCR (%/˚C)
1	350	71.9	2.51	-1.98%
2	140	198.8	2.78	-1.95%
3	110	201.6	2.49	-1.92%
4	110	257.8	2.84	-1.86%
5	110	248.7	2.74	-1.93%
6	110	242.8	2.67	-1.90%
7	110	245.1	2.7	-1.95%
8	110	240.1	2.64	-1.95%
9	110	233.8	2.57	-2.00%

Subsequent films using the same recipe were made on carbon substrates and analyzed using the Rutherford Backscattering technique to determine film composition. In this process, films are bombarded by high energy alpha particles. These particles lose energy simply by passing through a film, however a significant amount of energy is lost in a collision with an atom in the film. This energy is lost in the form of x-rays. By analyzing the spectrum of these x-rays information about the atomic composition of a sample can be determined. It is important to do this analysis on carbon substrates as the characteristic energies for

silicon overlap those of materials in the VO_x-Au films. The results of this testing determined the film composition of approximately 33.5% vanadium, 62.5% oxygen, and 4% gold by mole. The resulting molecular formula for the amorphous vanadium oxide was determined to be $VO_{1.87}$, with less than a 10% variation.

With a more repeatable process determined, an investigation into the process parameters to optimize the VO_x-Au film began. Table 3 presents the effect of substrate bias for a number of different deposition parameters. In most cases, substrate bias decreases the resistivity of the film while having little effect on the TCR of the film. Low resistivity was achieved for films deposited in a nominal 30% oxygen environment. In this case, the oxygen content was too high and the surface of the vanadium targets oxidized (target poisoning effect). The deposition rate of the VO_x greatly decreased, while the deposition rate of gold stayed constant as no oxidation occurs on the gold target. Therefore, the films are much more metal rich, and have a lower resistivity.

The predicted 1/f noise indicates that devices will likely be Johnson noise-limited for reasonable bias voltages if the resistance of the detector is at least 50 kΩ. Devices with low resistivity will therefore perform well in terms of Johnson noise, but this advantage will be lost because of 1/f noise. The ideal room temperature resistivity, therefore, is low but above 0.5 Ω-cm.

Table 3. Effect of substrate bias on TCR and resistivity for a number of different deposition parameters.

Deposition Parameters	Substrate Bias [W]	RT Resistivity [Ω-cm]	TCR [%/°C]
4 Vanadium targets, 20% O_2, 6.9% Au, 4mTorr	0	2.33	-1.99
	40	1.30	-2.00
4 Vanadium targets, 20% O_2, 12.8% Au, 4mTorr	0	0.32	-1.89
	40	0.39	-1.66
4 Vanadium targets, 30% O_2, 6.9% Au, 4mTorr	0	1.66	-1.89
	40	0.15	-1.19
4 Vanadium targets, 30% O_2, 12.8% Au, 4mTorr	0	0.11	-1.11
	40	0.18	-1.37
2 Vanadium targets, 20% O_2, 0% Au, 2mTorr	0	17.20	-2.79
	40	3.31	-2.24
2 Vanadium targets, 20% O_2, 0% Au, 4mTorr	0	39.10	-2.57
	40	4.93	-2.40
2 Vanadium targets, 20% O_2, 4% Au, 2mTorr	0	4.79	-2.22
	40	2.04	-2.32
2 Vanadium targets, 20% O_2, 6.8% Au, 2mTorr	0	1.95	-1.60
	40	1.37	-1.96

3.3 Optimization of Microbolometer Design

3.3.1 NiCr Arms

One obstacle in process development was the difficulty of depositing NiCr onto patterned photoresist. Often, a deposition by sputtering would result in films that had cracked or

flaked off of the sample. The breaking point would generally be along the sidewall of the polyimide pillar, although this was not exclusively the case. An SEM image showing broken and deflected NiCr arms after one such deposition is shown in Figure 19. Originally believed to be an overheating problem, many steps were taken to mitigate the issue, from use of thermal grease to testing different metals such as titanium and vanadium. These tests had mixed results, leading to the explanation that this was not a thermal problem. Thin films (~100nm) of vanadium and nichrome were sputter coated onto wafers covered in photoresist at various pressures, and the film stress was measured using a Flexus laser scan technique. It was determined that film stress was reduced at higher chamber pressure during the deposition, which allowed the deposition of thick films of NiCr without issue. Figure 20 shows a plot of film stress against chamber pressure for NiCr.

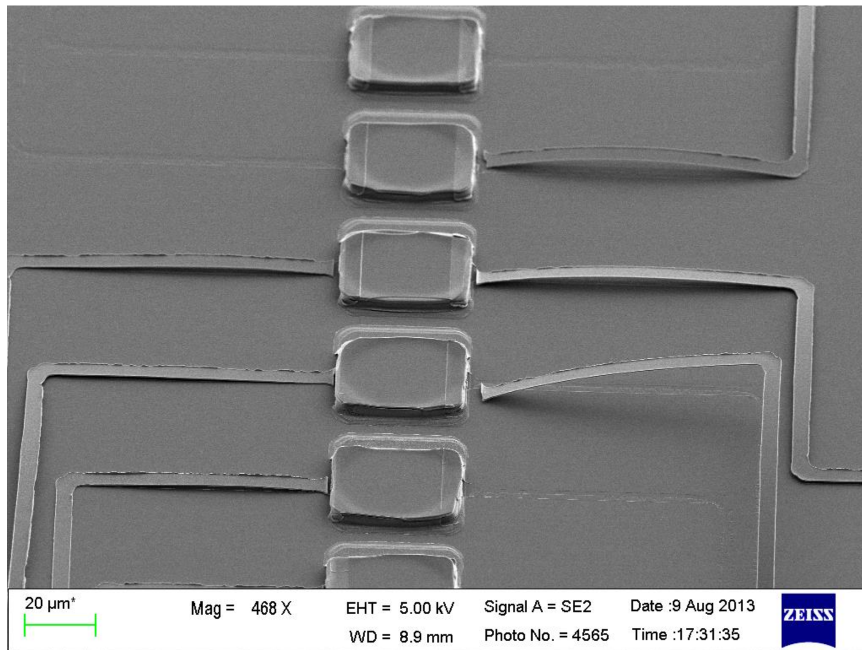

Figure 19. Film stress causing breaking and bending of deposited NiCr. The breaking point is generally at the polyimide sidewall. In this image, the polyimide was designed to be squares directly underneath the pixel.

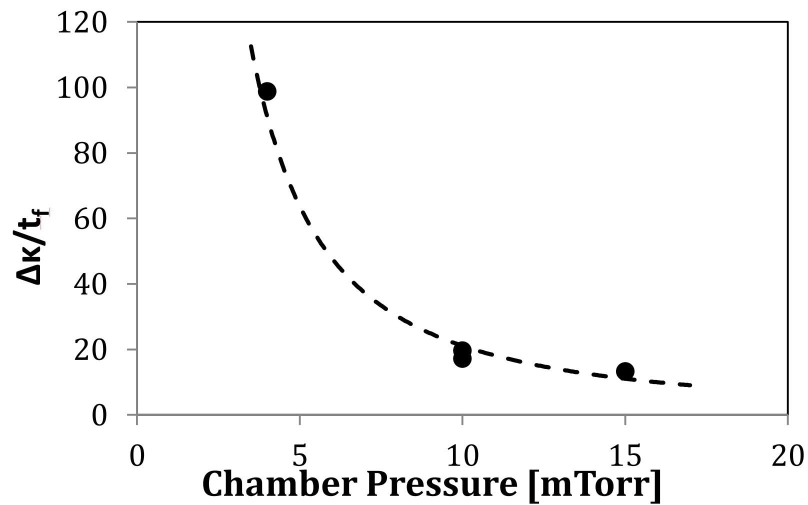

Figure 20. Film stress as a function of chamber pressure during sputter coating of NiCr.

3.3.2 Polyimide Sidewalls

The success of the microbolometer development hinged on the quality of the sidewalls on the polyimide pillars. The original design called for polyimide pillars to have 45˚ sidewalls upon which the NiCr arms could gently slope down to the substrate. Polyimide was deposited on the wafer by spin coating, and selectively etched away to form the desired structure. This patterning would also determine the length of the NiCr arms, which heavily influences the thermal conductance of the device.

A wet etch technique was used to etch the polyimide using photoresist developer. After the polyimide was spun on a wafer, photoresist was deposited and the desired pattern exposed. In a TMAH-based developer (tetramethyl ammonium hydroxide), the unexposed positive resist acted as an etch mask for the underlying polyimide. The wet etch technique was capable of leaving ~70˚ sidewalls, which was deemed sufficient for successful patterning of the NiCr arms. Unfortunately, this process was unpredictable. Often the sidewalls would be close to vertical or even have some slight undercut. To solve this problem, a secondary isotropic O_2/CF_4 plasma etch in a barrel asher was added to round the corners of the sidewalls. In this process, the polyimide is purposefully patterned 50% larger and thicker than intended, and the plasma etch is timed to remove the excess material. The plasma etches corners much more rapidly than flat regions, as the exposed surface area is larger; the end result is a rounded edge. Figure 21 presents an SEM image of these sidewalls before and after this plasma etch. Initially, the sidewall has a very still slope, which is smoothed out after the etch. Additionally, the top surface appears to have an extra,

“hardened” layer before the plasma etch. It is believed that this layer contains oxidized material, which is the reason for adding CF_4 to the plasma composition. Even still, this layer proved to have different and unpredictable etch rates than the rest of the polyimide, so that while this method was proved to be a success for some samples, it was still sufficiently unpredictable to keep yield of fabricated devices below 20%.

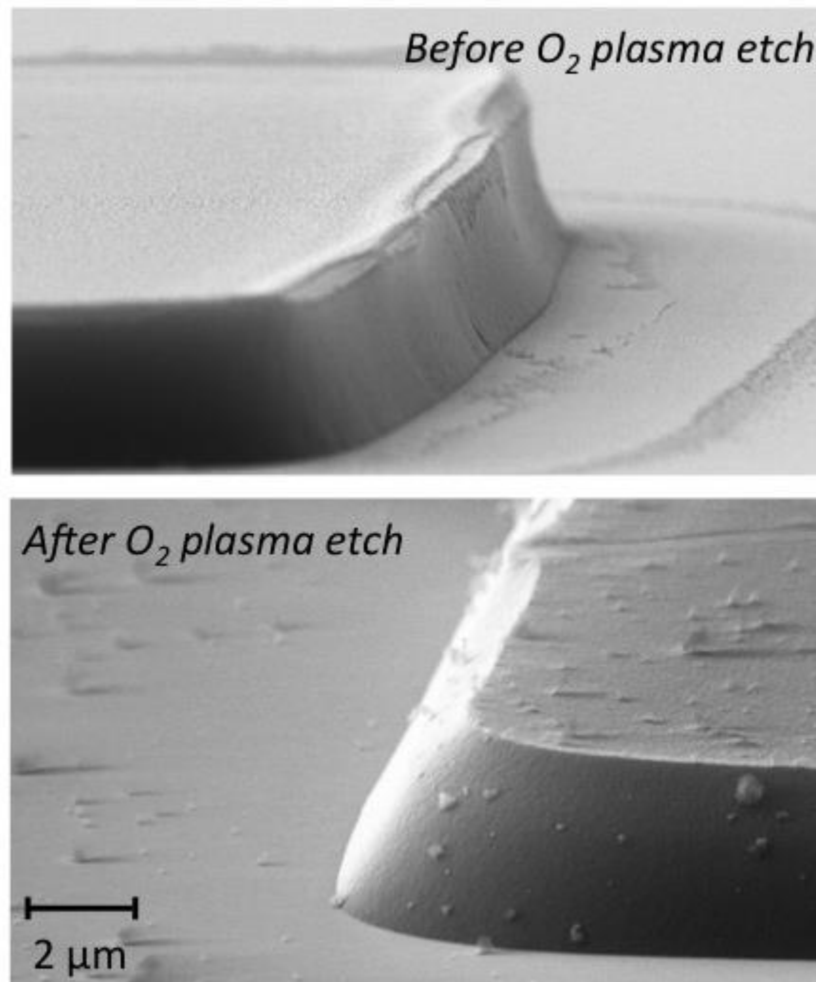

Figure 21. Polyimide sidewalls before and after an isotropic plasma etch. This process is designed to increase the slope of the sidewall.

3.3.3 Release Methods and Design Failures

Both wet and dry etch methods were investigated to remove the sacrificial polyimide layer and create the free-standing air bridge method. The wet etch methods involved submerging the sample in diluted Potassium Hydroxide (KOH). While this method was quick, it often caused failure due to surface tension pulling samples down to the substrate during drying.

A critical point dryer is often used in fabrication to solve this exact problem, but this approach often seemed to be too aggressive for high yield.

The more successful approach in the release etch was the use of the barrel asher. In this process, a plasma is created using an RF bias, but no DC supply is present, so that the plasma does not have any directional preference. This process is much slower than a more directional dry etch, such as in Reactive Ion Etching (RIE), in which plasma particles are accelerated towards the sample. In a barrel etcher, the etch is simply due to chemical reactions at any surface. During this process, the chamber reached temperatures of ~100˚C. The power was set at 400W, and the oxygen flow rate was set to achieve 650 mTorr pressure (usually around 200 sccm, but this could vary process to process). Samples were etched in 15-20 minute increments in an effort to reduce heating effects. After each increment, samples were imaged to determine if all of the polyimide had been removed. Figure 22 presents microscope images showing the progression of polyimide etching on a particular detector. After 45 minutes, the polyimide around the pixel is starting to be removed, and just begins to show removal from underneath the pixel. At 75 minutes, the polyimide is gone from around the pixel, and the contact with the underside of the pixel can be outlined easily. After 2 hours of etching, only a small amount of polyimide remains, but appears to no longer be in contact with the pixel. The right-hand side of the pixel shows some deformation or wrinkling of the film, a result of stresses induced in deposition and thermal processing. These deformations were commonly observed in pixels, particularly around the edges. This reduces the quality of the Fabry-Perot cavity and gives rise to a non-uniform absorptance across the pixel.

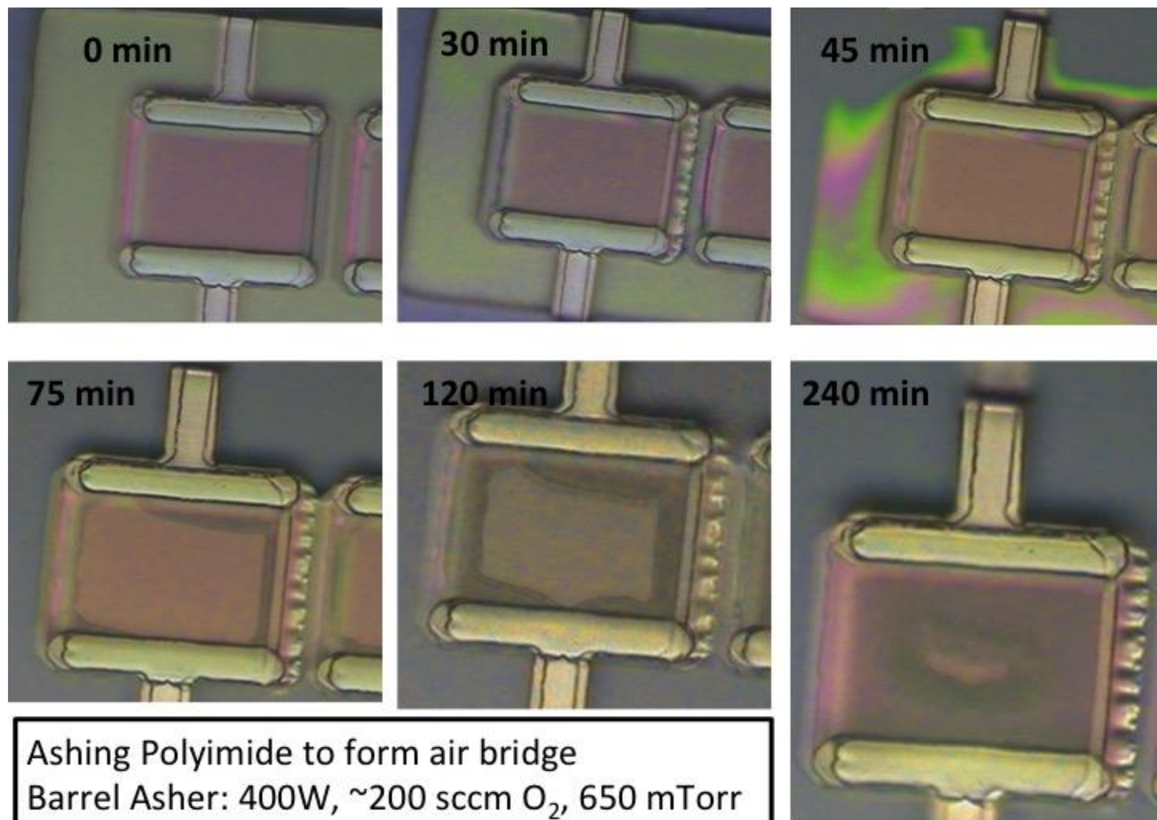

Figure 22. Microscope images showing the progression of the O_2 plasma release etch on single pixel. The polyimide seen around and under the pixel can be seen to be retreating over time.

The NiCr arms were connected to patterned gold bond pads on the substrate. Prior to any blackbody testing, these bond pads were probed and electrical continuity and resistance were determined for each detector. Failure of detectors came in two modes: detectors either measured as complete open circuits, or detectors measured with a high resistance (>1MΩ).

These two failures were identified to be occurring in two places: the first is in the bottom of the polyimide sidewall, where the NiCr arm starts to rise from the substrate surface to the top of the sacrificial layer. If there is any undercut or irregularity in the sidewall, then

the arm often have a break, as shown in Figure 23. This becomes more pronounced as sacrificial layer is removed and the arm weight applied to it. The second failure point was at the interface between the NiCr and the VO_x-Au film itself. This was due to poor contact due to “bat-ears”, or curled up portions of the film near the edges of the patterned area (see Figure 24). This effect is due to deposition on the sidewalls of the masking photoresist that is not removed cleanly during lift-off, and was solved by implementing a bi-layer resist process.

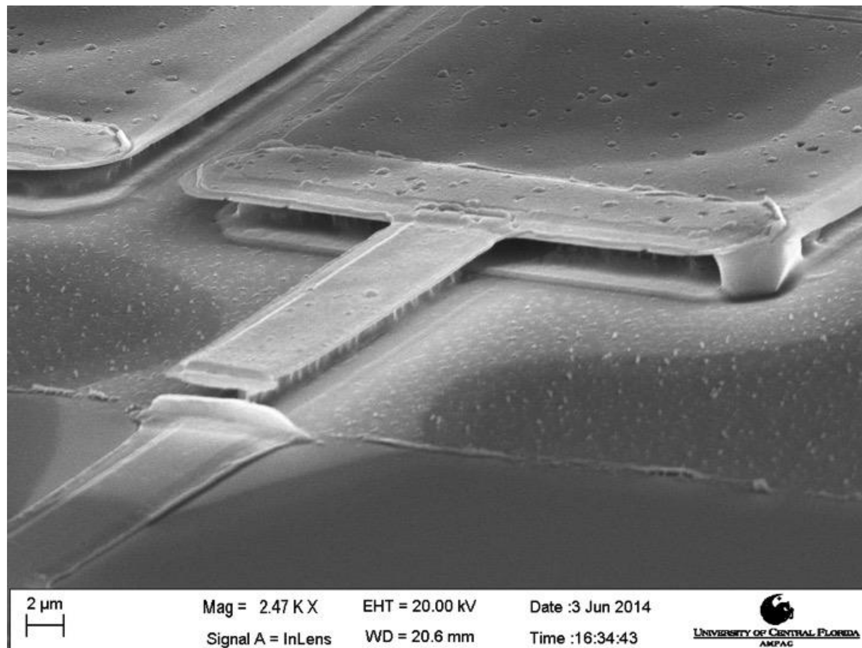

Figure 23. SEM image of a detector in which the NiCr arm has broken along the polyimide sidewall after release.

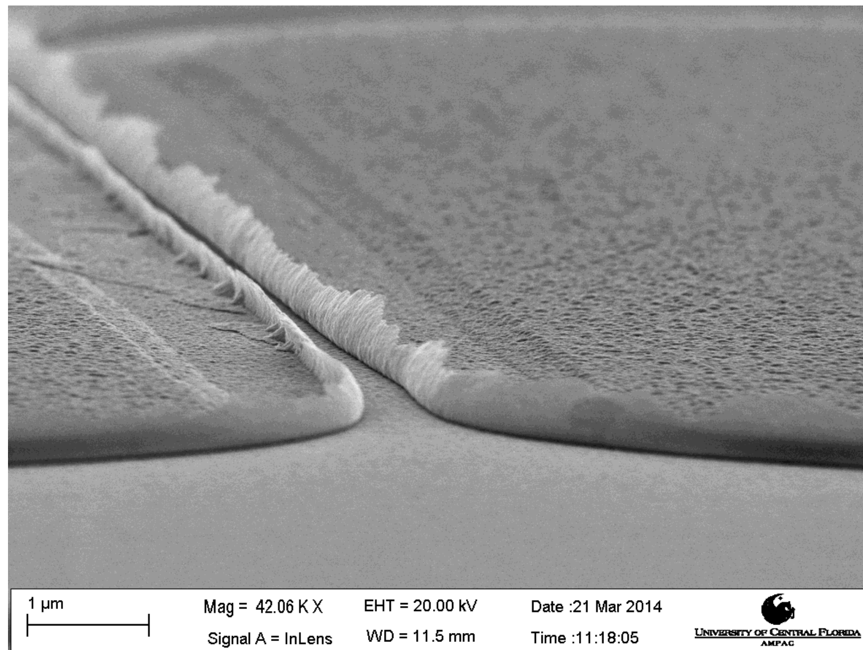

Figure 24. The edges of a sputtered VOx-Au film, showing the "bat-ear" effect that could cause electrical impedance issues.

3.3.4 Detector Redesign

The microbolometer fabrication process was redesigned to address the issues from the polyimide sidewalls. Even functioning devices in this initial design were incredibly fragile. This was due to the vertical or near vertical portion of the NiCr arm. Therefore, the detector was designed to keep the arms completely flat, even upon release. To do so, the detector was fabricated entirely flat on an SiO_2 surface, and the release etch involved cutting a trench into the silicon wafer underneath the pixel. In this redesign, detector arms were also lengthened to increase thermal conductance of the detector.

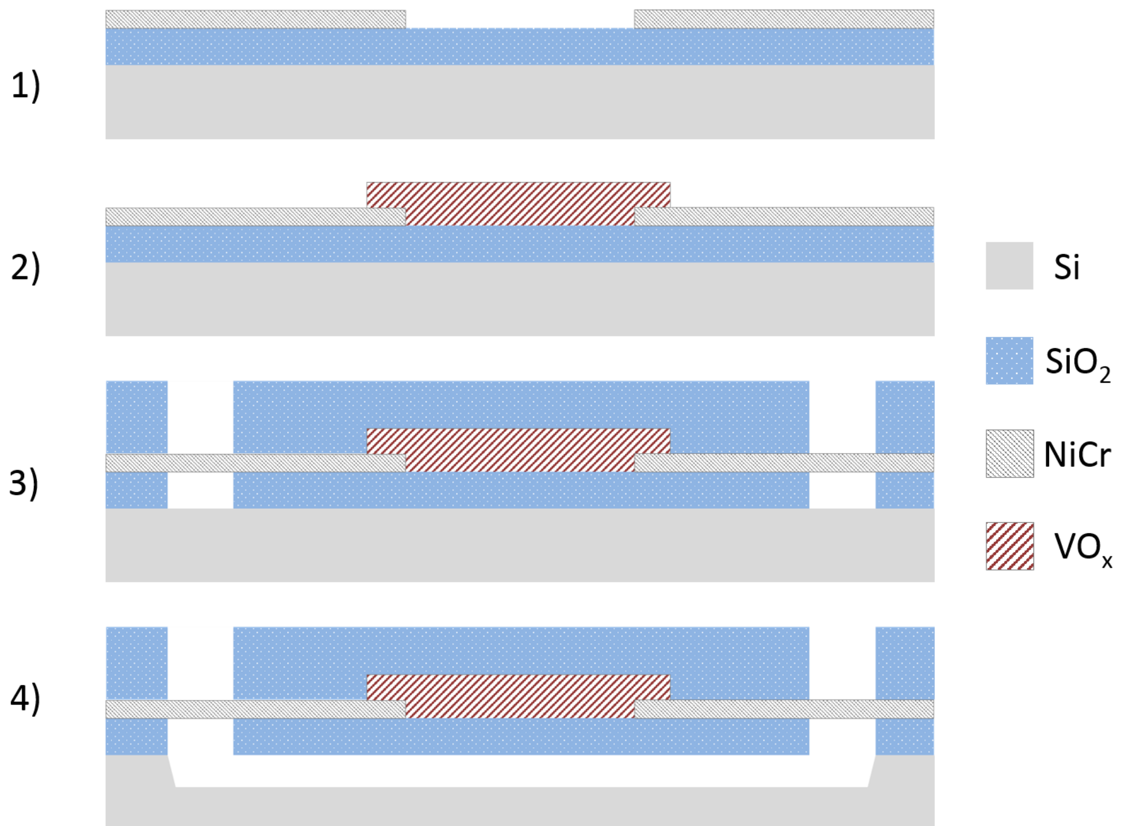

Figure 25. Process schematic for the redesign of the pixel, using a trench etch as opposed to the polyimide sacrificial layer.

Figure 25 presents a schematic of the fabrication steps. First, nickel-chrome alloy (nichrome, 80/20) is deposited and patterned on a thermally- oxidized silicon substrate to create the structural arms electrical interconnect for the detector. Next, VO_x film is co-sputtered with gold to form the active bolometer element. A layer of silicon oxide is then deposited by plasma-enhanced chemical vapor deposition (PECVD) over the surface to protect the VO_x-Au film, provide electrical isolation, and provide additional structural stability. The PECVD and thermal oxides are selectively co-etched to create vias to the silicon. Metal traces and bond pads are deposited and patterned by lift-off. Finally, the

detector elements were undercut by etching a trench in the silicon substrate using an isotropic fluorinated plasma in a barrel asher to form air bridges.

This process not only improved the production yield to over 95%, but detectors were much more mechanically stable upon release. Additionally, detectors in the second design seemed to measure with a lower and more uniform resistance than detectors using the first method, even though VO_x-Au witness samples had similar properties. There are two explanations for this effect, both of which may have contributed to the observation. First, the second design involved a PECVD oxide step, during which the sample is heated to 300˚C. This would inadvertently anneal the VOx-Au film. Gold grains have proven to grow as a result of annealing, and the density of the film would likely increase. Both of these effects would likely cause a drop in resistance, although the magnitude of this effect was never measured. Additionally, measured resistance variation in the first design could have been a result of poor ohmic contacts in the arms of the device, an effect that is solved in the redesign.

The downside of the redesigned microbolometer using the trench etch is the lack of control of the cavity dimensions. As the trench is etched using an isotropic plasma, a lateral etch of 17.5 μm (half the pixel dimension, the minimum necessary to release the pixel) would also etch 17.5 μm down, much greater than the desired 2-2.5 μm cavity designed originally for absorption. Indeed, fully released samples had very deep trenches. While the exact depth was never accurately measured, a metered changing in focus on an optical microscope between the base of the trench and the pixel indicated that this trench was over

10 μm deep. Furthermore, the trench is not flat, but slopes down to the bottom of the trench.

The fabrication plan was slightly altered in an attempt to achieve the desired cavity dimensions. First, a metal was deposited onto a bare silicon wafer by e-beam evaporation. This would act as the reflector for the absorbing cavity. Without breaking vacuum, amorphous silicon would be deposited on top of the metal, which served the role of the sacrificial material. Next, oxide would be deposited by PECVD, and the process would continue as before. Titanium, nickel and chromium were tested as the base metal for this process. The nickel failed due to adhesion problems with the evaporated amorphous silicon, and the titanium and chromium films failed to act as an adequate etch stop during the fluorinated oxide and release etches. This method should work given the right materials and process development, but this was never fully investigated.

Figure 26 shows SEM images of detectors fabricated using both designs. The sacrificial polyimide design produced functional devices and allowed for tight control over the cavity thickness, allowing for high absorption by this method. However, the weak arms made the device fragile and potentially hindered electrical continuity for the detector. This weakness also limited the total arm length possible, limiting the thermal conductance of the detector. The trench etch design is much more mechanically robust, involved fewer fabrication steps and facilitated clean, ohmic contacts across the detector. A stronger, more mechanically robust pixel allowed arm to be elongated to decrease thermal conductance. However, the

design removes practically all absorption gained by a Fabry-Perot quarter wave cavity. This created a need to investigate alternative absorption techniques.

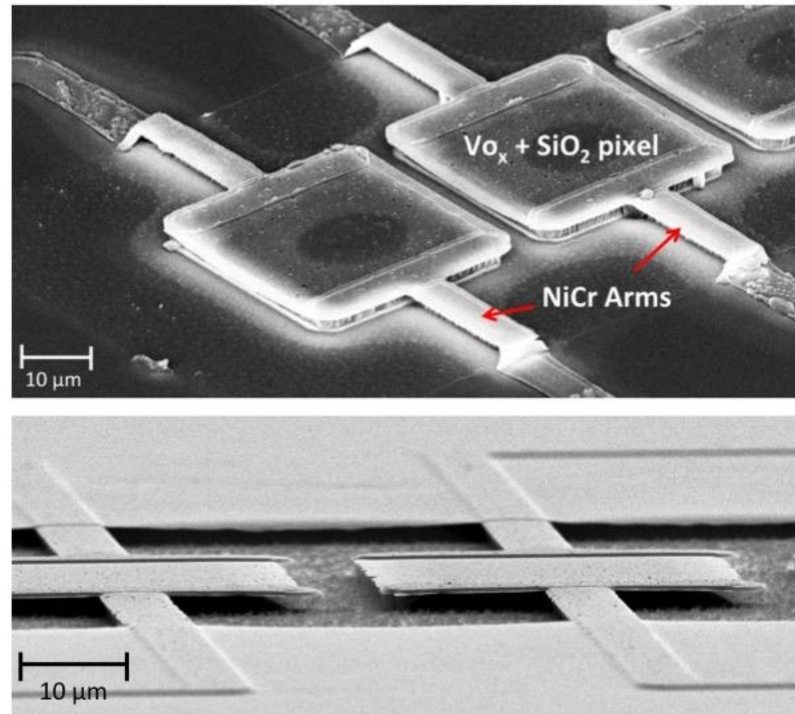

Figure 26. SEM images showing the two designs of microbolometers fabricated in this study: the top utilizes the sacrificial polyimide, while the bottom utilizes the flat pixel and silicon trench etch.

CHAPTER FOUR: SENSITIVITY ENHANCEMENTS USING PATTERNED GOLD BLACK ABSORBER

4.1 Experimental Methods

The use of metal black films and their advantages was discussed in Chapter 2. The aim of this investigation was to develop an absorptive coating that could work in tandem or even instead of the Fabry-Perot resonant cavity to achieve high responsivity in developed microbolometers. Gold black was chosen as an absorbing film due to its high absorptance over a very broad bandwidth [21, 49]. Gold black is a fragile film and as such is not suitable for integration with standard CMOS fabrication techniques. However, the ability to selectively pattern gold black by standard lift-off process using an oxide overcoat had recently been developed at UCF by Panjwani et al. [22], making this process readily available for integration with the designed microbolometers.

In this investigation, detectors were fabricated using the sacrificial polyimide layer design presented in Chapter 3. One single wafer containing hundreds of devices was fabricated and cleaved in half prior to deposition of gold black. Half of the detectors fabricated were kept uncoated for comparison. In this manner, the gold black coated samples and uncoated samples had entirely identical fabrication processes, excepting small uniformity variations. Gold black was deposited prior to the release etch, as observed fragility in the NiCr arms prevents any processing after samples are released.

Gold black was deposited and patterning were first described in [22]. Squares of dimension identical to the VO_x-Au film (35 x 35 μm^2) were patterned directly on top of the fabricated pixels using a negative tone resist, meaning that after development resist was removed only in this region above the pixel. The resist had a small amount of undercut to facilitate effective lift-off after deposition of the gold black.

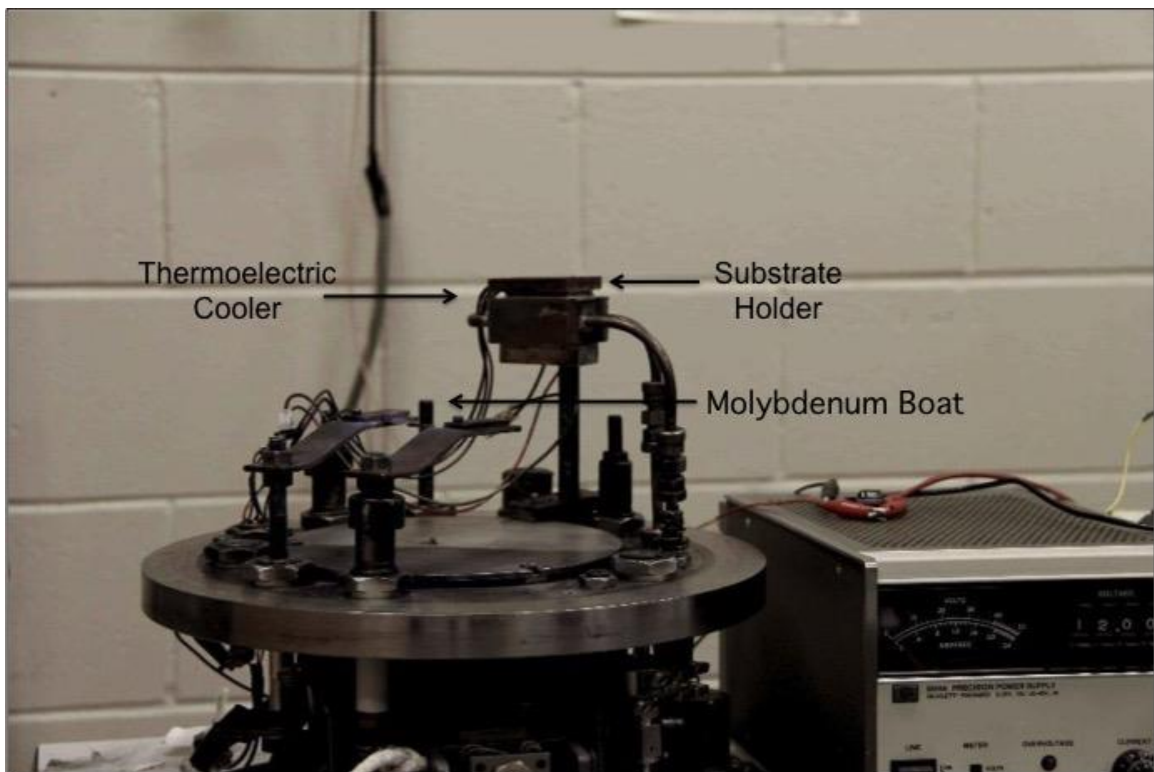

Figure 27. Deposition chamber for thermal evaporation of gold black (bell jar is removed). [49]

The deposition chamber used for thermal evaporation of gold black is shown in Figure 27. Gold source material was thermally evaporated at 300 mTorr N_2 ambient. The low mean free path inside the vacuum chamber causes gold atoms to collide and bind prior to landing on the thermoelectrically-cooled substrate (-13˚C) [64]. For sufficient uniformity and

thickness, multiple depositions were required with sample rotation between each deposition. The gold black was then encapsulated with 250 nm of e-beam evaporated SiO_2 prior to lift-off using n-methyl pyrrolidinone (NMP). After the deposition of gold black, samples were placed in the barrel asher for the isotropic O_2 plasma etch described in Chapter 3. As uncoated gold black does not even survive a puff of air directed at the film, it is worth noting that gold black in these detectors survives a solvent rinse, blow dry, and plasma treatment at temperatures up to 100˚C.

For characterization of absorptance, SiO_2-coated gold black films were deposited onto gold-coated silicon substrates. Specular and diffuse reflectance spectra were measured in a Hemispherical Directional Reflectance Spectrometer (SOC-100 HDR) connected to an Fourier Transform Infrared Spectrometer (FTIR, Thermo Scientific) using unpolarized light at incident angles of 7, 15, 30, 45, and 60°. Transmittance was zero due to the gold film on the substrate, so that absorptance is unity minus the measured reflectance.

Absorptance of individual bolometers was measured using the imaging spectrometer at the University of Wisconsin, Milwaukee (formerly at the Synchrotron Radiation Center)[65]. A Bruker Vertex FT-IR spectrometer equipped with a Hyperion 3000 infrared microscope was used to image the sample with a standard globar source. A 128 x 128 pixel focal plane array (FPA) detector was used to collect reflectance data over the 900-3700 cm^{-1} spectral range (2.7-11.1 µm) with a 4 cm^{-1} spectral resolution. A gold mirror was used for reference for the reflectance spectra. IRidys (Infrared Imaging and Data Analysis) software was used

to analyze the spectrum collected by each pixel of the FPA. The gold reflector allows no transmittance, so the absorptance is again unity minus reflectance.

Figure 28 presents a top-down SEM image of a linear bolometer array. There is slight misalignment of the gold black on the square resistor elements, but not enough to cause thermal or electrical cross talk between pixels or short to the substrate.

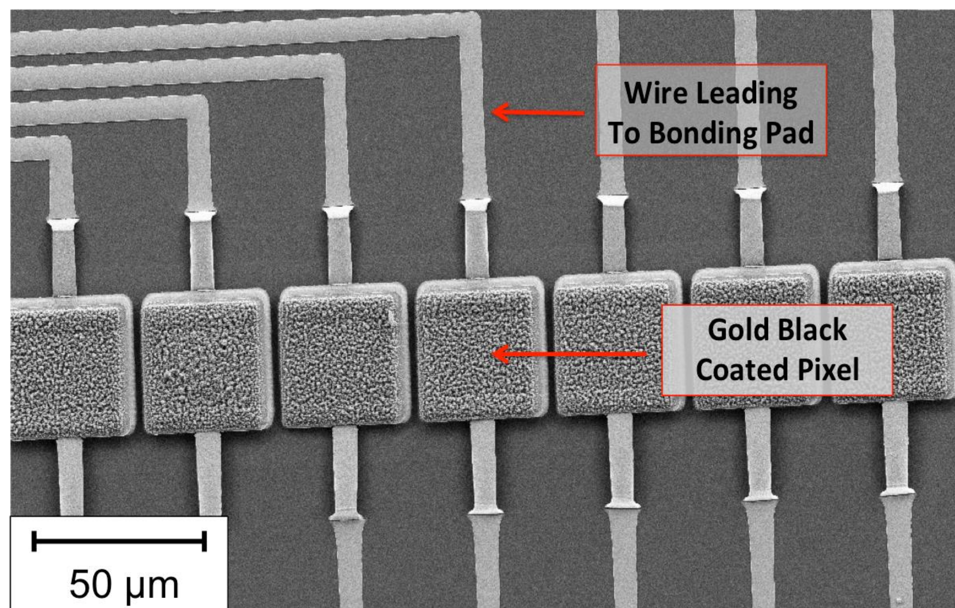

Figure 28. An array of gold black-coated pixels fabricated for testing purposes. In this image the gold black has been slightly misaligned, but is still electrically isolated.

Figure 29 presents SEM images of bolometers with (a) and without (b) gold black. The VO_x film is slightly inscribed within the pixel area, and it is protected on all sides by SiO_2. The NiCr arms come into contact with the VO_x film on either side of the pixel, and they support it above the substrate. The slight warping observed for the pixels affects mainly the Q of the Fabry-Perot resonant cavity formed by the air gap. The gold black film is uniform across the pixel, although it slopes down slightly around the edges. (The pixels

shown in Figure 29 have residual polyimide at the elbow joints of the arms. Such residues can also be seen with an optical microscope, which was used to confirm that such were absent from the pixels considered in responsivity studies.)

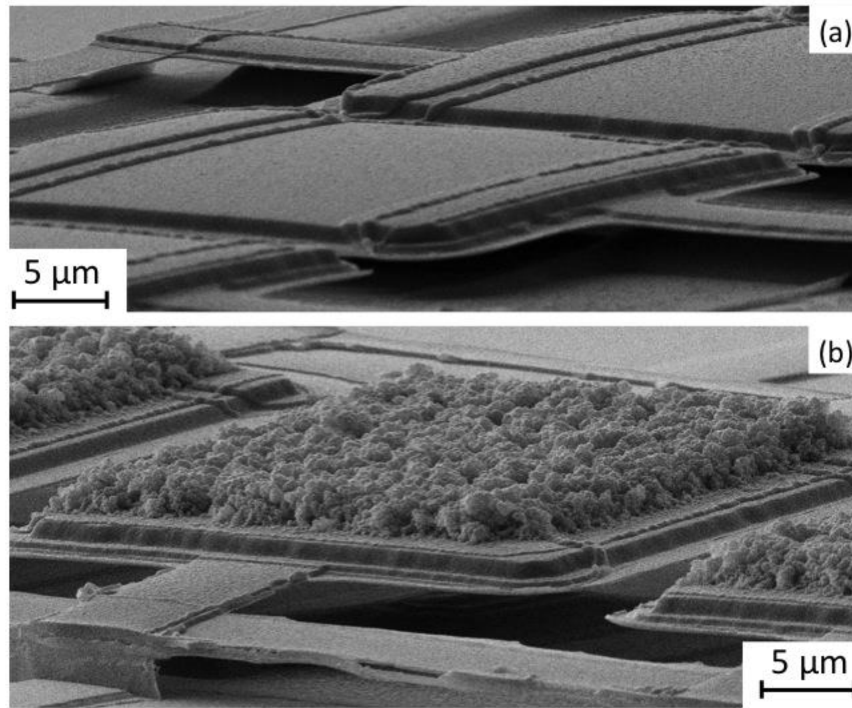

Figure 29. VOx air-bridge bolometers without (a) and with (b) the gold black coating.

4.2 Absorption Measurements

Figure 30 presents the specular and diffuse reflectance spectra *R* for a gold black layer with 250 nm SiO_2 protection. No dependence on angle of incidence appears until angles of about 45 deg. Diffuse reflectance is <1% for the LWIR and is only ~1% for the MWIR, indicating negligible scattering. The spectrally-averaged absorptance over the 8-12 µm LWIR wavelength band is ~70% for the smaller incidence angles, with a peak at 9.4 µm

of 93% due to the SiO_2. The absorptance averaged over the 3-5 μm MWIR wavelength band is ~86% for the smaller angles. In comparison to uncoated gold black, the absorptance is weaker, although the strong SiO_2 peak helps to compensate for this.

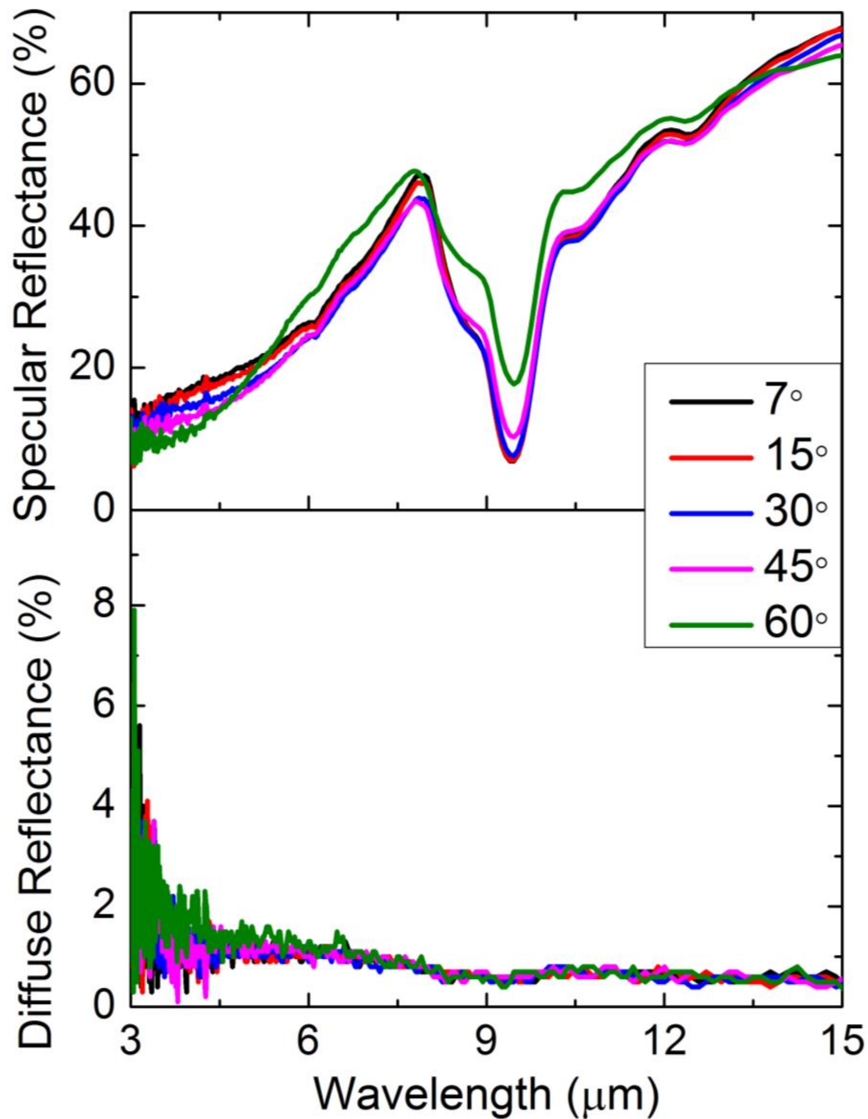

Figure 30. Specular and diffuse reflectance of SiO_2-protected gold black film on gold-coated silicon, at incidence angles of 7, 15, 30, 45, and 60°.

Figure 31 presents spatial maps of reflectance measured for MWIR (3-5 μm) and LWIR (8-11 μm). All four images have the same 35 μm x 35 μm field of view. The spatial sampling is 0.5 μm x 0.5 μm, so that the actual resolution is diffraction limited at all wavelengths. The pixel outline is represented by the black dashed line in images (a) and (c). The absorptance of bare pixels varies by 40% across the pixel, with the minimum at the center, where some points show almost zero absorption. The uncoated pixel's absorption is stronger in the LWIR than in the MWIR, due to the engineered Fabry-Perot resonance. However, the spatial uniformity is quite poor, which we attribute to the distortions in the FP cavity noted in Figure 29. A gold black coating greatly increases the absorption and its uniformity across the pixel in both bands. There is a narrow region around the edges with weaker absorption, because the gold black is thinner there, as can be seen in Figure 29.

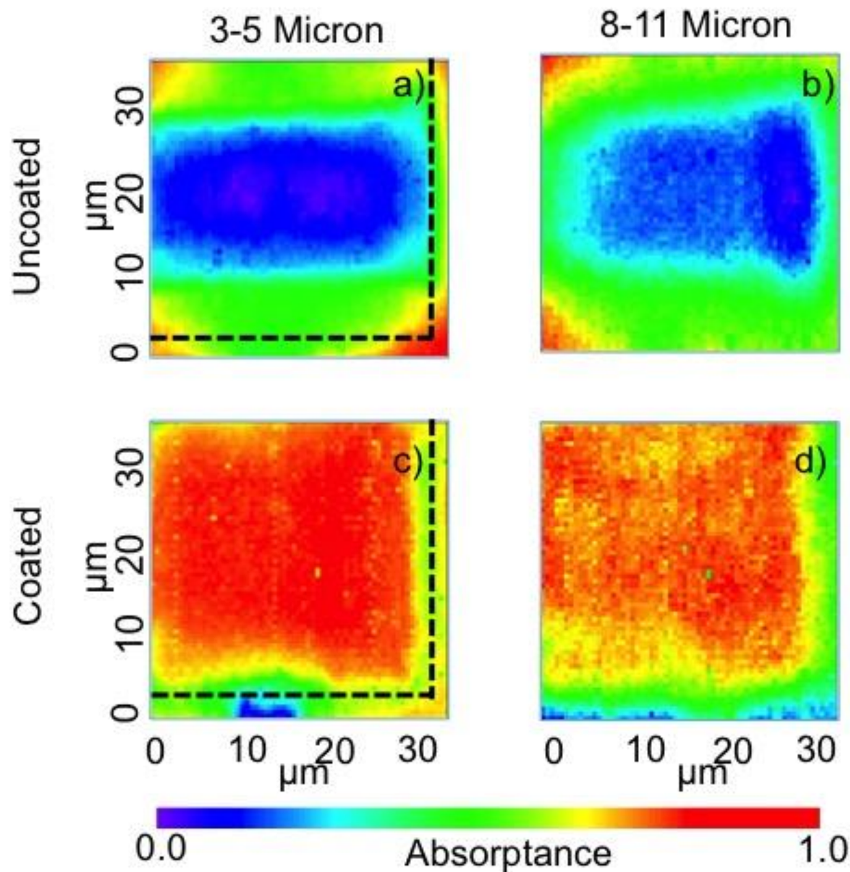

Figure 31 Spatial absorptance map for individual pixel. (a) and (b) show the absorptance across a single pixel without gold black coating for MWIR and LWIR, respectively. The corresponding absorptance for a pixel with the gold black coating is shown in images (c) and (d).

Figure 32 presents reflectance spectra obtained from spatial-averages over the pixel areas from the micro-FTIR images. For the uncoated sample, the Fabry-Perot absorption peak appears at 8.3 μm wavelength, indicating a cavity size just under 2.1 μm, which is well within the designed parameter. There is an SiO_2 absorption peak at 9.8 μm, which also appears in the spectrum for the gold black coated sample, although less pronounced due to the already high absorptance. The SiO_2 absorption is also observed in the oxide coated gold black sample (Figure 30). When the coating is added, the absorption increases over

the full 3 – 11 μm wavelength range of the measurement. The small oscillations in the spectrum for the sample without gold black are related to diffraction, as the period of oscillation is similar to the periodicity of the pixels in the array. These oscillations are not present in the spectrum for gold black because of low reflectance. The maximum spatially-averaged absorptance without gold black is only 64% for LWIR and less than 50% for MWIR. With the gold black coating the absorptance becomes ~90% and is fairly flat across the spectrum. The improvement is more in the MWIR than in the LWIR, where the absorption was initially strongest.

The absorption spectrum presented in Figure 32 for a single pixel is an improvement over the bulk reflectance data presented in Figure 30. A few fundamental differences between these two measurements may explain these results. Most obviously, the gold black patterned on the pixel benefits from any additional absorption from the SiO_2, VO_x-Au or the cavity. Additionally, the spectrum for the single pixel was taken at normal incidence, at which the absorption is maximized based on the trend observed for the bulk sample, although this effect would be minimal compared to the spectrum at 7° incident angle. Finally, the detection area is much smaller in the single pixel (35 x 35 μm^2) as opposed to the bulk measurements, in which the detection area was ~1 cm^2. With a larger detection area, any defects in the film will be integrated into the measurement. In the case of the gold black detectors, only pixels with no optically visible defects were tested.

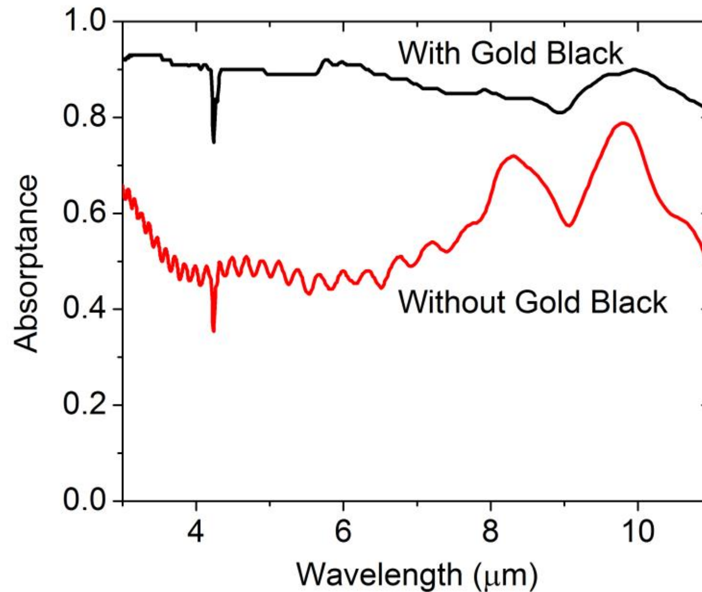

Figure 32. Absorptance spectra averaged over one pixel with and without gold black overcoat. The spike near 4.2 μm is an artifact due to atmospheric CO_2.

4.3 Responsivity and Noise Measurements

Fabrication yield was determined based on optical inspection and measured resistance. The most common failure is support-arm breakage, which results in an open circuit. Less common are electrical shorts from patterning misalignments. Inadequate or incomplete gold black coating occurs on fewer than 5% of pixels. Of the good pixels, we randomly selected and wire bonded 15 without the coating and 15 with the coating for testing. Detectors without gold black had an average resistance of 233 ± 17.5 kΩ, while coated detectors had an average resistance of 221 ± 25 kΩ. Load resistor values were selected in the range 200-250 kΩ to match the device under test. The signal voltage dV_{out}, defined in Eq. 18 based upon the voltage divider circuit, depends upon the quality of the impedance

matching, such that the approximation $\frac{R_L}{(R_L+R)^2} \approx \frac{1}{4R}$ can be made. The variation in the factor of ¼ due to imperfect load matching was less than 0.2%, far below the variance in detector resistance and the variance observed in dV_{out}.

Figure 33 presents measured voltage responsivity values $\mathcal{R}_v = \frac{dV_{out}}{dP}$ as a function of detector resistance. Chopping frequency was 80 Hz, and detector bias was 1 V. No optical filter was used, so the incident spectral range was defined by window transmittance to be 0.6 - 40 μm wavelength. The average responsivity for detectors without gold black was 753 ± 67 V/W, while the average responsivity for gold black-coated samples was 1110 ± 126 V/W. Thus, the coating improved the responsivity by 47%, which is much more than the 9 and 11% statistical uncertainties for the $\mathcal{R}_v$ values within each group, respectively. TCR goes as log(R) [24], so that the variation in $\mathcal{R}_v$ should be small over the range of resistances plotted in Figure 33. In fact, no trend in $\mathcal{R}_v$ is observed comparable to the statistical variations. This justifies the averaging represented by the horizontal dashed lines in Figure 33.

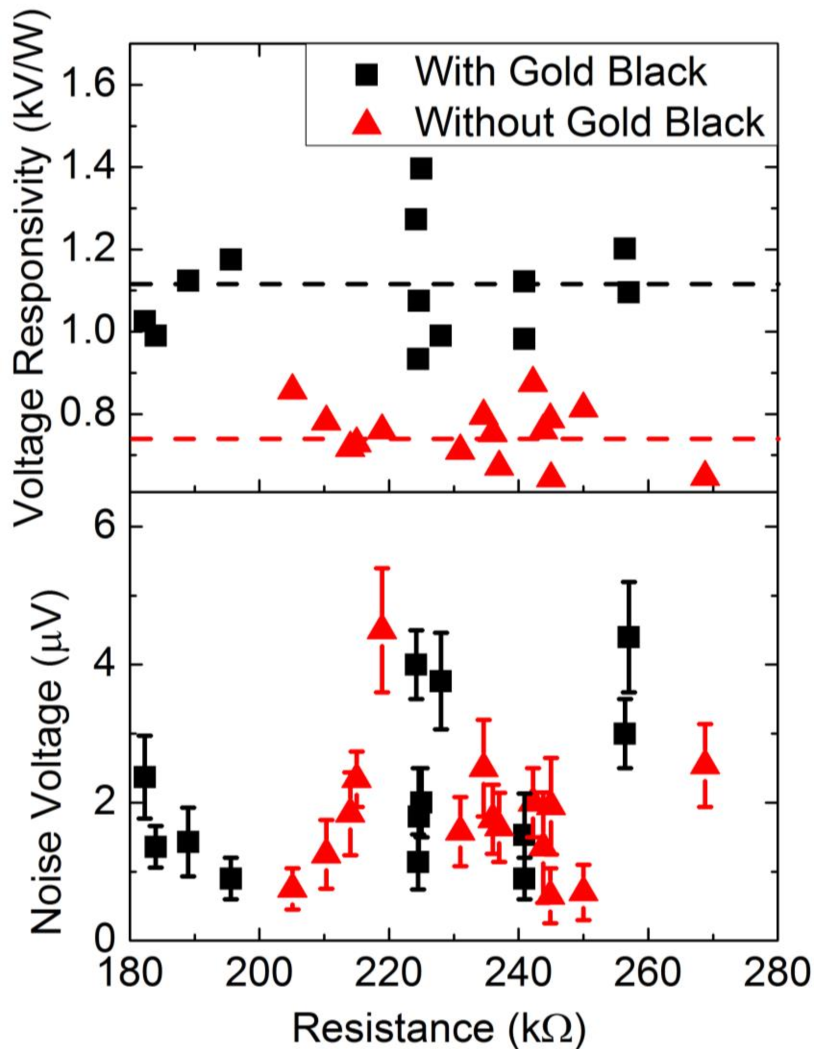

Figure 33. Voltage responsivity and noise voltage over a range of detectors, displayed as a function of detector resistance. Measurements are made at 80 Hz chopping frequency with 1 V applied bias and no optical filter.

The measured noise is presented in the lower part of Figure 33. There is no statistically significant increase in measured noise with the addition of the gold black film. The noise measurements exceed the ~250 nV expected for Johnson noise by a factor 10. While thermal fluctuation noise and photon noise contribute very little to the total device noise, the magnitude of 1/f noise is less easy to predict. To investigate the frequency dependence

of the noise, 5 samples with gold black and five without gold black were chosen at random from samples with resistances in the range of Figure 33. Figure 34 presents a plot of the measured noise voltage. Here, the noise voltage is doubled to show a full decade in the vertical scale. To fit the data, the 1/f noise given in Eq. 39 is integrated over the measurement bandwidth of 17 Hz, which solves to

$$V_f = \sqrt{k}\left(\sqrt{f+\frac{\Delta f}{2}}-\sqrt{f-\frac{\Delta f}{2}}\right), \tag{66}$$

where $\kappa = \frac{\alpha_H}{nV}$ is the fitting parameter and the bias voltage is 1V such that $\left(\frac{V_B R}{R_L+R}\right)^{\sim 2} \approx$ 0.25. The slope of the fitted lines is approximately -0.5 on the log scale, indicating the dependence on V of $f^{-1/2}$, as indicated in Eq. 39. The difference between the two curves is clearly much less than the statistical variation of the data, so that we conclude that gold black causes no increase in the noise. Using the volume of the VO_x film, we find values for the normalized Hooge parameter $\frac{\alpha_H}{n} \sim 1.5 \times 10^{-22}\ cm^3$. Wood [25] reports a similar value of $\frac{\alpha_H}{n} \sim 10^{-22} cm^3$ for VO_x films developed at Honeywell, while Basantani et al. [29] reports values in the range 10^{-17}-10^{-22} cm^3, with larger values holding for high resistivity VO_x films.

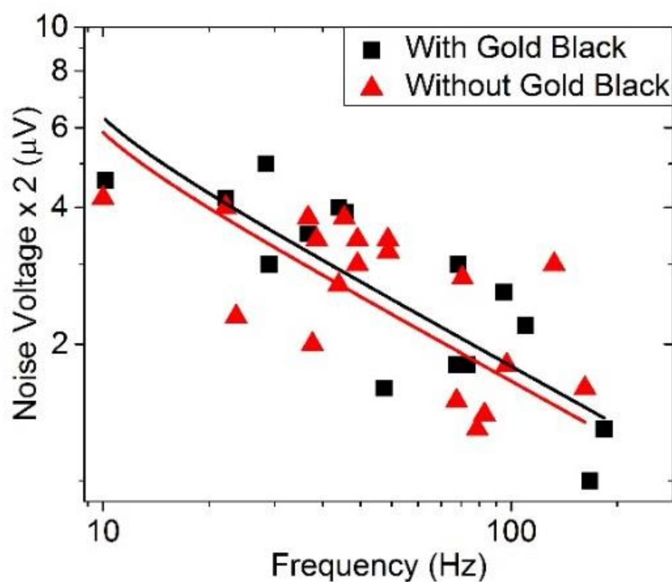

Figure 34. Measured noise voltage as a function of frequency for five devices with gold black compared with five uncoated device. A fit of the data generated by integrating Eq. 39 is presented, using a measurement bandwidth of 17 Hz.

It should be noted that this measurement considers the entire electrical path; the VO_x-Au film, the NiCr arms, bond pads, and even the electrical feed-throughs on the testing chamber. There is no clear explanation for 1/f noise; analytical calculations are based off of experimental data without the true mechanisms being fully understood. It has been suggested that 1/f noise is related to the number of defects in the electrical path of a material [24, 25]. As noted earlier, many failed devices tested with high resistance or open circuits, an effect that can be explained by the weak arms NiCr arms. Even for devices that measured with adequate resistance, it may be assumed that the arm path contains defects related to this fragility. Additionally, the embedded gold particles in the VO_x film create extra surfaces between various grains of vanadium oxide. The shortest electrical path is

through these low resistance gold particles, therefore these Au/VO_x interfaces may be viewed as defects in terms of 1/f noise.

The absorbing gold black film is electrically isolated from the VO_x-Au film by a thick layer of SiO_2. The addition of gold black to a pixel in no way will increase the resistance of the film or the number of defects in the electrical path. The added absorption and bandwidth will increase the background fluctuation noise, or photon noise, of the detector by an amount of $\sqrt{\Delta\eta}$, the square root of the increase in absorptance. Thermal fluctuation noise may be affected by the increase in thermal response time due to added heat capacity. However, as it has been shown that Johnson noise and 1/f noise dominate, the increase in total noise due to the addition of gold black should be marginal at best, which is consistent with experimental observation.

The voltage responsivity is given in Eq. 29, which may be written as

$$\mathcal{R}_v = \frac{\mathcal{R}_0}{\sqrt{1+(2\pi f)^2\tau^2}}, \tag{67}$$

where $\mathcal{R}_0 = \frac{V_B\alpha\eta}{4G_{eff}}$ is the voltage responsivity at $f=0$. Figure 35 presents $\mathcal{R}_v$ for one pixel as a function of chopping frequency from 10 to 150 Hz for detectors with and without gold black. The applied bias was 1 V and no optical filter was used in this data. Values are excluded near 60 Hz due to high noise. The parameters for $\mathcal{R}_0$ and τ_{th} were determined by fitting these data with the function in Eq. 67. This fit (solid lines) shows that the DC

responsivity increases from 4.13 to 6.24 kV/W by adding gold black, an increase of 51%, while the thermal response time only increases by 15%, from 9.57 to 10.97 ms.

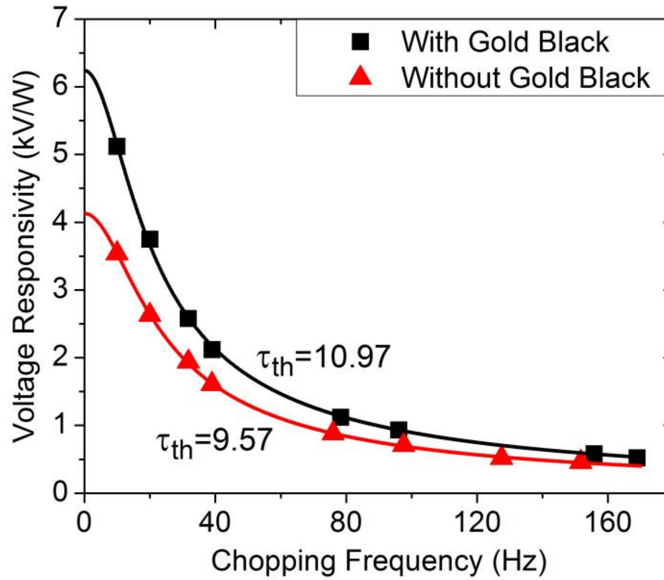

Figure 35. Voltage responsivity as a function of chopping frequency. The solid lines are fits to Eq. 29.

The values determined from the fitting parameter $\mathcal{R}_0$ allow an estimate of the effective thermal conductance G_{eff}, assuming the TCR to be -2.0% and the absorptance to be 0.85 for gold black-coated samples and 0.54 for uncoated samples, as shown in Figure 32 for 3-11μm. This yields thermal conductance G values of 6.5 x 10^{-7} W K^{-1} and 6.8 x 10^{-7} W K^{-1}, respectively, i.e. an increase of 4% caused by the coating. The smallness of this increase emphasizes that the main thermal conductance path is the arms, which are unaffected by the coating.

The fitting parameter τ and the just determined value for G allow an estimate of heat capacity C using Eq. 27. For bare and coated bolometers we find $C = 6.26 \times 10^{-9}$ and 7.47×10^{-9} J K^{-1}, respectively, i.e. the coating increases C by 19%. The density of protected gold black after lift-off was estimated to be 8% of bulk gold [17], so a 2 μm thick layer of gold black with 250 nm SiO_2 should add 0.87×10^{-9} J K^{-1} to the heat capacity, or a 14% increase, which is in reasonable agreement with the value obtained from the fit.

Figure 36 presents the effect of restricting the spectral range with an optical filter on the responsivity improvement achieved with gold black coating. This data was taken with a modulation frequency of 37 Hz. Additionally, a higher applied bias of 3V was chosen to counteract the reduced incident power due to the optical filters. Without an optical filter, the bandwidth incident on the detector was window-limited to the range 0.6 - 40 μm wavelength, but there is effectively no irradiance beyond about 20 μm, according to the 300˚C black body curve also plotted in Figure 36. The improvement is smallest for the LWIR band, where the uncoated bolometers already had significant absorption due to the resonant cavity and the oxide. The improvement for the MWIR band is much larger and is comparable to that obtained over the full unfiltered band.

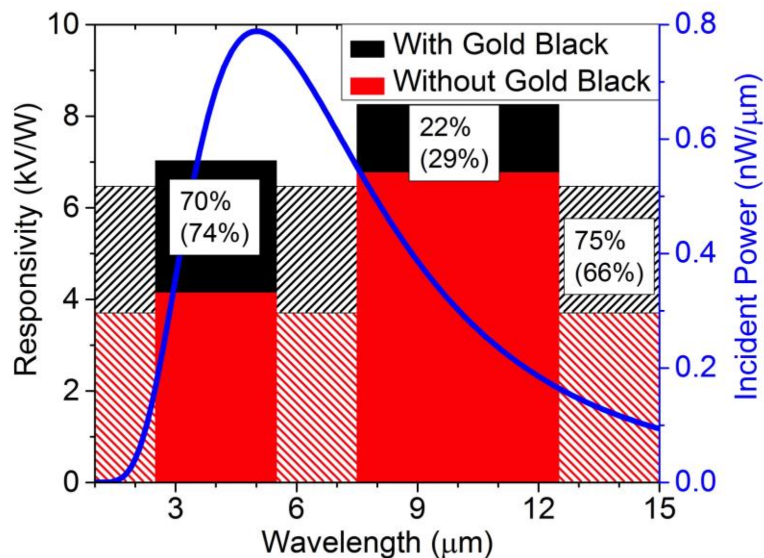

Figure 36. Voltage responsivity as function of IR bandwidth, which is given by horizontal limits of each bar. The solid curve is the incident power spectrum based on the blackbody radiance at 300˚. The upper percentage labels give the responsivity increase due to the gold black coating, while the lower values in parentheses give the absorptance increase for the same range. Note that the range for LWIR responsivity is 7.6-14.6 µm, while the LWIR absorption range is only from 7.6-11 µm. Measurements taken at 37 Hz with 3V applied bias.

4.4 Absorption Effects from Thermal Processing

Gold black is vulnerable to thermal effects [49]. The mechanism by which gold black achieves high absorption is related to the porosity and size of the web-like structures within gold black, which by their own nature have high surface area and thus a high chemical potential, leaving the system in a thermomechanical unstable state. To be suitable for commercial IR imaging systems, gold black must be able to survive standard vacuum

sealing techniques, in which temperatures can be raised above 300˚C for a period of time [66, 67]. This heating is expected to degrade the absorption of gold black significantly.

To investigate this effect, a gold black film with evaporated SiO_2 overcoat was prepared in the usual manner for FTIR spectroscopy. This sample was broken into multiple pieces for thermal processing. One was kept as the reference. Two other samples were heated on a hot plate for 10 minutes at 100˚C and 300˚C, respectively.

Infrared characterization of the effects of thermal processing on gold black was performed by collecting reflectance spectra at normal incidence from 3 to 15 μm wavelength. A Bomem DA8 FTIR spectrometer with globar source, KBr beamsplitter, and 77 K HgCdTe detector were used. The substrates for the coatings used in these studies had a thick Au coating to ensure zero transmittance, so that absorptance is one minus reflectance. The reference spectrum for determining the reflectance was measured on a gold mirror.

Figure 37 presents the reflectance spectra for heated gold black films, which show that the heat treatment increases the reflectance and degrades the absorption. There is little degradation after heating at 100˚C, particularly for the MWIR. At higher wavelengths, this degradation is enhanced. At 300˚C, the effect is much more pronounced, although the trend with wavelength is still present. The SiO_2 absorption feature shows little change from thermal stress, implicating the degradation is due to a change in the microstructure of the gold black.

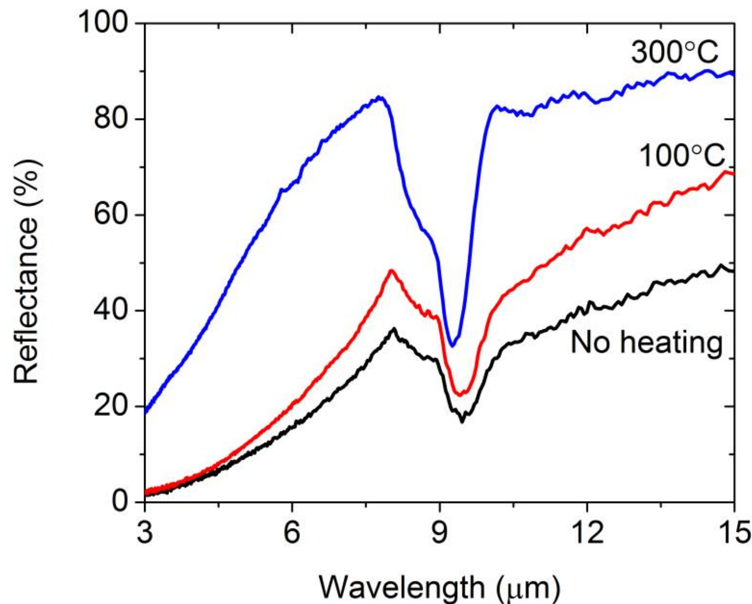

Figure 37. Reflectance spectra of gold black after annealing at the indicated temperatures for 10 minutes.

In an effort to reduce this effect, a fourth sample underwent a PECVD deposition of 350 nm SiO_2, in which the processing temperature is 300˚C for approximately 10 minutes. Figure 38 compares the reflectance of these two samples with nearly identical thermal processing. While both films have a weaker absorptance than an unheated film, the absorption is increased for a film with the additional PECVD processing, despite the heat load. Due to the increased SiO_2, this absorption band is much higher just above 9 μm. Additional absorption band are also present in the PECVD sample. This suggests that PECVD oxide may utilized to thermally stabilize the film, although the effect may be explained simply by the additional absorbing material.

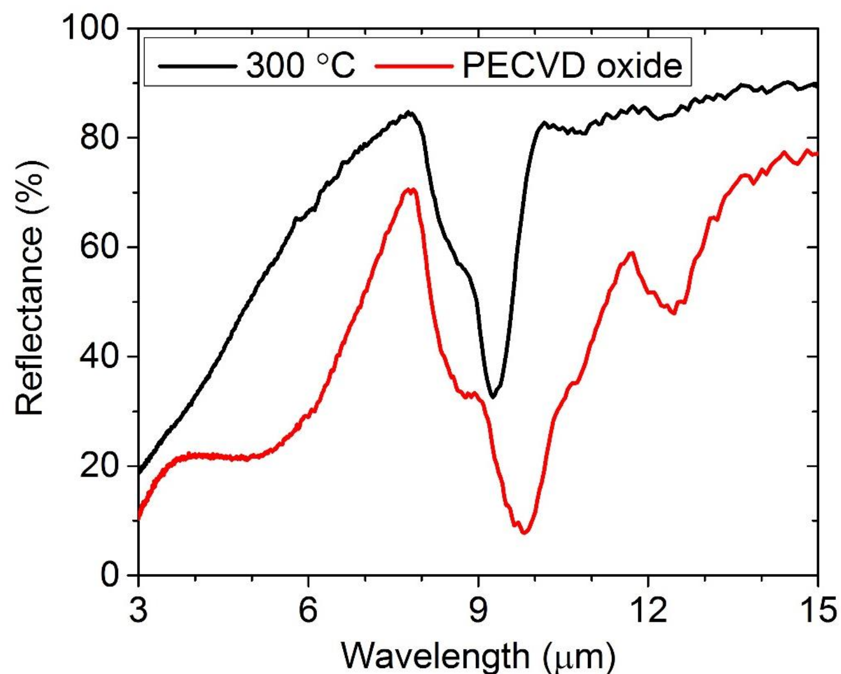

Figure 38. Comparison of protected gold black films under similar thermal processes. The red curve shows the reflectance of a sample that has an additional 350 nm SiO_2 deposited in a 300˚C PECVD process.

Gold black films were investigated using SEM imaging both in top-down view and in cross section. Figure 39 shows the top-down images of the unheated sample, heated samples at 100˚C and 300˚C, as well as the PECVD coated sample. These images reveal the size and topography of the SiO_2 on top of the gold black. Images (a), (b), and (c) show nearly identical particle sizes, although the sample heated at 300˚C (c) has particles more conglomerated together. Heating therefore seems to influence the spacing of particles and thus the size of the voids, however the SiO_2 particle sizes remain unchanged. The PECVD

oxide forms as large, conglomerated particles with few voids present. As PECVD deposition is much more conformal than evaporation, this process makes the surface much more planar, which may be desired in a process that would require any patterning steps beyond the deposition of gold black. The dark and bright spots in this image are a charging effect from the electron beam in the SEM.

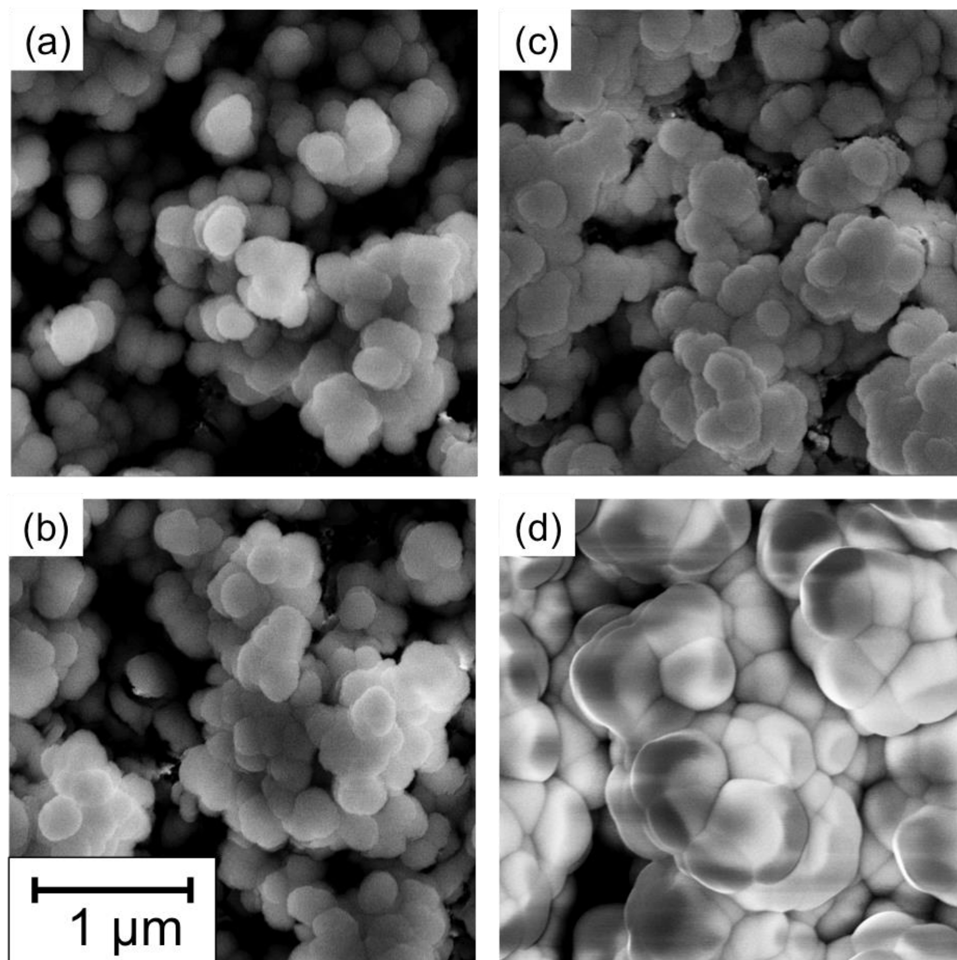

Figure 39. Top-down view of gold black films coated in SiO_2. The first sample (a) has had no heat treatment, while (b) and (c) have been heated on a hot plate at 100˚C and 300˚C, respectively. 350 nm PECVD oxide has been deposited on (d), during which thermal treatment was very similar to (c).

Figure 40 presents cross section images of the four samples. The SiO_2 overcoat imaged in Figure 39 can be seen, and the observations regarding particle size, voids and planarization are confirmed. The surface topography is smoothed as a result of heating, and even more so with the PECVD oxide, in which surface non-uniformities occur on a much larger scale. More interesting in these images is the grain structure and apparent thickness of the gold black. The unheated sample (a) appears similar to that heated at 100˚C (b). The thicknesses of these films are approximately 1.6 μm and the web-like structure of gold black is still intact. The gold black has collapsed and begun to coalesce after 300˚C heating (c). The web-like structure has largely been replaced with crystallites having a diameter on the order of 100nm. The thickness of this film has dropped to 1.2 μm. The result is a film with far fewer voids in which to trap light. Interestingly, the sample with PECVD oxide (d) shows less evidence of collapse and coalescing of the gold black chains (although still much more than (a) and (b)). While the heat has still been detrimental to the film, this additional oxide film helps to stabilize the film from further collapse.

As gold black collapses, the microstructural features that allow gold black to be a good absorber (i.e., small scale porosity that enables light trapping) are reduced. This means that absorption is lost in the longer wavelengths first, while the shorter wavelengths are still effectively absorbed. This is evident in the reflectance spectrum in Figure 37, as well as the color of the films. Gold black appears black because it highly absorbs light in the visible spectrum. After being heated, red light is partially reflected, while the other colors are still absorbed. The thermal degradation of gold black indicates the need for new low-

temperature methods of vacuum packaging for arrays so coated. Research in low temperature vacuum sealing is ongoing [68, 69].

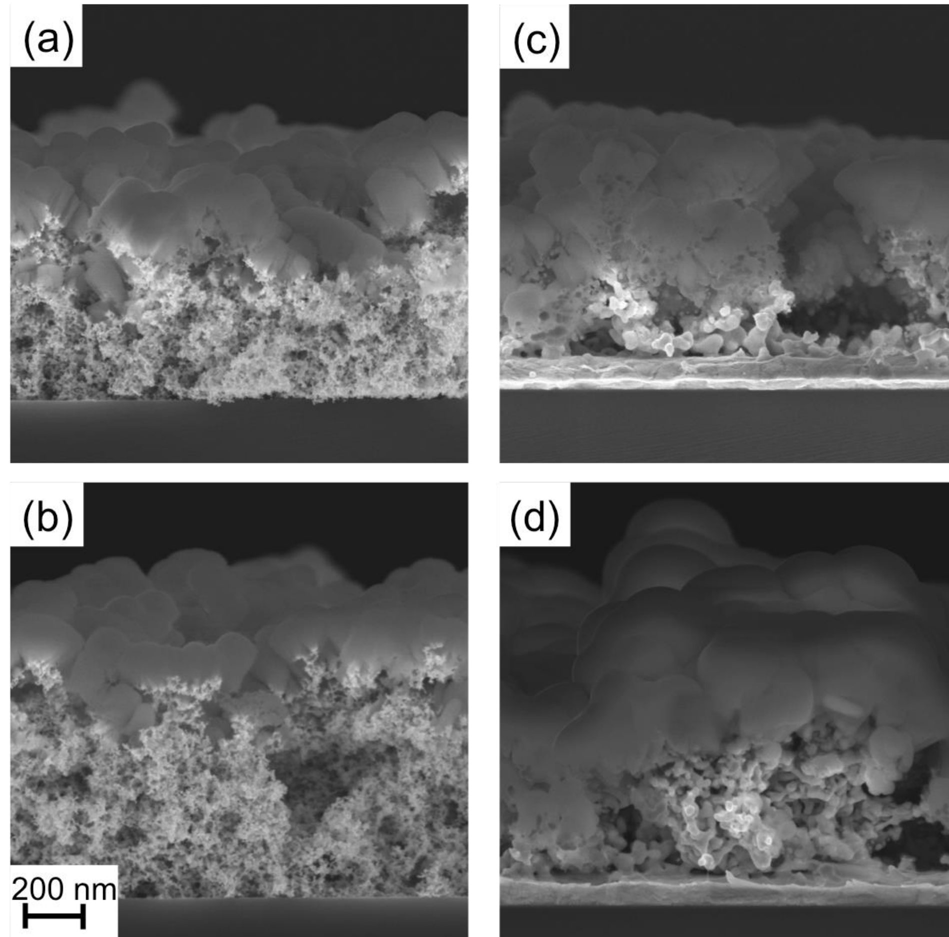

Figure 40. SEM cross section images of investigated samples: (a) unheated, (b) 100˚C, (c) 300˚C and (d) PECVD additional overcoat.

4.5 D* and NETD

Measured responsivity and noise values can be used to calculate total device performance in terms of NEP, D* and NETD, using Eqs 51, 52, and 60, respectively. Table 4 shows these values for 3 different testing conditions. All three of these tests consistently show an

increase in D*, which leads to a potential decrease in NETD for an imager. The greatest increase in device performance is at 30 Hz modulation frequency, which is a consequence of the increased thermal response time. For LWIR, only a modest increase in D* is observed, as was seen in Figure 36 in responsivity comparisons.

Table 4. Comparison of D and NETD for devices with and without gold black under various testing conditions*

Testing Conditions	NEP [W]	D* [cm√Hz W^{-1}]	NETD [mK]	% Increase D*	% Decrease NETD
No Gold Black, 1V, 80 Hz	1.06×10^{-9}	1.32×10^{7}	2388.78	33%	-25%
Gold Black, 1V, 80Hz	8.02×10^{-10}	1.76×10^{7}	1802.80		
No Gold Black, 1V, 30 Hz	5.51×10^{-10}	2.55×10^{7}	1239.34	48%	-33%
Gold Black, 1V, 30 Hz	3.72×10^{-10}	3.79×10^{7}	835.38		
No Gold Black, 3V, 37 Hz, LWIR	6.09×10^{-10}	2.31×10^{7}	1368.69	17%	-14%
Gold Black, 3V, 37 Hz, LWIR	5.21×10^{-10}	2.70×10^{7}	1170.77		

The measured D* values are about an order of magnitude lower than comparable commercial devices, even considering the enhancement gained by the gold black absorber. To some extent, the TCR of VO_x in commercial devices may be ~50% larger than that used in these devices [4], and the detector redesign discussed in Chapter 3 demonstrated the possibility of decreasing the thermal conductance by as much as a factor of 3. Therefore the discussed fabricated device potentially has a responsivity ~4.5 times less than commercial devices.

These devices suffered from a higher than anticipated noise floor that is roughly an order of magnitude higher than the Johnson noise. This is much more likely to be the source of the low D*. For the same responsivity, D* would be ~10^8 for Johnson-noise limited devices.

4.6 Summary

Results presented demonstrate the potential of patterned gold black as a dual band, wide-angle absorber for improving the responsivity of room temperature bolometer arrays. Gold black films protected by evaporated oxide were successfully patterned by lift-off onto pixels of the microbolometer, giving a spectrally averaged responsivity improvement of ~50%. In the LWIR band, the improvement was nearly 30%, and it was over 70% in MWIR. The coating increased the thermal time constant by ~15%, but the detectors remain sufficiently fast for standard 30 Hz video frame rates. A vacuum packaging method that maintains array temperatures below 100 ˚C would be required to avoid degrading the gold black coatings.

CHAPTER FIVE: SENSITIVITY ENHANCEMENTS USING SUB-WAVELENGTH RESONANT ABSORBERS

5.1 Theoretical Considerations

Thin film metamaterial, or plasmonic resonant absorbers, were discussed in Chapter 2 as an alternative to a metal black for enhanced absorption and sensitivity of an infrared microbolometer. Such films can be advantageous as they can achieve high absorption using relatively thin films, so that heat capacity and therefore thermal response time have minimal increase. While explanations for the absorption vary between a metamaterials approach, which utilizes effective medium theory based off of the electric permittivity and magnetic permeability of a material [15], to an interference approach, which is based off of phase-matching of electromagnetic waves similar to Fabry-Perot resonances [70], it is agreed that the absorption is related to the dimensions of sub-wavelength structures. Nath et al. [71] recently developed such a resonant absorber structure based on a metal-dielectric-metal (MDM) structure. This structure was developed for LWIR and far-IR (wavelengths longer than 12μm), in which the resonant absorption frequencies are dependent upon designed dimensions, and are therefore configurable to a wide range of bandwidths. Absorption in Ref. [71] is highest at 53.5 μm and 30 μm, where the absorption is 95% and 98%, respectively, while the same design with different dimensions has a peak absorption of 93% at 6.7 μm wavelength [23].

Such a resonant absorber is preferable to gold black in that it is not subject to any aging or heating degradation. Furthermore, this process involves standard e-beam evaporation of metals and dielectrics, while gold black requires a slightly more exotic deposition method that may not be compatible with all labs and foundries. Like gold black, these absorbers can be easily patterned through standard UV-photolithography. However, the absorber is not quite as broadband as gold black, and although the film thicknesses are comparable, the porosity of gold black allows it to have low heat capacity compared to the resonant absorbers described here, so a higher increase in thermal response time is expected. The goal of this investigation was to determine performance enhancements of the microbolometer after integration with the described resonant absorber, and to define the potential drawback associated with this method.

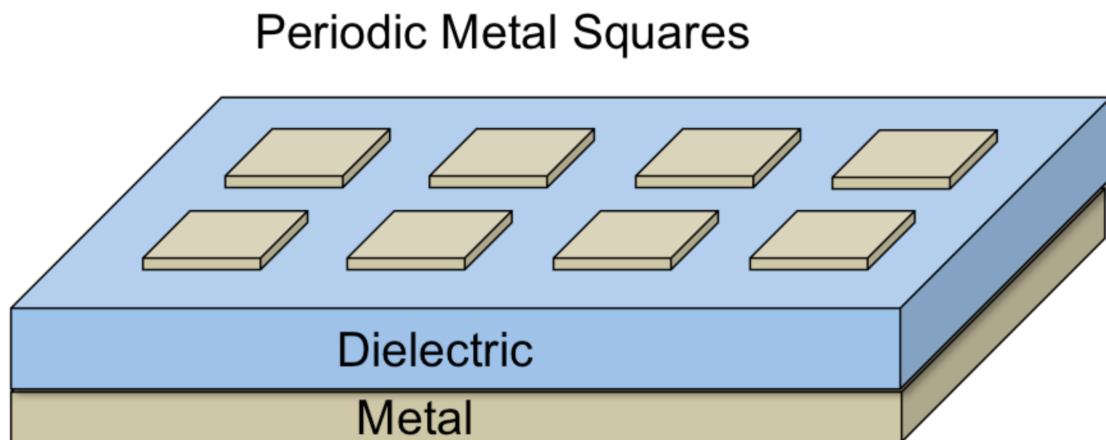

Figure 41. Schematic of the structured metamaterial absorber.

Figure 41 presents a schematic of the structured thin film absorber. The ground plane consists of optically thick gold with a titanium sticking layer, followed by a dielectric layer

(SiO_2) of thickness *t*. Optically thick gold squares are patterned on top of the SiO_2 in a periodic array with square dimension *l*. A standing wave resonance model accurately predicts the resonant absorption wavelengths [71]. This model considers electromagnetic waves traversing through the SiO_2 emanating from the edges of the top metal squares, driven by a periodic polarization induced from incident radiation. Based upon multiple reflections *b* off of the metallic surfaces, the mth order standing wave resonance occurs at wavelength [71]

$$\lambda(b,m) = \frac{2(b+1)n(\lambda)}{2m+b}\sqrt{t^2 + \frac{l^2}{(b+1)^2}}, \tag{68}$$

where $n(\lambda)$ is the wavelength dependent index of refraction of the SiO_2. It should be noted that, by symmetry, the number of reflections *b* will always be odd. The maximum resonance should occur at the fundamental $m=0$ mode for $b=1,3$. Hence, the absorption bands for this film are functions configurable by adjusting the thickness *t* of the dielectric and the length *l* of the gold square. Dependence on any other parameter, such as periodicity, is very weak [72]. Therefore the absorption profile can be explained even for a single square. Multiple absorption bands are achieved by using SiO_2, which is a dispersive dielectric, with such absorber structure. Strong wideband absorption is reported for such structures which cover almost the entire LWIR region [72].

5.2 Experimental Methods

The designed metamaterial absorber was patterned and deposited onto trench-etch microbolometers, the latter of the two designs described in Chapter 3. Therefore detectors in this investigation were much more robust, had a lower resistance with smaller variance, and arrays had a higher yield. A single wafer containing hundreds of individual detectors was fabricated. The absorber was patterned directly on top of a thick PECVD oxide layer, ensuring electrical isolation from the VO_x film. The total area of the absorber was 35 x 35 μm^2, matching the size of the VO_x-Au film. A shadow mask covered half of the wafer during depositions for the absorber, so that half of the devices could be kept without the absorber for comparison. The absorber metal (200 nm Au with 10 nm Ti sticking layer) and dielectric (1.3 μm evaporated SiO_2) layers were patterned first by a lift-off technique. Then, 150-nm-thick gold squares with 5 μm lateral dimension in a 7.5 μm period two-dimensional array were patterned on the bolometers by a second lithography step. The detectors were again patterned and covered in photoresist as an etch mask for the isotropic silicon etch in a fluorinated plasma to form the air bridges.

For characterization of absorbers independent of the bolometers, the absorber structure was patterned over large areas of a silicon substrate. The squares were fabricated using standard i-line UV photolithography.

Infrared characterization was performed by collecting reflectance spectra at normal incidence from 3 to 15 μm wavelength. A Bomem DA8 FTIR spectrometer with globar source, KBr beamsplitter, and 77 K HgCdTe detector were used. Transmission was

confirmed to be zero due to the optically thick gold ground plane on the silicon substrate, and no scattering is expected from the subwavelength squares. Hence, the absorptance is one minus reflection. The reference spectrum for determining the reflectance was measured on a gold mirror.

Figure 42 presents SEM images of detectors with and without the absorbers. The top image of the detectors without absorbers is taken from a separate wafer designed with a higher fill factor, but in every other regard the design is identical to the detectors tested in this work. One thing to note is that the edges appear rougher in the bottom image. This is an effect from silicon or "grass" that is formed during the fluorinated plasma etch. This is an unwanted byproduct common to this etch chemistry related to contaminants materials [73]. As this etch chemistry will etch both silicon and silicon dioxide (although the latter with a much slower rate), a photoresist etch mask must be utilized. The residue was not completely removed even with an oxygen plasma clean. Due to the minimal presence of this residue and location on the sample, it is not believed to have any measureable effect in our experiments.

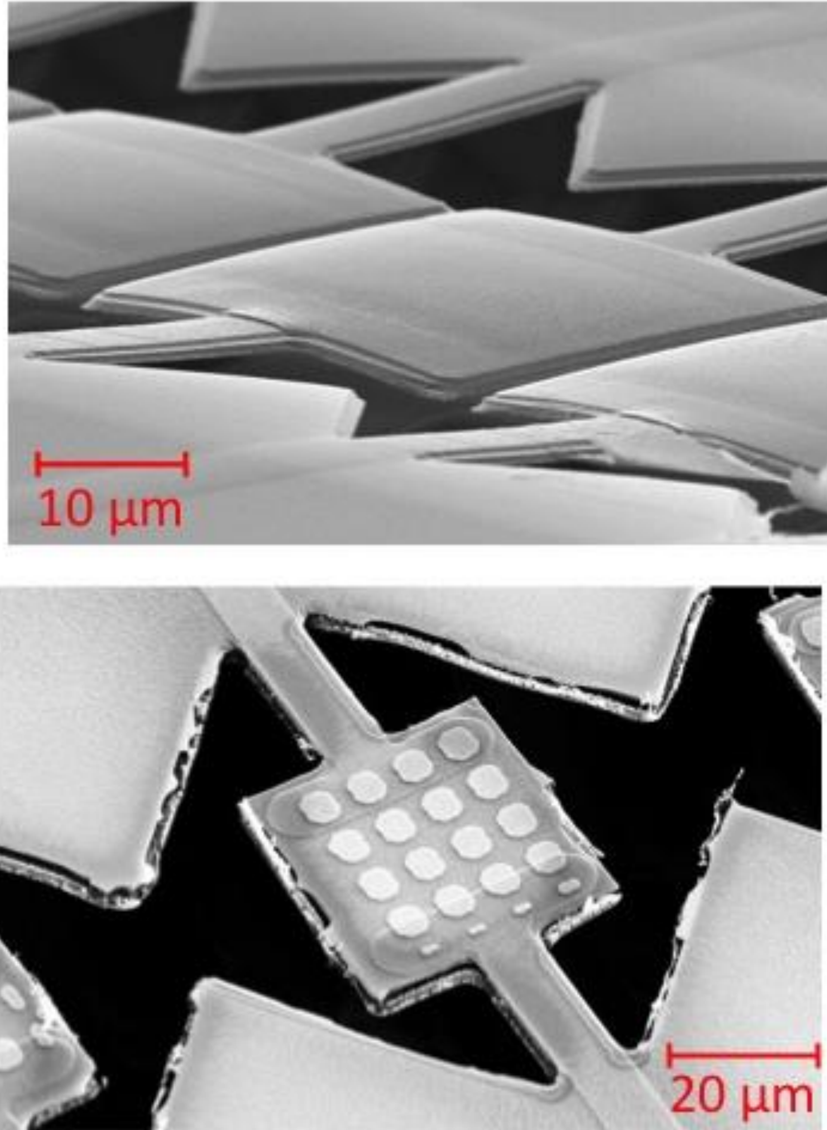

Figure 42. Comparison of detectors without patterned metamaterial (top) and with the metamaterial detector patterned (bottom).

Figure 43 compares top-view SEM images of the large reference absorber array and a smaller array selectively patterned onto a single bolometer element. Both arrays have a period of 7.5 µm and a lateral dimension of ~5 µm. The edge squares on the microbolometers are deformed due to the selective pattering process. Due to the nature of

the patterning process, different detectors had slightly different numbers of square patterns, as can be viewed by comparing the squares in Figure 42 and Figure 43. Theoretical analysis suggests little influence of periodicity on absorptance, although non-uniform square sizes will result in a smaller effective absorbing area or non-uniform absorption peaks across the pixel. Some variation in measured signal is expected from this non-uniformity from pixel to pixel.

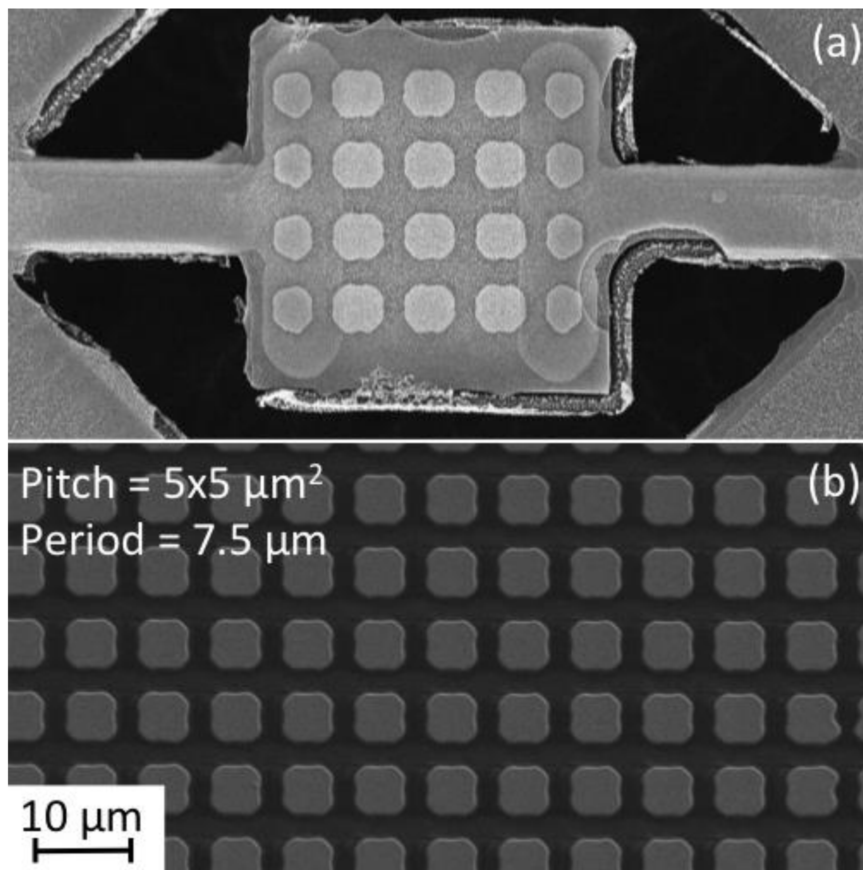

Figure 43. SEM images of (top) absorber structures on VO_x air-bridge bolometer and (bottom) absorber structures on Si substrate.

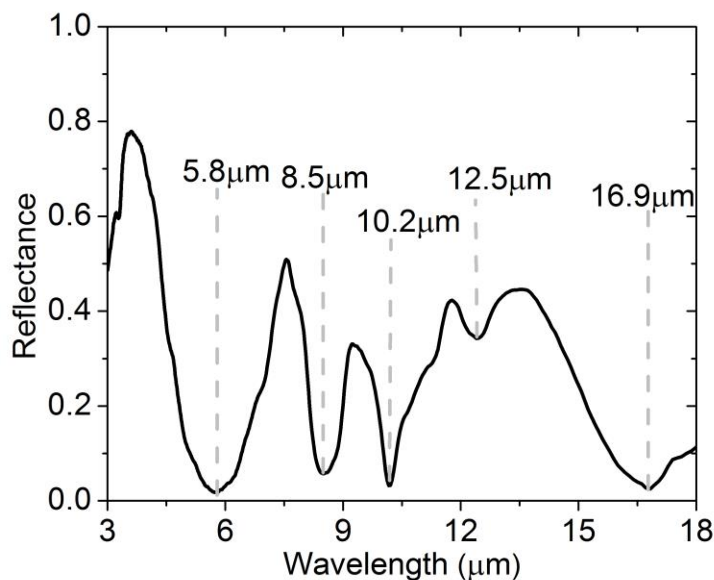

Figure 44. Reflectance spectra of absorber structure measured by FTIR. Reflectance minima (absorption peaks) are labeled.

Measured reflectance spectra are plotted in Figure 44. Multiple absorption bands appear at 5.8 µm, 8.5 µm, 10.2 µm, and 16.9 µm, with a small peak appearing at 12.5 µm. The peak at 10.2 µm corresponds to the absorption band of SiO_2, although slightly red-shifted due to the resonance of the squares. Because multiple bands overlap in the LWIR, the average absorption over this region is ~80%. Average absorption across the MWIR is only ~45%, which is still an improvement for a detector designed for LWIR.

Fabrication yield for devices was over 95%, based off of measured electrical resistance and mechanical stability. Patterned absorbers ideally would have a 4x4 array of squares visible on the surface. Due to fabrication limitations and low tolerance arising from the small critical dimension of the pattern, some pixels had fewer squares. The failure mode for

absorbers was determined by the number of visible squares on the surface under an optical microscope; detectors with fewer than 50% of the surface patterned (less than 8 full-sized squares) were deemed an unsuccessful absorber. Based upon this metric, the yield on patterned absorbers was only around 50%, and was largely dependent on the position of the wafer. That is to say, some sections of the wafer would have near 100% yield while other sections would have close to 0% yield.

Responsivity and noise measurements were carried out in a similar method as described in Chapter 3, however the electronic read-out circuit was slightly different. These detectors were designed to be part of an imaging system using a custom amplifier and ROIC that would measure all devices in an array. For single pixel measurements conducted for this study, the simple voltage divider electronics were utilized instead. However, to accommodate the custom electronics for the imager, detectors were fabricated with on-chip impedance-matched load resistors connected to a common ground. Thus, instead of directly measuring the voltage across the detector, the voltage across the equivalent resistance of the detector and the load resistor was measured. As $R \approx R_L$ to within the measured standard deviation (1.1%), $R_{eq} \approx \frac{R}{2}$.

For blackbody testing, ten devices without absorbers and ten samples with absorbers were chosen at random from among pixels that were deemed successful. For detectors with absorbers, the average equivalent resistance was 45.75 ± 0.31 kΩ, such that the detector resistance was 91.50 ± 0.62 kΩ. The average equivalent resistance for detectors without patterned absorbers was 40.01 ± 0.60 kΩ, such that the detector resistance was 80.02 ± 1.2

kΩ. Resistance differed between the two groups by roughly 12%. The difference in resistances between the two groups is larger than the standard deviation within the groups, so in this sense the difference is systematic. The absorber is electrically insulated from the VO_x-Au film, and the bottom layer of the absorber structure is a gold ground plane. Any interference this supplies on the electrical path, by design or by a fabrication error, would likely be a short, and thus decrease the resistance; the observed effect is an increase in resistance. It is unlikely, therefore, that this change in resistance is related to the application of the absorber, and more likely indicative of non-uniformity across the wafer of the deposited VO_x-Au film.

5.3 Responsivity and Noise Measurements

Bolometer testing conditions and results are presented in Table 5. For each set of conditions, measurements for the 10 different elements were averaged. Applied bias was 1.0 V in each case. "Full" bandwidth means the measurement was performed without an optical filter, so the incident power spectrum depended only on the blackbody spectra, atmospheric transmission, and the KRS-5 transmittance. For "LWIR" bandwidth, an AR-coated germanium long pass optical filter was used (Edmund Optics 68656) which has a spectral window of about 7.6 µm-14.6 µm. The lock-in time constant was 30 ms, giving a measurement bandwidth Δf of ~17 Hz.

The responsivity was highest at 35 Hz modulation frequencies, which is acceptable for video frame rates. The responsivity was consistently higher with an absorber than without.

For 35 Hz modulation frequency, the detectors with absorbers showed a 71% increase in responsivity, but only a 56% increase at 100 Hz. This is largely due to the increase in thermal time constant with the additional mass of absorber. With LWIR filter, responsivity improvement drops to 49%. The absorbers used have a much broader absorption bandwidth than the detectors achieve using a Fabry-Perot cavity alone, which is designed for LWIR. The higher responsivity for the full band measurements is largely due to increased absorption outside of the LWIR bandwidth.

Table 5. Data averaged over 10 detectors with and without the absorbing structure.

Modulation Frequency [Hz]	Bandwidth	Detector	Average Responsivity [V/W]	Average Noise Voltage [μV]
35	Full	Absorber	1399 ± 36	0.67 ± 0.37
		No Absorber	817 ± 21	0.49 ± 0.29
100	Full	Absorber	656 ± 14	0.73 ± 0.35
		No Absorber	420 ± 14	0.49 ± 0.25
35	LWIR	Absorber	2171 ± 51	0.42 ± 0.16
		No Absorber	1457 ± 36	0.33 ± 0.17

The measured noise was consistently larger for devices with the absorbers. At 35 Hz modulation, the noise increased by 36%, while a slightly higher increase of 48% was observed at 100 Hz, almost equal to the increase in responsivity. The smallest increase was observed for LWIR measurements at 27%. It should be noted that while this increase is observed to be systematic, it is also smaller than the observed standard deviation of the measurements, which is approximately 50%. Therefore the data are not sufficiently statically significant to conclude that the addition of the resonant absorbers increases the noise of the devices.

With a resistance of 80-90 kΩ, the Johnson noise for measured devices should approximately 200 nV by Eq. 30, which is 2-3 times lower than presented in Table 5. It was observed in gold black testing that 1/f noise was a higher noise source than originally expected, so it is reasonable to assume that 1/f noise is a larger source in these devices as well. This assumption is not supported by the results in Table 5, as noise remains more or less constant between 35 Hz and 100 Hz, but this effect was looked into more closely.

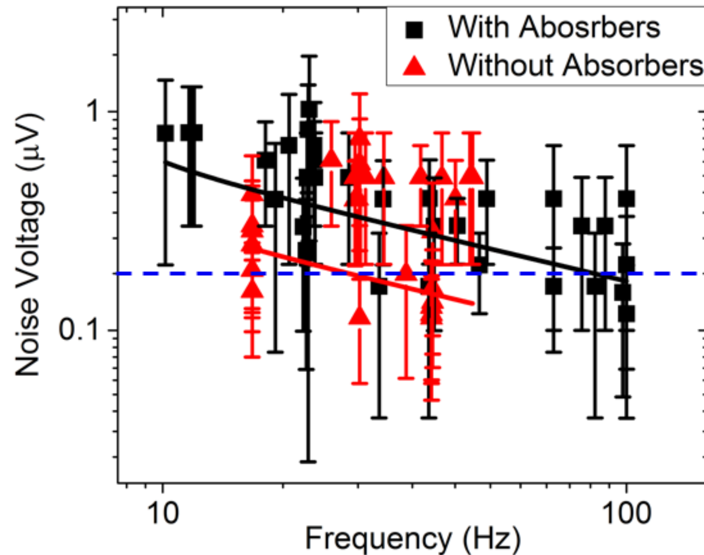

Figure 45. Noise voltages from devices with and without absorbers as a function of frequency, here plotted on a log-log scale. The Johnson noise floor is shown in blue, and the data are fitted based on Eq. 66 for 1/f noise.

Noise voltages as a function of modulation frequency are plotted in Figure 45. The Johnson noise floor at 200nV is plotted in comparison. The data suggest a strong 1/f dependence, with the 1/f knee at or before 100 Hz. The data are fitted using Eq. 66 as was done for gold black detectors in Chapter 4, from which the 1/f parameter $\kappa = \frac{\alpha_H}{nV}$ is found to be 1.3 ×

10^{-14} and 4.4×10^{-14} for detectors without and with absorbers, respectively. This gives a normalized Hooge parameter $\frac{\alpha_H}{n}$ nearly two orders of magnitude smaller than was present for the previous design. Although the fits for the data indicate less 1/f noise for detectors with absorbers, the large amount of measurement uncertainty makes this comparison inconclusive. It may be concluded, however, that 1/f noise, while still dominant at low frequencies, is reduced from the design used in Chapter 4.

The thermal time constant for detectors was determined in the same manner as for the gold black detectors discussed in Chapter 4. The signal voltage was measured as a function of chopping frequency from 10-150 Hz for both detectors with and without the absorbers. A 2V applied bias was used over the full bandwidth. Figure 46 presents a plot of responsivity as a function of chopping frequency. Responsivity values are absent near 60 Hz due to noise. The data are fit according to Eq. 67 for the parameters $\mathcal{R}_0$ and τ. The thermal time constant is found to be 4.05 ms and 4.82 ms for samples with and without the absorbers, respectively, an increase of 19%. $\mathcal{R}_0$ increases from 2.31 kV/W to 4.21 kV/W by adding the absorber, which represents an increase of 82%, slightly higher than the earlier observed increase of 71% at 35 Hz frequency. The detectors with absorbers are more sensitive to an increase in modulation frequency due to their higher time constant and thermal mass, therefore the lowest modulation frequencies will see the highest increase in responsivity.

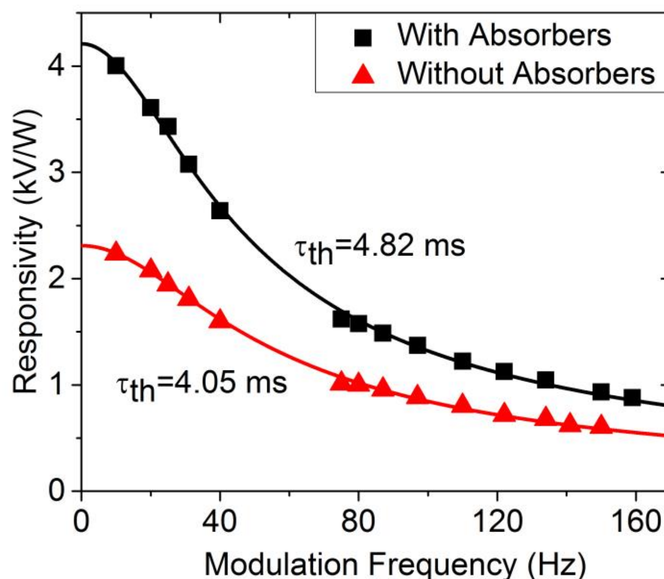

Figure 46. The voltage responsivity of devices with and without absorbers as a function of chopping frequency. This data is taken with a bias voltage of 2V. The solid lines are fits to Eq. 29.

The responsivity measurements with respect to frequency from Figure 46 give values for $\mathcal{R}_0$ and the thermal time constant. From these two values, and using assumptions for TCR and absorptance, the thermal conductance and heat capacity of devices can be calculated. Using TCR =-2.0% as was used for similar calculations in Chapter 4, and setting the absorptance to be 0.7 and 0.4 for the absorbers and non-absorbers, respectively, the thermal conductance calculates to be $G = 1.6 \times 10^{-6}\ W/K$ for detectors with absorbers and $G = 1.7 \times 10^{-6}\ W/K$ for detectors without absorbers. The heat capacity calculates to be $C = 8 \times 10^{-9}\ J/K$ and $C = 7 \times 10^{-9}\ J/K$, an increase of 14%, comparable to the increase of 19% in thermal time constant. The thermal conductance is considerably higher than

observed for gold black detectors, while the heat capacity is also larger, but by a smaller extent.

The responsivity and noise voltage are plotted as a function of applied bias voltage in Figure 47. Measurement error is shown for the noise measurements. Measurement error for responsivity measurements was less than 1%, which is not visible on the scale of this plot, so these were omitted. The responsivity peaks at an applied bias of 3V. The linear relationship predicted by Eq. 29 thus holds only up to 3 V bias. The noise increases as well but appears to flatten out around 3V. Thus, the bias that optimizes D* is 3V.

Excessive bias risks breakdown across the resistive element, resulting in a permanent short, and Joule heating raises bolometer temperature and reduces sensitivity [74]. Different designs have been introduced to compensate for such heating [75, 76]. By simply considering the bias voltage, a 1 V bias causes 5 μW heating, while 4 V increases this heating by a factor of 16 to 80 μW. However, heating also decreases the bolometer resistance, which tempers the increase in power slightly. The TCR $\alpha = \frac{1}{R}\frac{dR}{dT}$, so a lower device resistance reduces dR/dT. Joule heating also decreases the thermal conductivity, increasing the thermal time constant, which affects the frequency response.

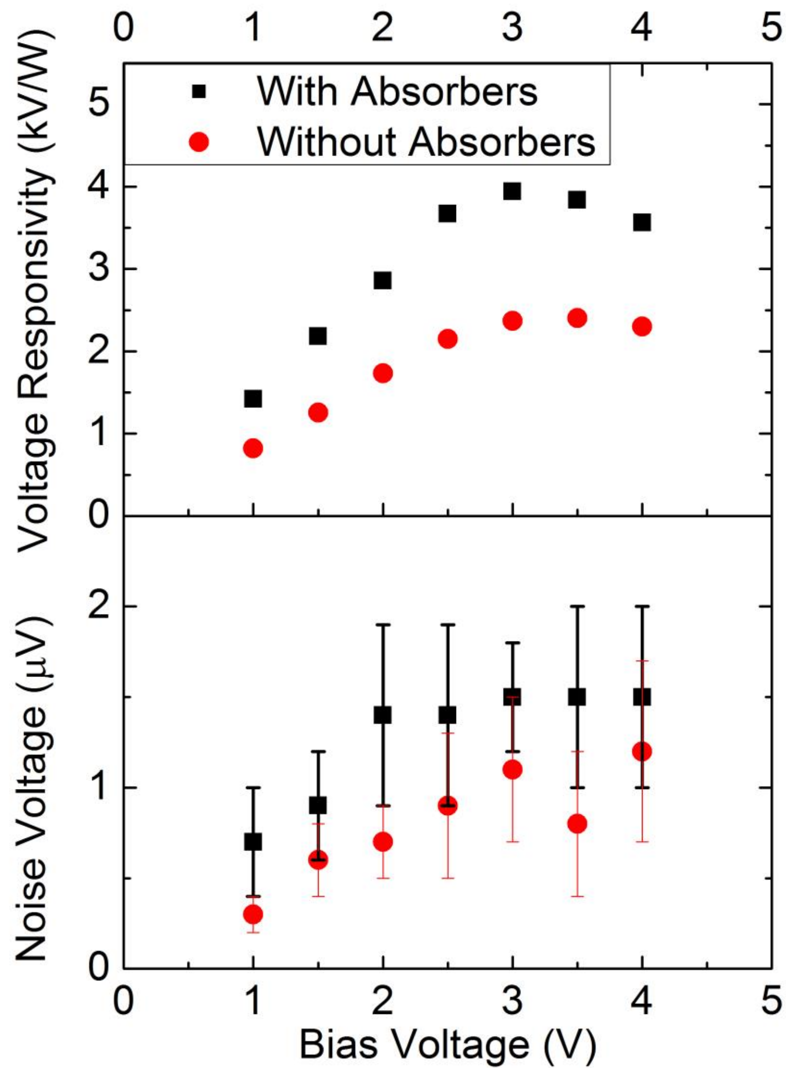

Figure 47. Responsivity and noise voltage as a function of bias voltage measured at 35 Hz.

Detectors were also measured using various optical filters to select different bandwidths. Data for responsivity as a function of detector bandwidth is reported in Figure 48. Responsivity was measured without an optical filter initially, which is indicated in the full bandwidth measurement. An increase of 71% is observed over this region. Optical filters

were used to isolate the MWIR and LWIR bandwidths. Responsivity increased higher for MWIR at 96% than in LWIR with a 49% gain. The device is designed for LWIR initially, and the absorption band for SiO_2 is also in LWIR, so a smaller increase in this bandwidth is to be expected with the additional absorber. Even with a 96% responsivity increase, the MWIR performance is still less than the LWIR performance *without* the absorber. Hence, the absorber enables dual band function for a bolometer initially designed for single bandwidth capability.

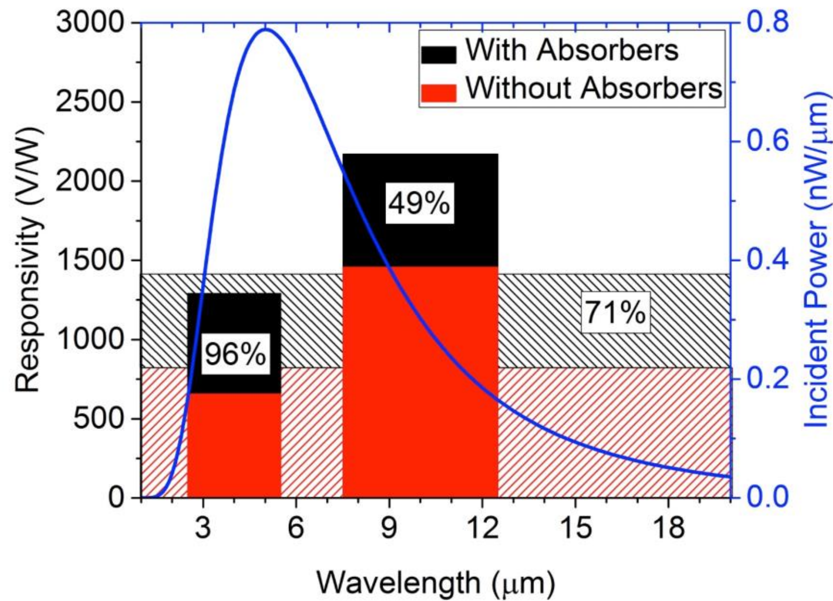

Figure 48. Voltage responsivity as a function of measurement bandwidth, plotted in comparison to the spectral incident power used in measurement for a 300°C blackbody. Data were taken using 2V applied bias at 35 Hz modulation.

5.4 D* and NETD

Performance calculations derived from measured responsivity and noise voltage of devices is presented in Table 6. While all testing conditions report an increase in D*, the greatest increases occur at lower frequencies, while only a modest improvement is seen at 100 Hz modulation. Furthermore, performance in the LWIR are smaller than the full band, as the absorbers provide the benefit of additional bandwidth for achieving high absorption. The largest improvement is observed for devices operated at a higher bias voltage. D* also increases at a higher bias voltage, bringing it closer to desired performance levels.

Table 6. Comparison of D and NETD for devices with and without the absorbers under various testing configurations.*

Testing Conditions	NEP [W]	D* [cm√Hz W^{-1}]	NETD [mK]	% Increase D*	% Decrease NETD
No Absorber, 35 Hz, 1V	6.00×10^{-10}	2.35×10^{7}	1348.51	24%	-19%
Absorber, 35 Hz, 1V	4.85×10^{-10}	2.90×10^{7}	1091.27		
No Absorber, 100 Hz, 1V	1.17×10^{-9}	1.21×10^{7}	2623.17	5%	-5%
Absorber, 100 Hz, 1V	1.11×10^{-9}	1.26×10^{7}	2502.07		
No Absorber, 35 Hz, 1V, LWIR	2.26×10^{-10}	6.21×10^{7}	509.25	17%	-15%
Absorber, 35 HZ, 1V, LWIR	1.93×10^{-10}	7.28×10^{7}	434.98		
No Absorber, 35 HZ, 3V	5.00×10^{-10}	2.81×10^{7}	1124.22	33%	-25%
Absorber, 35 HZ, 3V	3.75×10^{-10}	3.75×10^{7}	843.16		

D* is maximized by limiting the bandwidth to LWIR. In this bandwidth, D* is roughly two times less than is achieved in many commercial devices. However, these measurement values are only at 1V. Increasing the bias voltage and limiting the bandwidth may increase D* to ~10^8.

5.5 Summary

We have demonstrated the integration of a thin-film "metamaterial" absorber onto a vanadium oxide microbolometer. Strong increase in responsivity resulted due to improved absorption. The uncoated bolometer was designed for a fairly narrow LWIR band by using a Fabry-Perot resonant cavity, and the thin film absorber broadens the spectral response to include the MWIR. The device can be entirely patterned by photolithography and requires no exotic steps or materials. By operating with 3 V bias and at a modulation frequency of 30 Hz, it is possible to achieve D* of $\sim 10^8\ cm\sqrt{Hz}/W$ for both the MWIR and LWIR bands, which is a significant improvement over the original design of these detectors.

CHAPTER SIX: CONCLUSIONS

6.1 Evaluation of Methods

It is clear that changing the detector design to the flat pattern in place of the polyimide sacrificial layer improved detector performance, mechanical stability and overall yield. The possibility of generating detectors with longer arms for higher lower thermal conductance makes this new approach very attractive. The drawback of the latter design is the loss of the Fabry-Perot cavity, although this is a solvable problem a suitable metal etch stop layer, as discussed earlier.

The biggest concern from devices fabricated is the relatively low TCR of the VO_x-Au film. While -2.0% is acceptable, this value must be significantly higher to achieve D* values in the high 10^8 or even 10^9 range, in which state-of-the-art performance could be achieved.

The two absorbing structures discussed in this work both have positive effects on device performance. Comparing the results from the gold black experiments with results from the metamaterial experiments is unfortunately difficult because these absorbers were patterned on different detector designs. The metamaterial absorbers had the lowest predicted NETD of all devices for the LWIR, as well as having a higher responsivity increase for full range, LWIR and MWIR measurements. Responsivity increase, while a useful metric for evaluating the benefit of a specific type of film on a specific detector, is not transferrable to other detectors. The responsivity increase observed for the metamaterial absorbers is likely high only because the native device absorption was low from a poor cavity design.

Application of these absorbers on a detector with a high native absorption would result in a very small increase in responsivity.

To compare the gold black film and metamaterial absorber, it is more useful to look at absorptance, bandwidth and fabrication complexity and longevity of the material. The absorbed power can be determined as the product of the spectral incident power and the spectral absorption. Figure 49 compares the absorbed power of the measured Fabry-Perot cavity, as well as the measured gold black and metamaterial absorbers. These values are plotted against the spectral radiance of the 300°C blackbody used in experiment. One thing to note is that most of the blackbody incident power is in the MWIR, where the gold black and metamaterial absorber perform considerably well, especially compared with the Fabry-Perot cavity. In the LWIR, the differences are less pronounced. Additionally, the advantage of the gold black film is that absorptance is much more flat across the spectrum than the metamaterial absorber. In a practical device, there will not be much atmospheric transmission between 5-8 μm, therefore the sharp dip in this region for the metamaterial device will be negligible. By optimizing the size of the squares, the metamaterial absorber can be designed to have peaks in the MWIR and LWIR, making it a comparable absorber to gold black.

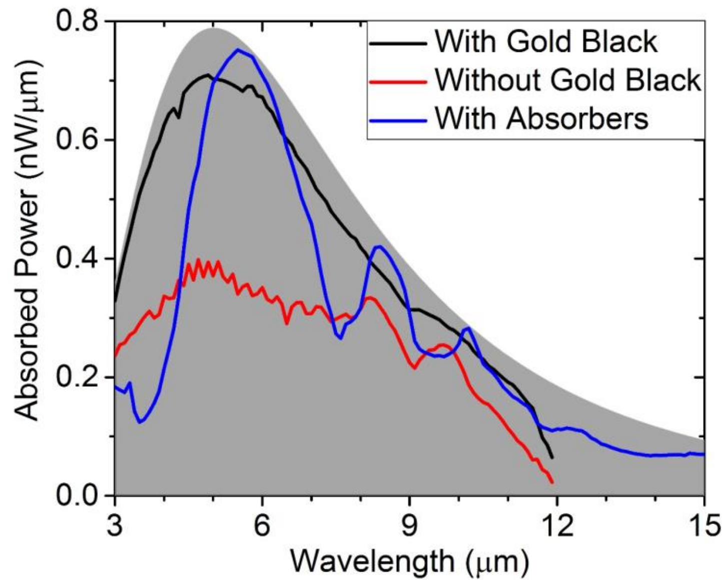

Figure 49. Comparison of absorbed power between different absorbers, plotted against the maximum absorbed power for a 300°C blackbody.

The additional benefit of the metamaterial absorber is the ease of fabrication and the longevity of the absorber. Gold black requires a somewhat more exotic method of deposition, while the metamaterial absorber is deposited using standard fabrication techniques. The drawbacks of thermal degradation of gold black is not apparent in the metamaterial film, as these structures are much more chemically and thermomechanically stable. Until low-temperature vacuum sealing can be achieved and integrated into the process of standard vacuum sealing of devices, the metamaterial absorber remains a more attractive option.

6.2 Future Experiments

Gold black is susceptible to thermal processing partially because gold is a highly mobile material [77]. It is possible that other metal blacks would withstand thermal processing if the metal was less mobile and had a higher melting point. A proposed experiment would be to measure absorption for various metal blacks after different thermal processing steps, and to correlate this absorption to structure size visible through SEM cross sections. Materials such as platinum black, tungsten black, and even chromium black would be good candidates for experimentation. Deposition of these materials by thermal evaporation methods used for gold black would require higher currents, and is beyond the capability of the deposition chamber used for gold black processing.

An alternative experiment involves further integration of the resonant absorbing structure with the VO_x-Au microbolometer. The main problem with the absorber is the added heat capacity, such that the thermal response time is increased. To reduce this effect, the absorber could be fully and intimately integrated into the microbolometer. Figure 50 presents a cross section schematic of the proposed structure. The absorber comprises an insulated metal blanket layer, a thin dielectric layer for electrical isolation, a thick semiconducting VO_x film, another dielectric layer to encapsulate and insulate the VO_x, and finally a periodic array of metal squares.

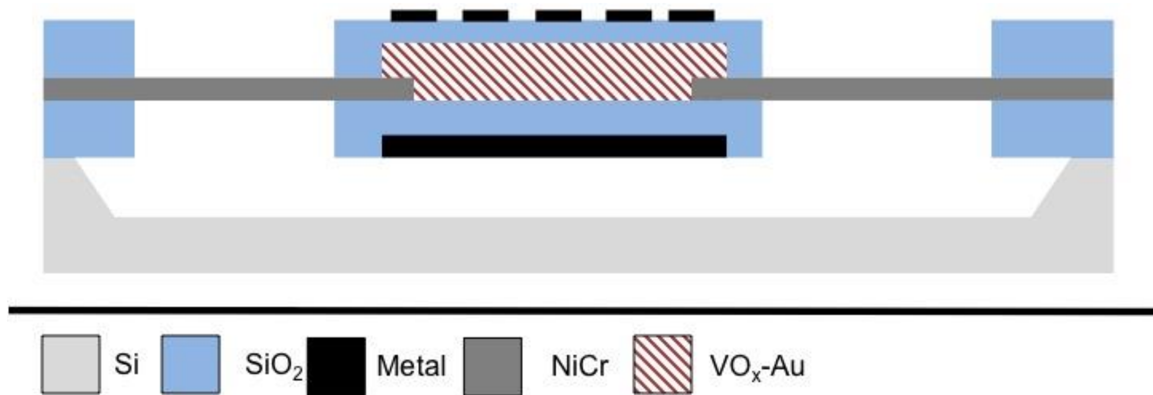

Figure 50. Schematic for a VO_x-Au microbolometer with integrated resonant absorber structure.

A secondary advantage of this approach is due to the thicker VO_x layer. This reduces device resistance given a constant film resistivity. In theory, TCR would remain unchanged as this is related to resistivity, not total resistance. The result would be a reduction in Johnson noise. Potentially, absorption could increase over a larger bandwidth due the different dispersion relations of the dielectric and the VO_x intersecting with the resonant modes of the periodic array, but these results require further study and simulation of designs.

APPENDIX A: DERIVATION OF BLACKBODY RADIANCE

Planck's Law describes the amount of energy emitted from a blackbody with respect to the body temperature and wavelength bandwidth, given in the text as Eq. 2. This derivation seeks to provide the theoretical background of this radiance term, and in the process, explain some mathematical properties of this function. This derivation follows models given in Amit [28], Dereniak [24], Landau [27], and Pathria [78]. While none of these sources specifically includes all of the following derivations, it should be stressed that this work is simply combining various derivations and explanations from the above authors, who are themselves explaining phenomena derived by Planck and others. There are many different approaches towards deriving the Planck equation, historically stemming from work by Planck, Bose and Einstein. Here, the approach looks at the distribution of harmonic oscillators under Bose-Einstein statistics, and then relates this to the specific case of photons.

The probability of an oscillator being found in the nth energy level is given by

$$P(n_1, n_2 \dots n_N) = Z^{-1} e^{\beta E(n_1, n_2, n_N)}, \tag{A1}$$

where Z is the is the partition function and can be described as $Z = z^N$, where z is the partition function of a single oscillator such that

$$z = \sum_{n=0}^{\infty} e^{\beta \hbar \omega \left(n + \frac{1}{2}\right)} . \tag{A2}$$

Eq. A2 gives the energy as of a system as

$$E = \hbar \omega \left(n + \frac{1}{2}\right) . \tag{A3}$$

Eq. A1 can be rewritten as the product of N probabilities:

$$P(n_1, n_2 \dots n_N) = P(n_1)P(n_2)\dots P(n_N)\,, \tag{A4}$$

where $P(n) = z^{-1}e^{-\beta E}$. Now the expectation value of the distribution of oscillators is

$$\langle n\rangle = z^{-1}\sum n e^{-\beta E}\,, \tag{A5}$$

where the summation is taken over infinity. This value is the mean number of oscillators in each quantum state, or the degree of excitation of the oscillators. It will also be referred to as the distribution function. Substituting from Eqs. A2 and A3 yields

$$\langle n\rangle = \frac{\sum n e^{-\beta\hbar\omega\left(n+\frac{1}{2}\right)}}{\sum e^{-\beta\hbar\omega\left(n+\frac{1}{2}\right)}} = \frac{\sum n e^{-\beta\hbar\omega n} e^{-\beta\hbar\omega\left(\frac{1}{2}\right)}}{\sum e^{-\beta\hbar\omega n} e^{-\beta\hbar\omega\left(\frac{1}{2}\right)}} = \frac{\sum n e^{-\beta\hbar\omega n}}{\sum e^{-\beta\hbar\omega n}} = \frac{\sum n e^{-xn}}{\sum e^{-xn}}\,, \tag{A6}$$

where the final step comes from substituting $x = \beta\hbar\omega$. As the numerator is the derivative of the denominator, Eq. A6 can be written as

$$\langle n\rangle = -\frac{d}{dx} ln \sum e^{-xn} = -\frac{d}{dx} ln \sum (e^{-x})^n = -\frac{d}{dx}\ln\left(\frac{1}{1-e^{-x}}\right). \tag{A7}$$

Taking the derivative in Eq. A7 and substituting the original terms, we find

$$\langle n\rangle = \frac{1}{e^{\beta\hbar\omega}-1}\,. \tag{A8}$$

Eq. A8 is the Bose-Einstein distribution (Landau calls this *Planck's distribution*) and describes the probability that an oscillator will be found in a specific state of certain energy.

The argument thus far is made for any oscillators subject to Bose-Einstein statistics (bosons). It now makes sense to switch to speaking specifically of photons, which propagate in all directions at velocity c.

The density of states is the number of quantum states of photons per wavelength (per volume). This term, multiplied by distribution of oscillators in Eq. A8 will yield the total number of oscillators per unit frequency. Consider a square box of length L, such that the volume of the box is given by $V=L^3$. The possible modes of oscillations of standing waves inside this box are, in each dimension,

$$k_x = \frac{2\pi n_x}{L}, k_y = \frac{2\pi n_y}{L}, k_z = \frac{2\pi n_z}{L}, \quad \text{(A9)}$$

where n_x, n_y and n_z are integers and k is the wave vector such that $k = \frac{\omega}{c}$. We can rewrite Eq. A9 to obtain the total number of possible modes in each dimension

$$n_x = \frac{k_x L}{2\pi}, n_y = \frac{k_y L}{2\pi}, n_z = \frac{k_z L}{2\pi}. \quad \text{(A10)}$$

The total number of possible modes in a volume dk is

$$dn_x dn_y dn_z = \frac{L^3}{(2\pi)^3} dk_x dk_y dk_z = \frac{V}{(2\pi)^3} k^2 dk d\Omega. \quad \text{(A11)}$$

Here, L^3 is the total volume, and the differential volume in Cartesian coordinates is translated into polar coordinates. The integral over the solid angle yields 4π, and the substitution of $k = \frac{\omega}{c}$ makes Eq. A11 become

$$dn = \frac{V}{(2\pi)^3}\left(\frac{\omega^2 d\omega}{c^3}\right)4\pi = \frac{V\omega^2 d\omega}{2\pi^2 c^3} \times 2 = \frac{V\omega^2 d\omega}{\pi^2 c^3}\,. \tag{A12}$$

The multiplication of two represents the two states of polarization of the photon spin, and the final term on the right is the density of states, g(ω)dω. To find the total number of photons in a frequency $d\omega$ we multiply the right side of Eq. A12 with Eq. A8 to yield

$$dN_\omega = \frac{V}{\pi^2 c^3}\frac{\omega^2 d\omega}{e^{\beta\hbar\omega}-1}\,, \tag{A13}$$

and the total energy with respect to frequency is found by multiplying Eq. A13 by the photon energy $\hbar\omega$:

$$dE_\omega = \frac{V}{\pi^2 c^3}\frac{\hbar\omega^3 d\omega}{e^{\beta\hbar\omega}-1}\,. \tag{A14}$$

This equation is *Planck's equation* in terms of frequency, and is a common form of the equation found in most statistical physics textbooks.

At this point, Planck's equation has been derived. However, for the purposes of understanding the energy distributed to a particular area; a detector for instance, this equation must be translated into power per unit source area per unit wavelength, which is the *radiance*. This can be accomplished by converting energy in terms of frequency to power in terms of frequency and then to power in terms of wavelength.

Eq. A14 can be expressed as the energy density per unit source volume per unit frequency

$$\rho(\omega) = \frac{1}{\pi^2 c^3}\frac{\hbar\omega}{e^{\beta\hbar\omega}}\,. \tag{A15}$$

Each element *dV* of the source emits radiation in all directions as $\rho(\omega)d\omega dV$, where the volume can be expressed as $dV = r^2 sin\theta dr d\theta d\phi$. The fraction of the total amount of radiation in the direction of a unit source area *dA* is given by the ratio of the projected solid angle $\frac{dAcos\theta}{r^2}$ by the total solid angle of the volume element (4π). Thus, the energy of the radiation emitted in the direction of the unit area is

$$dE = \rho(\omega)d\omega r^2 sin\theta dr d\theta d\phi \frac{dAcos\theta}{r^2} = \rho(\omega)d\omega \frac{dA}{4\pi}\, dr\, sin\theta cos\theta d\theta\, d\phi. \quad \text{(A16)}$$

The total radiation passing through this unit area is found by integrating Eq. A16 over the volume. As the radiation travels at the speed of light, the amount of radiation that will pass through the area in a time *dt* will be *cdt*. We integrate over half of the sphere surrounding the area element, such that the equation becomes

$$dE = \rho(\omega)d\omega \frac{dA}{4\pi} \int_0^{cdt} dr \int_0^{\frac{\pi}{2}} sin\theta cos\theta d\theta \int_0^{2\pi} d\phi$$

$$dE = \rho(\omega)d\omega \frac{dA}{4\pi}\, cdt \left(\frac{1}{2}\right)(2\pi)$$

$$dE = \rho(\omega)d\omega dA dt \frac{c}{4}. \quad \text{(A17)}$$

Dividing by the time and the area yields a power per unit area per unit time, which in radiation terms is the irradiance *I* or the exitance *M*, the first being radiation incident on a surface, the latter radiation leaving a surface:

$$I(\omega) = \frac{c}{4}\rho(\omega)d\omega$$

$$I(\omega) = \frac{c}{4}\frac{1}{\pi^2 c^3}\frac{\hbar\omega^3 d\omega}{e^{\beta\hbar\omega}} = \frac{1}{4\pi^2 c^2}\frac{\hbar\omega^3 d\omega}{e^{\beta\hbar\omega}} \ . \tag{A18}$$

To convert Eq. A18 to wavelength dependence, we utilize the equality $I(\omega)d\omega = I(\lambda)d\lambda$ so that $I(\lambda) = I(\omega)\left|\frac{d\omega}{d\lambda}\right|$. Substituting $= \frac{2\pi c}{\lambda}$, $\hbar = \frac{h}{2\pi}$ and $\beta = \frac{1}{kT}$ we finally have

$$I(\lambda) = \frac{1}{4\pi^2 c^2}\frac{\hbar\left(\frac{2\pi c}{\lambda}\right)^3}{e^{\beta\hbar\left(\frac{2\pi c}{\lambda}\right)}}\frac{2\pi c}{\lambda^2} = \frac{2\pi h c^2}{\lambda^5\left[e^{\frac{hc}{\lambda kT}}-1\right]}\frac{Power}{Area\ Wavelength} \ . \tag{A19}$$

All blackbody sources are *Lambertian* sources, meaning that the radiance is independent of the viewing angle. The perceived "brightness" of the source would not change as the observer moved off of the normal of the surface. In general, radiance is defined as

$$L = \frac{\partial^2\phi}{\partial A\ cos\theta\ \partial\Omega} \ , \tag{A20}$$

where ϕ is radiated power. That is, the radiance is the power emitted per unit projected area per unit solid angle. Eq. A20 can be rewritten as

$$\partial^2\phi = L\ \partial A\ cos\theta\ \partial\Omega \ . \tag{A21}$$

Radiant exitance, or irradiance is the power per unit area, which can be derived as

$$\frac{\partial\phi}{\partial A} = \int L\ cos\theta\ \partial\Omega\ = L\int_0^{\frac{\pi}{2}} cos\theta\ sin\theta\ d\theta\ \int_0^{2\pi} d\phi = \pi L \ . \tag{A22}$$

From Eq. A22, we find the radiance by dividing Eq. A20 by π, so that radiance is

$$L = \frac{2hc^2}{\lambda^5\left[e^{\frac{hc}{\lambda kT}}-1\right]}\frac{Power}{Area \cdot Wavelength \cdot Solid\ Angle}, \quad \text{(A23)}$$

which is Eq. 2 from Chapter 2.

By differentiating Eq. A23 with respect to wavelength and setting the result equal to zero, we can determine the wavelength of the maximum power intensity. This becomes

$$\frac{\partial L}{\partial \lambda} = -\frac{2hc^2\left[5\lambda^4\left[e^{\frac{hc}{\lambda kT}}-1\right]+\lambda^5\left[-e^{\frac{hc}{\lambda kT}}\frac{hc}{\lambda^2 kT}\right]\right]}{\lambda^{10}\left[e^{\frac{hc}{\lambda kT}}-1\right]^2}, \quad \text{(A24)}$$

which simplifies to

$$\frac{\partial L}{\partial \lambda} = \frac{\frac{2hc^2k^6T^6}{h^6c^6}\left(\frac{hc}{\lambda kT}\right)^6\left[-5\left[e^{\frac{hc}{\lambda kT}}-1\right]+\left[e^{\frac{hc}{\lambda kT}}\frac{hc}{\lambda kT}\right]\right]}{\left[e^{\frac{hc}{\lambda kT}}-1\right]^2}. \quad \text{(A25)}$$

Using the substitution $x = \frac{hc}{\lambda kT}$ simplifies Eq. A25 to

$$\frac{\partial L}{\partial \lambda} = \frac{\frac{2hc^2k^6T^6}{h^6c^6}x^6\left[-5[e^x-1]+[e^x x]\right]}{[e^x-1]^2}. \quad \text{(A26)}$$

Setting Eq. A26 equal to zero lets us find the maximum value of the radiance in wavelength space. It also further simplifies the equation to

$$5[e^x - 1] = xe^x, \quad \text{(A27)}$$

which has the numerical solution of approximately $x \approx 4.96511$. Plugging this value in to the substitution made earlier and solving for the wavelength yields

$$\lambda_{max} \approx \frac{2880}{T} \mu m \,, \tag{A28}$$

which is known as Wien's Displacement Law.

APPENDIX B: PUBLICATIONS

Journal Publications

1. Imen Rezadad, Javaneh Boroumand, **Evan M. Smith**, and Robert E. Peale, "Micro electro mechanical cantilever with electrostatically controlled tip contact", Appl. Phys. Lett. 105, 033514 (2014)

2. Janardan Nath, **Evan Smith**, Douglas Maukonen, and Robert E. Peale, "Optical Salisbury screen with design-tunable resonant absorption bands", J. Applied Physics 115, 193103 (2014).

3. Deep Panjwani, Mehmet Yesiltas, Janardan Nath, D. E. Maukonen, Imen Rezadad, **Evan M. Smith**, R. E. Peale, Miriam Unger, Julia Sedlemair, Ralf Wehlitz, Carol Hirschmugl, Glenn Boreman, "Patterning of oxide-hardened gold black by photolithography and metal lift-off", Infrared Physics & Technology 62, 94-99 (2014).

4. **Evan M. Smith**, Deep Panjwani, James Ginn, Andrew P. Warren, Christopher Long, Pedro Figuieredo, Christian Smith, Janardan Nath, Joshua Perlstein, Nick Walter, Carol Hirschmugl, Robert E. Peale, David Shelton, "Dual band sensitivity enhancements of VOx microbolometer array using patterned gold black absorber", Applied Optics, ***in review***

5. **Evan M. Smith**, Janardan Nath, James Ginn, Robert E Peale, David Shelton, "Sensitivity enhancements of a vanadium oxide microbolometer using sub-wavelength resonant absorbers", ***in preparation***

Conference Proceedings

1. **Evan M. Smith**, Deep Panjwani, James Ginn, Andrew Warren, Christopher Long, Pedro Figuieredo, Christian Smith, Joshua Perlstein, Nick Walter, Carol Hirschmugl, Robert E. Peale, David Shelton, "Enhanced performance of VO_x-based bolometer using patterned gold black absorber", Proc. SPIE 9451-52 (2015) [Oral Presentation]

2. **Evan M Smith**, Deep Panjwani, James Ginn, Andrew Warren, Christopher Long, R. E. Peale, David Shelton, "Patterned gold-black absorber integrated on VOx-bolometer array enhances sensitivity and noise equivalent power", FLAVS 2015 [Poster].

3. **Evan M. Smith**, James C. Ginn, Andrew P. Warren, Christopher J. Long, Deep Panjwani, Robert E. Peale, David J. Shelton, "Linear bolometer array using a high TCR VOx-Au film", Proc. SPIE 9070 - 120 (2014) [Poster].

4. Imen Rezadad, Javaneh Boroumand, **Evan M. Smith**, Ammar Alhasan, Robert E. Peale, "Vertical electrostatic force in MEMS cantilever IR sensor", Proc. SPIE 9070 - 57 (2014).

5. Javaneh Boroumand, Imen Rezadad, Ammar Alhasan, **Evan Smith**, R. E. Peale, "Thermomechancial Characterization in a Radiant Energy Imager Using Null Switching", Proc. SPIE 9070 - 125 (2014).

6. Deep Panjwani, Nima Nader-Esfahani, Doug Maukonen, Imen Rezadad, Javaneh Boroumand, **Evan Smith**, Janardan Nath, R.E. Peale, "Patterning and hardening of Gold Black infrared absorber by shadow mask deposition with Ethyl Cyanoacrylate", Proc. SPIE 8708-41 (2013).

7. **Evan Smith**, Javaneh Boroumand, Imen Rezadad, Pedro Figueiredo, Janardan Nath, Deep Panjwani, R. E. Peale, Oliver Edwards, "MEMS clocking-cantilever thermal detector," Proc. SPIE 8704 - 100 (2013) [Oral Presentation]

8. Janardan Nath, Douglas Maukonen, **Evan Smith**, Pedro Figueiredo, Guy Zummo, Deep Panjwani, Robert E. Peale, Glenn Boreman, Justin W. Cleary, Kurt Eyink, "Thin-film, wide-angle, design-tunable, selective absorber from near UV to far infrared", Proc. SPIE 8704 - 127 (2013).

9. Imen Rezadad, Javaneh Boroumand, **Evan Smith**, Pedro Figueiredo, Robert Peale, "Stress Analysis of Free-standing Silicon Oxide Films Using Optical Interference", Mater. Res. Soc. Symp. Proc. Vol. 1536 (2013).

10. **Evan Smith**, Robert Peale, Imen Rezadad, Oliver Edwards, "Performance measurement of a commerical PbSe photoconductor", Florida AVS, Orlando 2013 [Poster]

11. Javaneh Boroumand Azad, Imen Rezadad, Janardan Nath, **Evan Smith**, Robert E. Peale, "Release of MEMS devices with hard-baked polyimide sacrificial layer" Proc. SPIE 8682 - 80 (2013).

12. Janardan Nath, Casey Schwarz, **Evan Smith**, Chandana Ghosh, R. E. Peale, L. Chernyak, Walter R. Buchwald, "Cathodoluminescence of conducting gratings and implications for electron-beam investigations of nano-photonic devices", Proc. SPIE 8376 - 18 (2012).

APPENDIX C: COPYRIGHT PERMISSION LETTERS

ELSEVIER LICENSE
TERMS AND CONDITIONS

Oct 05, 2015

This is a License Agreement between Evan Smith ("You") and Elsevier ("Elsevier") provided by Copyright Clearance Center ("CCC"). The license consists of your order details, the terms and conditions provided by Elsevier, and the payment terms and conditions.

All payments must be made in full to CCC. For payment instructions, please see information listed at the bottom of this form.

Supplier	Elsevier Limited The Boulevard,Langford Lane Kidlington,Oxford,OX5 1GB,UK
Registered Company Number	1982084
Customer name	Evan Smith
Customer address	2762 Pepper Lane
	ORLANDO, FL 32812
License number	3722641138864
License date	Oct 05, 2015
Licensed content publisher	Elsevier
Licensed content publication	Elsevier Books
Licensed content title	Semiconductors and Semimetals
Licensed content author	R.A. Wood
Licensed content date	1997
Number of pages	79
Start Page	43
End Page	121d
Type of Use	reuse in a thesis/dissertation
Intended publisher of new work	other
Portion	figures/tables/illustrations
Number of figures/tables/illustrations	1
Format	both print and electronic
Are you the author of this Elsevier chapter?	No
Will you be translating?	No
Original figure numbers	Figure 6 (Chapter 3)
Title of your thesis/dissertation	Development and optimization of a vanadium oxide microbolometer using absorbing coatings and other methods
Expected completion date	Oct 2015
Estimated size (number of pages)	120
Elsevier VAT number	GB 494 6272 12
Permissions price	0.00 USD
VAT/Local Sales Tax	0.00 USD / 0.00 GBP
Total	0.00 USD

Copyright Permission Letter for the image used in Figure 6

AIP PUBLISHING LLC LICENSE
TERMS AND CONDITIONS

Oct 05, 2015

All payments must be made in full to CCC. For payment instructions, please see information listed at the bottom of this form.

License Number	3722620151447
Order Date	Oct 05, 2015
Publisher	AIP Publishing LLC
Publication	Journal of Vacuum Science & Technology A
Article Title	Potential for reactive pulsed-dc magnetron sputtering of nanocomposite VOx microbolometer thin films
Author	Yao O. Jin,Adem Ozcelik,Mark W. Horn, et al.
Online Publication Date	Aug 28, 2014
Volume number	32
Issue number	6
Type of Use	Thesis/Dissertation
Requestor type	Author (original article)
Format	Electronic
Portion	Figure/Table
Number of figures/tables	1
Title of your thesis / dissertation	Development and optimization of a vanadium oxide microbolometer using absorbing coatings and other methods
Expected completion date	Oct 2015
Estimated size (number of pages)	120
Total	0.00 USD

Copyright Permission Letter for the image used in Figure 13.

REFERENCES

1. Herschel, W., *Experiments on the Refrangibility of the Invisible Rays of the Sun. By William Herschel, LL. DFRS.* Philosophical Transactions of the Royal Society of London, 1800: p. 284-292.
2. *"Atmosfaerisk spredning". Licensed under Public Domain via Wikimedia Commons* - https://commons.wikimedia.org/wiki/File:Atmosfaerisk_spredning.png - /media/File:Atmosfaerisk_spredning.png.
3. Dunlap, R.A., *Experimental Physics-Modern Methods.* Experimental Physics-Modern Methods, by RA Dunlap, pp. 392. Foreword by RA Dunlap. Oxford University Press, Oct 1988. ISBN-10: 0195049497. ISBN-13: 9780195049497, 1988. **1**.
4. Niklaus, F., C. Vieider, and H. Jakobsen. *MEMS-based uncooled infrared bolometer arrays: a review*. in *Photonics Asia 2007*. 2007. International Society for Optics and Photonics.
5. Shie, J.-S., et al., *Characterization and modeling of metal-film microbolometer.* Microelectromechanical Systems, Journal of, 1996. **5**(4): p. 298-306.
6. Gu, X., et al., *Determination of thermal parameters of microbolometers using a single electrical measurement.* Applied Physics Letters, 1998. **72**(15): p. 3.
7. Wood, R.A. *Uncooled thermal imaging with monolithic silicon focal planes*. 1993.
8. Basantani, H.A., et al. *Vertically integrated pixel microbolometers for IR imaging using high-resistivity VOx*. in *SPIE Defense, Security, and Sensing*. 2013. International Society for Optics and Photonics.
9. Rogalski, A., *Infrared detectors for the future.* Acta Physica Polonica-Series A General Physics, 2009. **116**(3): p. 389.
10. Kruse, P.W., *Uncooled thermal imaging: arrays, systems, and applications*. Vol. 2003. 2001: SPIE press Bellingham, WA.
11. *<320 by 240 silicon microbolometer uncooled IR FPA with on chip offset correction.pdf>.*
12. Morin, F., *Oxides which show a metal-to-insulator transition at the Neel temperature.* Physical Review Letters, 1959. **3**(1): p. 34.
13. Andresen, B.F., et al., *Development and optimization of microcantilever based IR imaging arrays.* 2008. **6940**: p. 694013.
14. Liu, N., et al., *Infrared perfect absorber and its application as plasmonic sensor.* Nano Lett, 2010. **10**(7): p. 2342-8.
15. Watts, C.M., X. Liu, and W.J. Padilla, *Metamaterial electromagnetic wave absorbers.* Adv Mater, 2012. **24**(23): p. OP98-120, OP181.
16. Andresen, B.F., et al., *Wavelength selective wideband uncooled infrared sensor using a two-dimensional plasmonic absorber.* 2013. **8704**: p. 870418.

17. Smith, E.M., et al. *Enhanced performance of VOx-based bolometer using patterned gold black absorber*. 2015.
18. Wang, B., et al., *Vanadium oxide microbolometer with gold black absorbing layer.* Optical Engineering, 2012. **51**(7): p. 074003-1-074003-6.
19. Muralt, P., *Micromachined infrared detectors based on pyroelectric thin films.* Reports on Progress in Physics, 2001. **64**(10).
20. Smith, E.M., et al. *Linear bolometer array using a high TCR VOx-Au film*. in *SPIE Defense+ Security*. 2014. International Society for Optics and Photonics.
21. Becker, W., et al., *Black gold deposits as absorbers for far infrared radiation.* physica status solidi (b), 1996. **194**(1): p. 241-255.
22. Panjwani, D., et al., *Patterning of oxide-hardened gold black by photolithography and metal lift-off.* Infrared Physics & Technology, 2014. **62**: p. 94-99.
23. Nath, J., et al. *Infra-red spectral microscopy of standing-wave resonances in single metal-dielectric-metal thin-film cavity*. in *SPIE Nanoscience+ Engineering*. 2015. International Society for Optics and Photonics.
24. Dereniak, E. and G. Boreman, *Infrared Detectors andSystems*. 1996, New York: Wiley and Sons.
25. Wood, R., *Monolithic silicon microbolometer arrays.* Semiconductors and Semimetals, 1997. **47**: p. 43-121.
26. Liu, W.-T., et al., *Intrinsic Optical Properties of Vanadium Dioxide near the Insulator− Metal Transition.* Nano letters, 2010. **11**(2): p. 466-470.
27. Landau, L.D., E. Lifshitz, and L. Pitaevskii, *Statistical Physics (Course of Theoretical Physics, Volume 5).* 3rd. Edition, 1984.
28. Amit, D.J. and Y. Verbin, *Statistical physics: an introductory course*. 1999: World Scientific.
29. Basantani, H.A., et al. *Evaluation of 1/f noise in prospective IR imaging thin films*. in *SPIE Defense+ Security*. 2014. International Society for Optics and Photonics.
30. Paradis, S., et al. *Vanadium oxide films for optical modulation applications*. in *Photonics North 2006*. 2006. International Society for Optics and Photonics.
31. Chen, C., et al., *Characterizations of VO 2-based uncooled microbolometer linear array.* Sensors and Actuators A: Physical, 2001. **90**(3): p. 212-214.
32. Ramanathan, S., *Thin film metal-oxides.* Harvard University: Springer New York Dordrecht Heidelberg London, 2010.
33. Wang, Y., et al., *Phase composition and valence of pulsed laser deposited vanadium oxide thin films at different oxygen pressures.* Surface and Coatings Technology, 2007. **201**(9): p. 5344-5347.
34. Berghmans, F., et al., *Low-cost uncooled microbolometers for thermal imaging.* 2010. **7726**: p. 772611.
35. Jin, Y.O., et al., *Potential for reactive pulsed-dc magnetron sputtering of nanocomposite VOx microbolometer thin films.* Journal of Vacuum Science & Technology A, 2014. **32**(6): p. 061501.

36. Muralt, P., *Micromachined infrared detectors based on pyroelectric thin films.* Reports on Progress in Physics, 2001. **64**(10): p. 1339.
37. Datskos, P.G., N.V. Lavrik, and S. Rajic, *Performance of uncooled microcantilever thermal detectors.* Review of Scientific Instruments, 2004. **75**(4): p. 1134.
38. Corbeil, J.L., et al., *"Self-leveling" uncooled microcantilever thermal detector.* Applied Physics Letters, 2002. **81**(7): p. 1306.
39. Niklaus, F., et al., *Performance model for uncooled infrared bolometer arrays and performance predictions of bolometers operating at atmospheric pressure.* Infrared Physics & Technology, 2008. **51**(3): p. 168-177.
40. He, X., et al., *Performance of microbolometer focal plane arrays under varying pressure.* Electron Device Letters, IEEE, 2000. **21**(5): p. 233-235.
41. Endo, R., M. Shima, and M. Susa, *Thermal-conductivity measurements and predictions for Ni–Cr solid solution alloys.* International Journal of Thermophysics, 2010. **31**(10): p. 1991-2003.
42. Syllaios, A., et al. *Amorphous silicon microbolometer technology*. in *MRS Proceedings*. 2000. Cambridge Univ Press.
43. Cole, B.E., B.S. Fritz, and R.D. Horning, *Fabry-Perot micro filter-detector*. 1996, Google Patents.
44. Spears, D.L., *Infrared detector using a resonant optical cavity for enhanced absorption*. 1995, Google Patents.
45. http://software.kjinnovation.com/GD-Calc.html.
46. Olsen, J. and F. Shimura, *Infrared reflection spectroscopy of the SiO2 ‐ silicon interface.* Journal of applied physics, 1989. **66**(3): p. 1353-1358.
47. Knolle, W. and J. Osenbach, *The structure of plasma ‐ deposited silicon nitride films determined by infrared spectroscopy.* Journal of applied physics, 1985. **58**(3): p. 1248-1254.
48. Panjwani, D., et al. *Metal-black scattering centers to enhance light harvesting by thin-film solar cells*. in *SPIE Defense, Security, and Sensing*. 2011. International Society for Optics and Photonics.
49. PANJWANI, D.R., *CHARACTERIZATION OF GOLD BLACK AND ITS APPLICATION IN UN-COOLED INFRARED DETECTORS*. 2015, University of Central Florida Orlando, Florida.
50. Pfund, A., *The optical properties of metallic and crystalline powders.* JOSA, 1933. **23**(10): p. 375-377.
51. Marshall, D., et al., *Improved detectivity of pyroelectric detectors.* Final Report Honeywell Electro-Optics Center, Lexington, MA., 1978. **1**.
52. Maier, S.A., *Plasmonics: fundamentals and applications*. 2007: Springer Science & Business Media.
53. Erturk, O., et al. *A plasmonically enhanced pixel structure for uncooled microbolometer detectors*. in *SPIE Defense, Security, and Sensing*. 2013. International Society for Optics and Photonics.
54. Ogawa, S., et al., *Wavelength selective uncooled infrared sensor by plasmonics.* Applied Physics Letters, 2012. **100**(2): p. 021111.

55. Zhu, H., F. Yi, and E. Cubukcu, *Nanoantenna absorbers for thermal detectors.* Photonics Technology Letters, IEEE, 2012. **24**(14): p. 1194-1196.
56. Standard, A., *E1543.* Standard test method for noise equivalent temperature difference of thermal imaging systems. West Conshohocken (PA): ASTM International, 2011.
57. Shackelford, J.F. and W. Alexander, *CRC materials science and engineering handbook*. 2000: CRC press.
58. *Reade Advanced Materials* http://www.reade.com/component/content/article/619-nicr-nichrome-nickel-chrome-nickel-chromium-alloy-chromium-nickel-alloy-nickel-chromium-lump-nickel-chromium-powder-nickel-chromium-wire-nickel-chromium-sputtering-target-nickel-chromium-slug-nickel-chromiu?q=nicr.
59. Cho, C.-R., et al., *Current-induced metal–insulator transition in VO x thin film prepared by rapid-thermal-annealing.* Thin Solid Films, 2006. **495**(1): p. 375-379.
60. Chen, T., et al. *Study on the preparation of vanadium oxide thin films by the metal-oxygenation method*. in *International Symposium on Photoelectronic Detection and Imaging 2009*. 2009. International Society for Optics and Photonics.
61. Dem'yanenko, M.A., et al. *Uncooled 160× 120 microbolometer IR FPA based on sol-gel VOx*. in *Congress on Optics and Optoelectronics*. 2005. International Society for Optics and Photonics.
62. Lam, V.H., *Electrical Properties of Reactive Magnetron Sputtered Vanadium Oxide Thin Films*. 2005, Masters Thesis, UCF, Orlando.
63. Coffey, K.R., et al., *Nanocomposite semiconducting material with reduced resistivity*. 2012, Google Patents.
64. Panjwani, D.R., *Metal Blacks as Scattering Centers to Increase the Efficiency of Thin Film Solar Cells*. 2011, University of Central Florida Orlando, Florida.
65. Nasse, M.J., et al., *High-resolution Fourier-transform infrared chemical imaging with multiple synchrotron beams.* Nature methods, 2011. **8**(5): p. 413-416.
66. Forsberg, F., et al., *Very large scale heterogeneous integration (VLSHI) and wafer-level vacuum packaging for infrared bolometer focal plane arrays.* Infrared Physics & Technology, 2013. **60**: p. 251-259.
67. Higashi, R.E., et al., *Integrated silicon vacuum micropackage for infrared devices*. 1999, Google Patents.
68. Garcia-Blanco, S., et al. *Low-temperature vacuum hermetic wafer-level package for uncooled microbolometer FPAs*. in *MOEMS-MEMS 2008 Micro and Nanofabrication*. 2008. International Society for Optics and Photonics.
69. Stagon, S.P. and H. Huang, *Airtight metallic sealing at room temperature under small mechanical pressure.* Scientific reports, 2013. **3**.
70. Chen, H.-T., *Interference theory of metamaterial perfect absorbers.* Optics express, 2012. **20**(7): p. 7165-7172.

71. Nath, J., et al., *Far-infrared absorber based on standing-wave resonances in metal-dielectric-metal cavity.* Optics express, 2015. **23**(16): p. 20366-20380.
72. Nath, J., et al. *Thin-film, wide-angle, design-tunable, selective absorber from near UV to far infrared*. in *SPIE Defense, Security, and Sensing*. 2013. International Society for Optics and Photonics.
73. Lee, C., et al., *A novel silicon nanotips antireflection surface for the micro sun sensor.* Nano letters, 2005. **5**(12): p. 2438-2442.
74. Saxena, R.S., et al., *Effect of Excessive Bias Heating on a Titanium Microbolometer Infrared Detector.* IEEE Sensors Journal, 2008. **8**(11): p. 1801-1804.
75. Ramakrishna, M., et al., *Highly sensitive infrared temperature sensor using self-heating compensated microbolometers.* Sensors and Actuators A: Physical, 2000. **79**(2): p. 122-127.
76. Parrish, W.J. and J.T. Woolaway II. *Improvements in uncooled systems using bias equalization*. in *AeroSense'99*. 1999. International Society for Optics and Photonics.
77. Love, J.C., et al., *Fabrication and wetting properties of metallic half-shells with submicron diameters.* Nano Letters, 2002. **2**(8): p. 891-894.
78. Beale, R.K. and P.D. Pathria, *Statistical Mechanics: Third Edition*. 2011, Boston: Academic Press.